TEST OF POLE EXTRAPOLATION
PROCEDURES IN
pp -- A ---- N AT 6 GeV/c

Dissertation for the Degree of Ph. D. MICHIGAN STATE UNIVERSITY JOHN DOUGLAS MOUNTZ 1974

LIBRARY
Michigan State
University

This is to certify that the

thesis entitled

Test of Pole Extrapolation Procedures in pp \rightarrow $\Delta^{++}N$ At 6 GeV/c

presented by

John Douglas Mountz

has been accepted towards fulfillment of the requirements for

Ph.D. degree in Physics

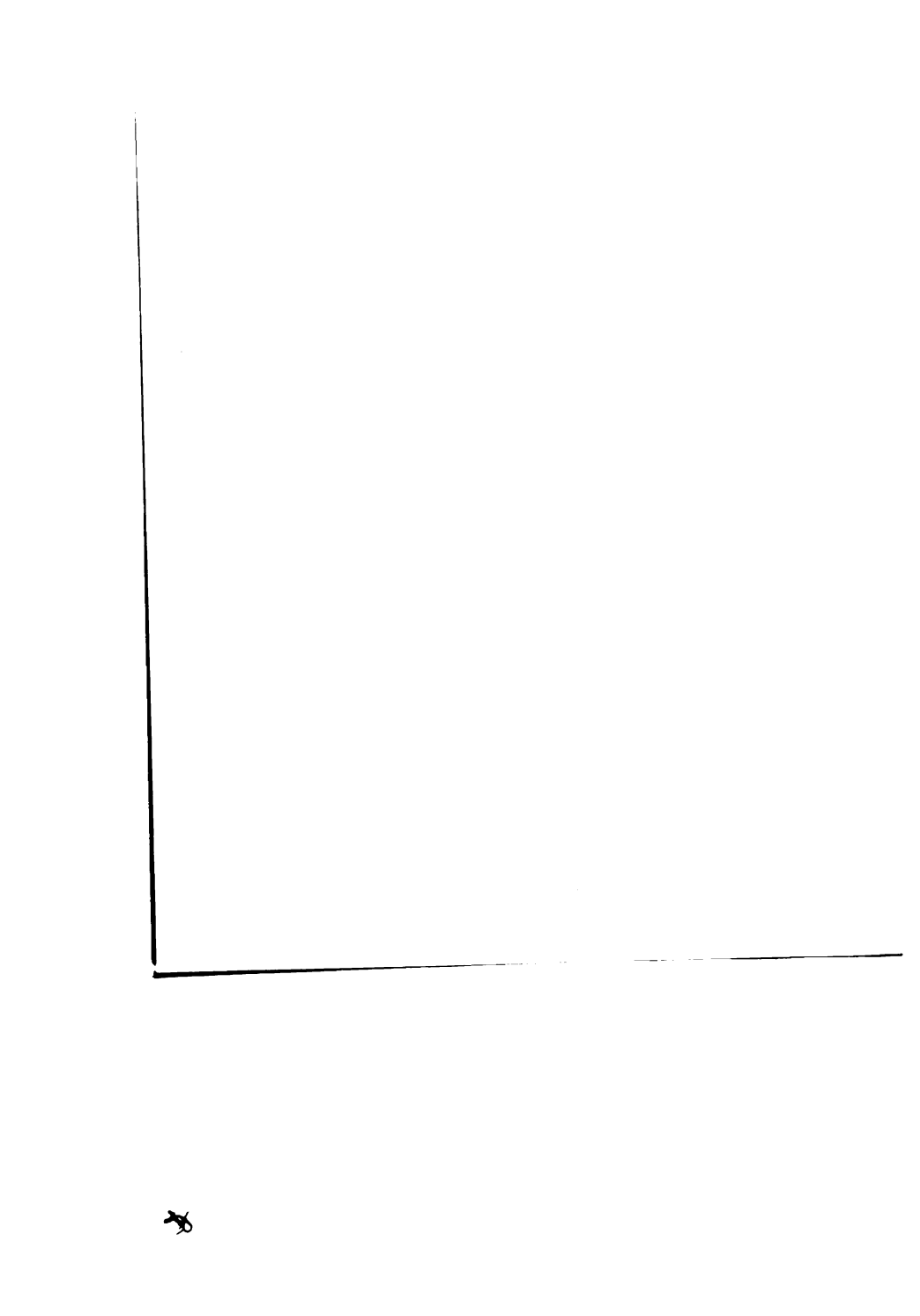
Major professor

Date May 14, 1974

0-7639

· E = 0





INO INC.

pion exchange no

reaction with a

shell pion in the

in the elastic s

shell before and

this experiment

and extrapolation

the on-shell cros

data. It is suff Wishes to extrap

ABSTRACT

TEST OF POLE EXTRAPOLATION PROCEDURES IN PP \rightarrow $\Delta++$ AT 6 GeV/c

Ву

John Douglas Mountz

The experimental apparatus in this thesis is designed to detect one pion production at a beam momentum of 6 GeV/c resulting from proton-proton collisions. Eighty percent of the events have the $PN\pi$ + final state. Thirty percent of the events have the well known $\Delta + +_{1236}(3,3)$ resonance-neutron final state. This resonance occurs at a low $M(P\pi+)$ and momentum transfer square. Assuming a onepion exchange model, this resonance is produced in this reaction with a virtual pion in the initial state and a onshell pion in the final state. The same resonance occurs in $\pi+P$ elastic scattering where the pion is on its mass shell before and after the resonance is found. The goal of this experiment is to test the accuracy of different models and extrapolation polynomials which can be used to obtain the on-shell cross section from the off-shell scattering data. It is sufficient to use form factor models if one wishes to extrapolate the total cross section. The models

considered here model, and the

It is t

known to high a here, it will a extrapolating i

on-shell value such as $\pi-\pi$ and

This extheir raw form. to obtain an until the extrapolation of the large corrections, the to date of the section.

The restand the Dürr Pinass and tranger that an At + Bt culated using enterproduce the conto the pole. The same fit terms

to pass through

at t=0 is consis

considered here are the Chew-Low model, the Dürr Pilkuhn model, and the Benecke Dürr model.

It is useful to test the validity of the extrapolation process in this case because the on-shell data is known to high accuracy. If the method proves successful here, it will add credibility to cross sections obtained by extrapolating initial virtual states to the unphysical on-shell value where the on-shell data is not available, such as $\pi-\pi$ and $\pi-K$ scattering.

This experiment provides 14 thousand $\Delta + +$ events in their raw form. The processing and corrections necessary to obtain an unbiased high quality $\Delta + +$ sample necessary for the extrapolation is the subject of much of this thesis. Due to the large number of events and the good quality of corrections, this thesis represents the most exacting test to date of the extrapolation technique for the cross section.

The results indicate that the Benecke Dürr model and the Dürr Pilkuhn model are indistinguishable for the mass and t range considered here. The results also show that an At + Bt² polynomial fit to the "to" values calculated using either of the above mentioned models will reproduce the on-shell value if the curve is extrapolated to the pole. The good fit requires no scale factors. If the same fit technique is done without requiring the curve to pass through the origin, the extrapolated cross section at t=0 is consistent with zero within the limits of the error.

in parti

TEST OF POLE EXTRAPOLATION PROCEDURES

IN pp $\rightarrow \Delta^{++}$ N AT 6 GeV/c

Ву

John Douglas Mountz

A DISSERTATION

Submitted to
Michigan State University
in partial fulfillment of the requirements
for the degree of

DOCTOR OF PHILOSOPHY

Department of Physics

I wish Gerald A. Smith

throughout the are due also t

sable assistan

analysis, and

suggestions as

data.

I am Dame for pro:

to the many F

assistance di

Sandy Schauwe

this thesis.

ACKNOWLEDGMENTS

I wish to express my appreciation to Professor

Gerald A. Smith for his patience, guidance, and motivation
throughout the analysis of this experiment. Many thanks
are due also to Professor R. J. Sprafka for his indispensable assistance during the initial stages of the data
analysis, and Professor Z. Ming Ma for his many helpful
suggestions and comments during the physics analysis of the
data.

I am deeply indebted to the University of Notre

Dame for providing the apparatus for this experiment, and
to the many people at Argonne National Laboratory for their
assistance during the data acquisition. I wish to thank
Sandy Schauweker for cheerfully typing the rough draft of
this thesis.

LIST OF TABLES

LIST OF FIGURES.

Chapter

I. INTRODUCT

II. HARDWARE.

III. EVENT PRO

IV. ZERO VALU

4.1 Zer 4.2 Bea

V. ACCEPTALIC

5.1 Gec 5.2 Zer

T. PION DECA

6.1 Pic 6.2 Ele 6.3 Str

MI. SPARK CHA

7.1 Spa 7.2 DE/

TII. RESOLUTIO

8.1 Mis 8.2 Inv

TABLE OF CONTENTS

															Page
LIST OF	TABLI	ES .	•	•	•	•	•	•	•	•	•	•	•	•	
LIST OF	F FIGUI	RES.	•	•	•	•	•	•	•	•	•	•	•	•	
Chapter	:														
I.	INTRO	DUCTIO	N	•	•	•	•	•	•	•	•	•	•	•	1
II.	HARDWA	ARE.	•		•	•	•	•	•	•	•	•	•	•	5
III.	EVENT	PROCE	ESSI	NG	ANI	SI	ELE	CTIC	ON	•	•	•	•	•	13
IV.	ZERO V	VALUE	AND	BE	EAM	MON	1EN	TUM	•	•	•	•	•	•	20
		Zero Beam				•	•	•	•	•	•	•	•	•	20 25
v.	ACCEPT	TANCE		•		•	•	•	•	•	•	•	•	•	29
		Geome Zero					ta:	nce •	•		•	•	•	•	29 33
VI.	PION I	DECAY	AND	SE	CON	DAF	RY :	SCAI	TER	RING	;.	•	•	•	44
	6.2	Pion Elect Stron	rom	agn	eti						•	•	•	•	44 46 50
VII.	SPARK	СНАМЕ	ER	EFF	CI	ENC	Y Z	AND	DE/	'DX	LO	SSE	s.	•	54
		Spark DE/DX							• •	•	•	•	•	•	54 55
VIII.	RESOLU	UTION	AND	AM	BIG	UI	CIE	s.	•	•	•	•	•	•	63
		Miss Invar			lass	•		•				•	•	•	6 <i>4</i>

IX. CROSS SEC

X. ONE PION

10.1 Kir. 10.2 Ver

F 10.3 Dür 10.4 Ben 10.5 Cor

XI. SUMMARY A:

PETERENCES . . PREMOTOES

Appendix

A. Event Prod

B. Beam Mome:

C. Transforma

D. Glac and

E. Monte Carl

P. Resonance Experime

G. Spark Cham

H. Error Calc

Chapte	•			Page
	8.3 Momentum Transfer Squared Resolution 8.4 Ambiguities	•	•	83 83
IX.	CROSS SECTION AND NORMALIZATION	•	•	98
х.	ONE PION EXCHANGE	•	•	107
	10.1 Kinematics	•	•	107
	Factors	•	•	111
	10.3 Dürr Pilkuhn Corrections	•	•	115
	10.4 Benecke Dürr Corrections	•	•	117
	10.5 Corrected Cross Section and Pole			
	Extrapolation	•	•	119
XI.	SUMMARY AND CONCLUSIONS	•	•	160
REFERE	NCES	•	•	165
APPEND	ICES			
Append	ix			
A.	Event Processing Failures	•	•	168
В.	Beam Momentum Fitting Program	•	•	175
C.	Transformation From M, t, θ_{Jac} , ϕ_{TY} to \vec{P} as	nd	 π.	178
D.	$\theta_{ extsf{Jac}}$ and $\phi_{ extsf{TY}}$ Biases	•	•	186
E.	Monte Carlo Event Generation	•	•	189
F.	Resonance Mass and Width Corrections Due to Experimental Errors	•	•	194
G.	Spark Chamber Efficiency	•	•	199
н.	Error Calculation			206

3.3. Events

3.4. Circe (

3.5. Teuta J

3.6. Teuta

3.7. Good T

3.8. Final

4.1. Initia

4.2. Beam F

5.1. Typica

6.1. Pion D

6.2. Pion D

6.3. Break-

6.4. Chemic

6.5. Coulom

6.6. Strong

LIST OF TABLES

Table							Page
3.1.	Trigger Breakdown	•	•	•	•	•	14
3.2.	BAG and ub/event	•	•	•	•	•	14
3.3.	Events Out of Crunch	•	•	•	•	•	15
3.4.	Circe Output Events	•	•	•	•	•	16
3.5.	Teuta Fit Reactions	•	•	•	•	•	16
3.6.	Teuta Fits C _T >3%	•	•	•	•	•	18
3.7.	Good Teuta Events After Cuts .	•	•	•	•	•	18
3.8.	Final Events	•	•	•	•	•	19
4.1.	Initial and Final Zero Values .	•	•	•	•	•	24
4.2.	Beam Fitting Program Test	•	•	•	•	•	25
5.1.	Typical Event Weighting Process	•	•	•	•	•	30
6.1.	Pion Decay Events	•	•	•	•	•	46
6.2.	Pion Decay Track and Fit Results	s.	•	•	•	•	46
6.3.	Break-down of Secondary Matter.	•	•	•	•	•	48
6.4.	Chemical Break-down of Material	•	•	•	•	•	49
6.5.	Coulomb Scattering Event Analys:	is.	•	•	•	•	49
6.6.	Strong Elastic Scattering	•	•	•	•	•	51

- 6.8. Strong
- 7.1. Spark C
- 7.2. DE/DX d Proto
- 7.3. Experim
- 7.4. DE/DX O Event
- 8.1. Results Plots
- 8.2. Bubble Paran
- 8.3. Mass Pa
- 8.4. 4296 Ma
- 9.1. 1++ Crc
- 9.2. Accepta
- 9.3. PN-+ C1
- 10.1. Chi-sq: at +
- 10.2. Chi-sq bt +
- A.1. Crunch
- A.2. Circe
- A.3. Reacti
- A.4. Teuta
- P.1. Peak a E^{LC}

Table		Page
6.7.	Elastic and Total Cross Sections for Protons and Pions on Carbon and Aluminum	53
6.8.	Strong Interaction Correction Factors	53
7.1.	Spark Chamber Efficiency	55
7.2.	DE/DX Counter Characteristics for 6 Gev/c Proton	57
7.3.	Experimental Discriminator Curve	60
7.4.	DE/DX Counter Characteristics for Real Event Triggers	61
8.1.	Results of Gaussian Fit to Missing Mass Plots	75
8.2.	Bubble Chamber Background Estimates Fit Parameters	76
8.3.	Mass Parameters for $\Delta++$ (1236) Resonance	82
8.4.	4296 Mark 4-Teuta Fit Breakdown	87
9.1.	Δ ++ Cross Section Factors	99
9.2.	Acceptance for PN π + and PP π °	101
9.3.	$PN\pi+$ Cross Section Factors	104
10.1.	Chi-Square and Multiplier for at, at + bt ² and at + bt ² + cT ³ fits	129
10.2.	Chi-Square and Multiplier for a + bt and a + bt + ct ² Fits	150
A.1.	Crunch Losses	168
A.2.	Circe Failures	170
A.3.	Reactions Leading to 90% of Circe Failures .	171
A.4.	Teuta Events Confidence Level <.03	171
F.1.	Peak and Width of $M(P,\pi+)$ With Resolution	197

P.3. Paramet Exper

G.1. Beam C:

G.2. Hodosco

G.3. Probab:

G.4. a. Bea

b. Mag

c. Hoo

Table		Page
F.2.	Breit-Wigner Fits to Unsmeared and Smeared Data	198
F.3.	Parameter for Predicted Fitted and Experimental Mass and Distribution	198
G.1.	Beam Chambers	201
G.2.	Hodoscope Chambers	202
G.3.	Probability for $i\frac{th}{}$ Magnet Chamber to Miss Two Tracks of a Missing Event	203
G.4.	a. Beam Chambers	
	b. Magnet Chambers	
	c. Hodoscope Chambers	205

2.1. This dexpe

2.2. The Ho fron

2.3. a. Dia alt and rur

b. Dia and cha

3.1. Coordin

4.1. The two figu: trac plan

4.2. Fitted runs

5.1. Typica

5.2. a-d sh the Jack dist

5.3. a-b Th

LIST OF FIGURES

Figure		Page
1.1.	One pion exchange diagram	2
2.1.	This diagram is an overall plan view of the experiment hardware	7
2.2.	The Hodoscope counter array is shown in a front view with lightpipes indicated	9
2.3.	a. Diagram showing how the four layers of aluminum wires are applied to a chamber and where the magnetostrictive ribbons run	12
	b. Diagram showing details of the mechanical and electrical construction of the chambers	12
3.1.	Coordinate system used in Circe	16
4.1.	The twenty distributions shown in this figure are the fitted minus measured beam track positions for the 20 spark chamber planes used in this experiment	22
4.2.	Fitted beam momentum and angles using data runs triggered on single beam tracks	27
5.1.	Typical event weighting process	32
5.2.	a-d show the mass squared of the $p\pi+$ system, the momentum transfer squared, the Jackson angle and the Treiman-Yang angle distributions respectively	3 5
5.3.	a-b Three dimensional plot of the zero acceptance region	39

- 5.4. a-d Fin (shad accep
- 7.1. Spark c
- 7.2. The tri nator
- 7.3. Single perce nator
- 8.1. Confider is my
- 8.2. Missing even
- 8.3. a. Ne:
 - b. Ga
- 8.4. a. Pi fi
 - b. Ne Ga
- 8.5. Breitbubb
- 8.6. Breitdist
- 8.7. a. Pr mc
 - b. pr
- 8.8. Spark Carl

Figure		Page
5.4.	<pre>a-d Final experimental data shown before (shaded) and after (unshaded) zero acceptance correction</pre>	42
7.1.	Spark chamber classification	54
7.2.	The triangles mark differential discriminator curve points	59
7.3.	Single and double energy loss curves and percent trigger loss due to discriminator setting	63
8.1.	Confidence level distribution after the χ^2 is multiplied by 7.2	66
8.2.	Missing mass squared distributions after event reconstruction	69
8.3.	 Neutron error distribution consistant with flat confidence level. 	
	b. Gaussian ideogram around $M_N^2 = 0.88 \text{ Gev}^2$ using errors	72
8.4.	a. Pion missing mass data and Gaussian fit for $M^2\pi$ and $\Gamma\pi$.	
	b. Neutron missing mass data and Gaussian fit for Γ_N with $M_N^2 = 0.88$.	74
8.5.	Breit-Wigner plus phase space fit to bubble chamber data	79
8.6.	Breit-Wigner fit to experimental mass distributions	81
8.7.	a. Probability of finding an error E at momentum transfer squared t.	
	b. Probability of finding an error E at momentum transfer squared t normalized so that \(\int W(t,E) \) dE = CONSTANT	85
8.8.	Spark chamber data (unshaded) and Monte Carlo events with induced errors selected by best confidence level (shaded)	89

9.1. 4++ cro

9.2. PNn+ c

10.1. One pi PP+P

10.2. Exchar

10.3. a-b.

c-d.

e-f.

10.4. a-b.

c-d.

e-f.

¹⁰.5. a.

b.

c.

е,

10.6. Dow

Figure		Page
8.9.	Distributions are plotted without ambiguity correct efficiency (unshaded) and after (shaded) the normalized correction is applied	95
		, ,
9.1.	Δ++ cross section at 6 Gev/c plotted with near by values	103
9.2.	PN π + cross section	106
10.1.	One pion exchange (OPE) diagram for PP+Pπ+N	107
10.2.	Exchange graph of scalar particle with mass X	118
10.3.	a-b. Chew-Low extrapolation curves	
	c-d. Dürr Pilkuhn extrapolation curves	
	e-f. Benecke Dürr extrapolation curves	123
10.4.	a-b. Chew Low extrapolated on-shell mass cross section and on-shell data	
	c-d. Dürr Pilkuhn extrapolated and on- shell mass data	
	e-f. Benecke Dürr extrapolated and on- shell mass data	133
10.5.	a. dg/dM experiment and Dürr Pilkuhn prediction	
	b. do/dt experiment and Dürr Pilkuhn prediction	
	c. $d\sigma/d\cos\theta_{\mbox{\scriptsize Jac}}$ experiment and Dürr Pilkuhn prediction	
	e. dσ/dφ _{TY} experiment and Dürr Pilkuhn prediction	140
10.6.	Double-Regge-Pole Model	144

Pigure

10.7. a. C

b. D.

с. в е

^{10.8}. a. C

b. D

c. I

10.9. a.

p.

c.

11.1. One

A.1. a-b.

B.1. Expe

C.1. The

c.z. _θJac

C.3. Bear ma

Figure		Page
10.7.	a. C.L. model with a + bt + ct ² extrapolation polynomials	
	b. D.P. model with a + bt + ct ² extrapolation polynomials	
	c. B.D. model with a + bt + ct ² extrapolation polynomials	147
10.8.	a. C.L. extrapolated cross section at $t = M\pi^2$ and on-shell curve for a + bt + ct^2 extrapolation curve	
	b. D.P. extrapolated cross section using same criteria as above	
	c. B.D. extrapolated cross section using same criteria as above	152
10.9.	 a. C.L. extrapolated cross section at t = 0 for a + bt + ct² extrapolation curve 	
	<pre>b. D.P. extrapolated cross section at t = 0 using same criteria as above</pre>	
	<pre>c. B.D. extrapolated cross section at t = 0 using same criteria as above</pre>	157
11.1.	One pion exchange diagram for PP+ Δ ++N	161
A.1.	a-b. Vertex distributions for events lost in the target cut plotted along the beam direction x, where x = 0 is the target center, and R	174
B.1.	Experimental apparatus after target (a) and coordinate system (b)	175
c.1.	The reaction PP→Δ++N in over-all center of mass	178
C.2.	$\theta_{ extsf{Jac}}$ and $\phi_{ extsf{TY}}$ defined in $\Delta++$ center of mass.	181
C.3.	Beam and decay proton in $\Delta++$ center of	102

- C.4. Project Figu:
- C.5. Moment: to be
- 0.1. PP+PN+
- E.1. a-d. (
- F.1. Three vers
- H.1. Notat
- H.2. Notat
- H.3. Nota

Figure		Page
C.4.	Projected view of planes described in Figure C.2	183
C.5.	Momentum of $\Delta++$ decay products perpendicular to beam proton in $\Delta++$ center of mass	184
D.1.	$PP \rightarrow PN\pi +$ event in $P-\pi +$ center of mass	186
E.1.	<pre>a-d. Original bubble chamber events (shaded) and Monte Carlo distributions which are the result of generation program (unshaded)</pre>	192
F.1.	Three dimensional plot of error in mass versus mass	196
н.1.	Notation and coordinate system used in this appendix	206
н.2.	Notation used in calculating invariant mass error	208
н.3.	Notation used in calculating momentum	209

Virtual state Their paper

Physical ta

physical vi

lab are sa

to their .

is a char

בהסעשה .

rajecto

the sca

also th

the re:

Dentio

sectio

reaio.

Polat is 亡

sye]

CHAPTER I

INTRODUCTION

In 1959, G. F. Chew and F. E. Low presented a scheme for extrapolating physical cross sections using the virtual states existing in hadronic matter as targets. Their paper draws a connection between scattering data off physical targets, which are on the mass shell, and unphysical virtual targets. Physical targets existing in the lab are said to be on-shell because their mass is related to their energy and momentum by $M^2 = E^2 - P^2$ and this mass is a characteristic of the target. Virtual targets are thought to be associated with real particles or Regge Trajectories and have a negative M² as defined above. the scattering region, the mass of the exchange particle is also the momentum transfer squared from the target proton to the neutron, denoted by t. 2 The extrapolation scheme mentioned above proposes to extend the scattering cross section, measured as a function of t in the physical region, into the unphysical positive t region. This extrapolated cross section can be evaluated at $t = M^2$, where M is the mass of the exchange particle, to obtain the onshell cross section. 3, 4

The rea

Beam

Target

Figure 1.1. On

The one pion ex

Figure 1.1. The target is an of:

the target prote

virtual pion an

Place the virtu

shell proton an

process has a h

ine to the pres

The pol

to obtain cross

thove. Experi

have been done

scattering whe

after the reso

las been measu

‰'e extrapola iata in order

The reaction considered in this thesis is $PP+\Delta++N$.

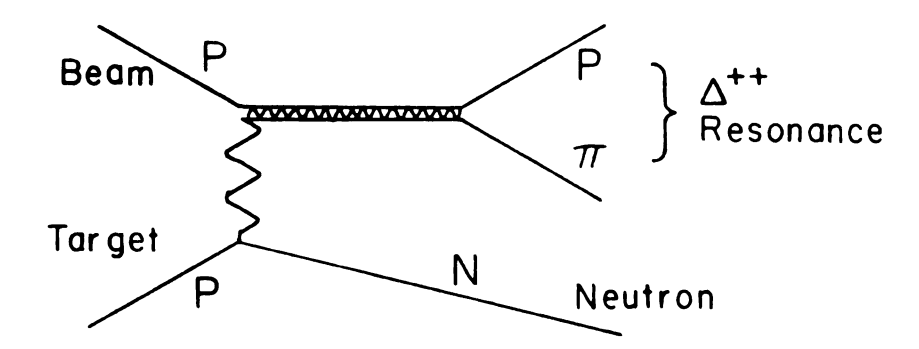


Figure 1.1. One pion exchange diagram.

The one pion exchange diagram for this reaction is shown in Figure 1.1. The beam particle is a proton and the virtual target is an off-shell pion residing in the pion "cloud" of the target proton. The beam proton collides with the virtual pion and imparts a momentum transfer t necessary to place the virtual pion on its mass shell. The final onshell proton and pion are then detected in the lab. This process has a high cross section at low t and $(P, \pi+)$ mass due to the presence of the $\Delta++_{1236}$ resonance.

The pole extrapolation technique is not necessary to obtain cross section data in the reaction described above. Experiments using pion beams colliding with protons have been done. The same resonance occurs in $\pi+P$ scattering where the pion is on its mass shell before and after the resonance is formed. The on-shell cross section has been measured to high accuracy. It is useful to do a pole extrapolation experiment using off-shell $\pi-P$ scattering data in order to check the validity of the extrapolation

process against the known correct results. If the method proves successful here, it will add credibility to cross sections obtained by extrapolating initial virtual states to the unphysical on-shell value where the on-shell data are not available, such as $\pi-\pi$ and $\pi-K$ scattering. 8

The experimental apparatus in this thesis was designed to detect one pion production at a beam momentum of 6 Gev/c resulting from pion-proton and proton-proton collisions. The apparatus was built by the University of Notre Dame in order to carry out pion-proton experiments.9 Subsequently, the experiment reported in this thesis on proton-proton collisions was carried out as a University of Notre Dame, Argonne National Laboratory, Michigan State University collaboration. Wire spark chambers using magnetostrictive wands were used to obtain the data. Scintillators were positioned so that only data from a certain event configuration would trigger the apparatus and cause a spark. When a spark occurred, scalars automatically digitized the location of the spark in the chamber and a computer was used to write the scalar information onto magnetic tape. The apparatus was triggered on events having one beam track and two outgoing tracks. Typically 15 events were written on tape during each 400 m sec beam burst. The experiment ran for 12 days at the Argonne Z.G.S. and 1.5 million triggers were recorded. The final sample of 50,000 single pion production events were identified after reconstruction and event type fitting using

the Michigan of the processing unbiased high is the subject the final even of the events neutron final pion-proton malarge number rections, thi date of the co

shape from a pion propagate factors associate extrapolation distribution different models if one section. The model, I the The Chew-Low

one pion exc

models intro

the extrapo.

The t

The processing and corrections necessary to obtain the unbiased high quality $\Delta ++$ sample used in the extrapolation is the subject of much of this thesis. Eighty percent of the final events have the PN $\pi +$ final state. Thirty percent of the events have the well known $\Delta ++$ 1236(3,3) resonanceneutron final state. These 14,000 $\Delta ++$ events occur at low pion-proton mass and low momentum transfer. Due to the large number of events and the good quality of the corrections, this thesis represents the most exacting test to date of the cross section extrapolation technique.

The t dependence of the cross section at a given mass is complicated. ¹⁰ The t distribution derives its shape from a combined contribution of the PNπ vertex, the pion propagator, ² the PπΔ++ vertex ¹¹ and dynamical form factors associated with the interaction. An accurate extrapolation of the data cannot be done unless the t distribution is linearized by normalizing the data with different models. It is sufficient to use form factor models if one wishes to extrapolate the total cross section. The models considered here are the Chew-Low model, ¹ the Dürr-Pilkuhn model, ¹² and Benecke-Dürr model. ¹³ The Chew-Low model considers only the kinematics of the one pion exchange where the Dürr-Pilkuhn and Benecke-Dürr models introduce additional form factors to help linearize the extrapolation curves.

CHAPTER II*

HARDWARE

The hardware for this experiment was constructed by the University of Notre Dame and will not be described in detail here. 9

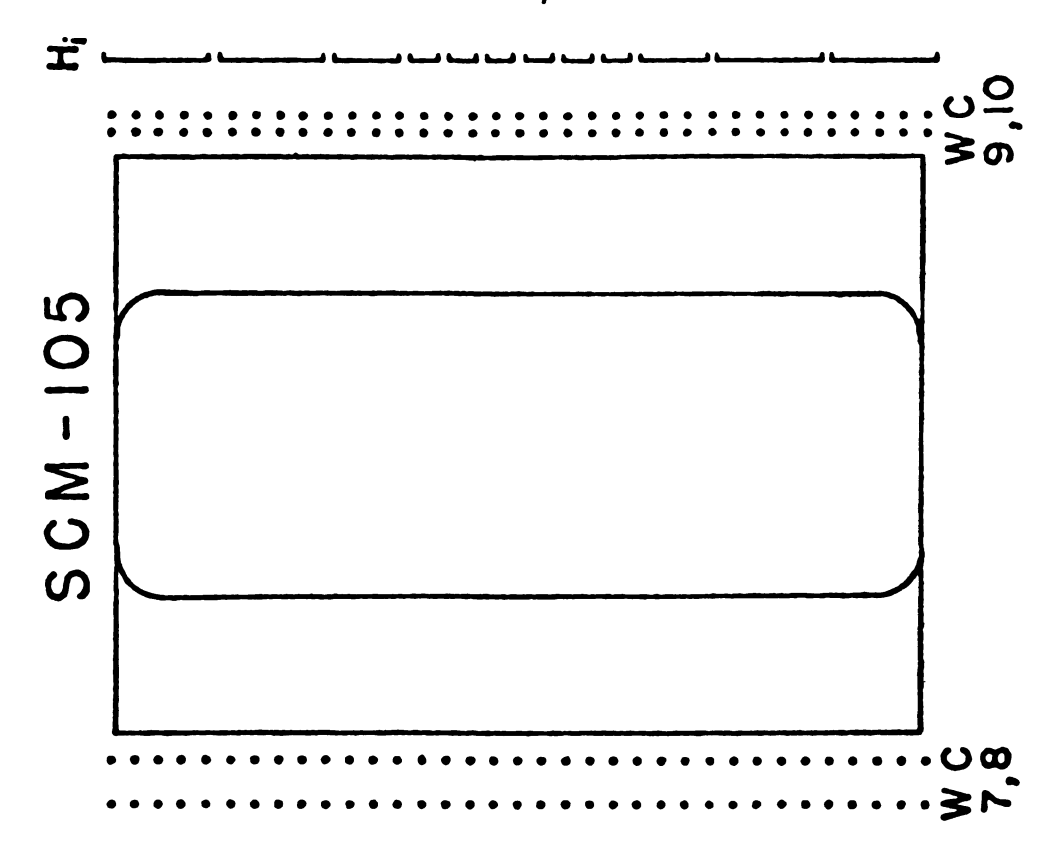
A proton beam of momentum $6 \pm .5\%$ Gev/c was focused and directed at a 6 inch long hydrogen target. The 20% pion beam component was identified by a Cerenkov counter. The counters used to trigger the apparatus are shown in Figure 2.1. A trigger was defined as \bar{C} B_1B_2 \bar{A} (D>2) H_1H_j where D>2 means two particles must hit the DE/DX counter and H_1H_j means two separate hodoscopes must fire. The DE/DX counter was 1/8" thick pilot F scintillator. The hodoscope array, shown in Figure 2.2, was designed using Monte Carlo events of the type $\pi^-P + \pi^+\pi^-N$ to have a high two track acceptance. The gross features considered in the Monte Carlo do not change when considering the reaction $PP + PN\pi^+$.

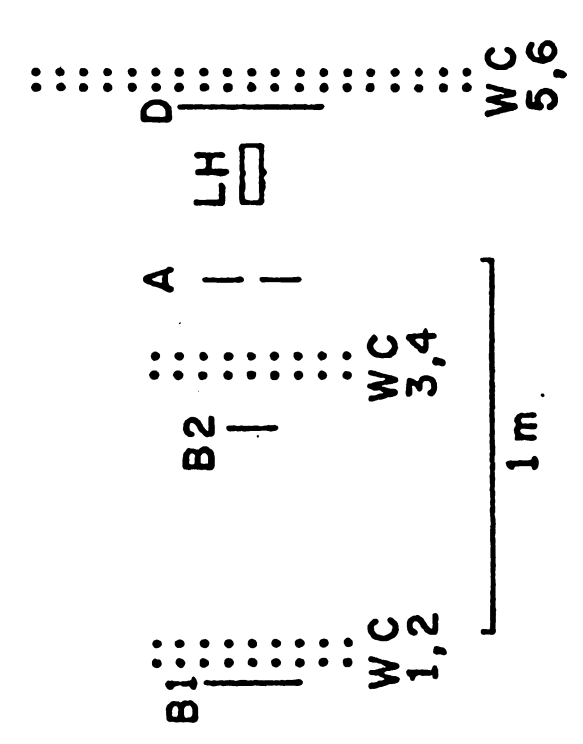
^{*}I am indebted to the University of Notre Dame for providing the apparatus and supplying the information used in this chapter.

Figure 2.1.

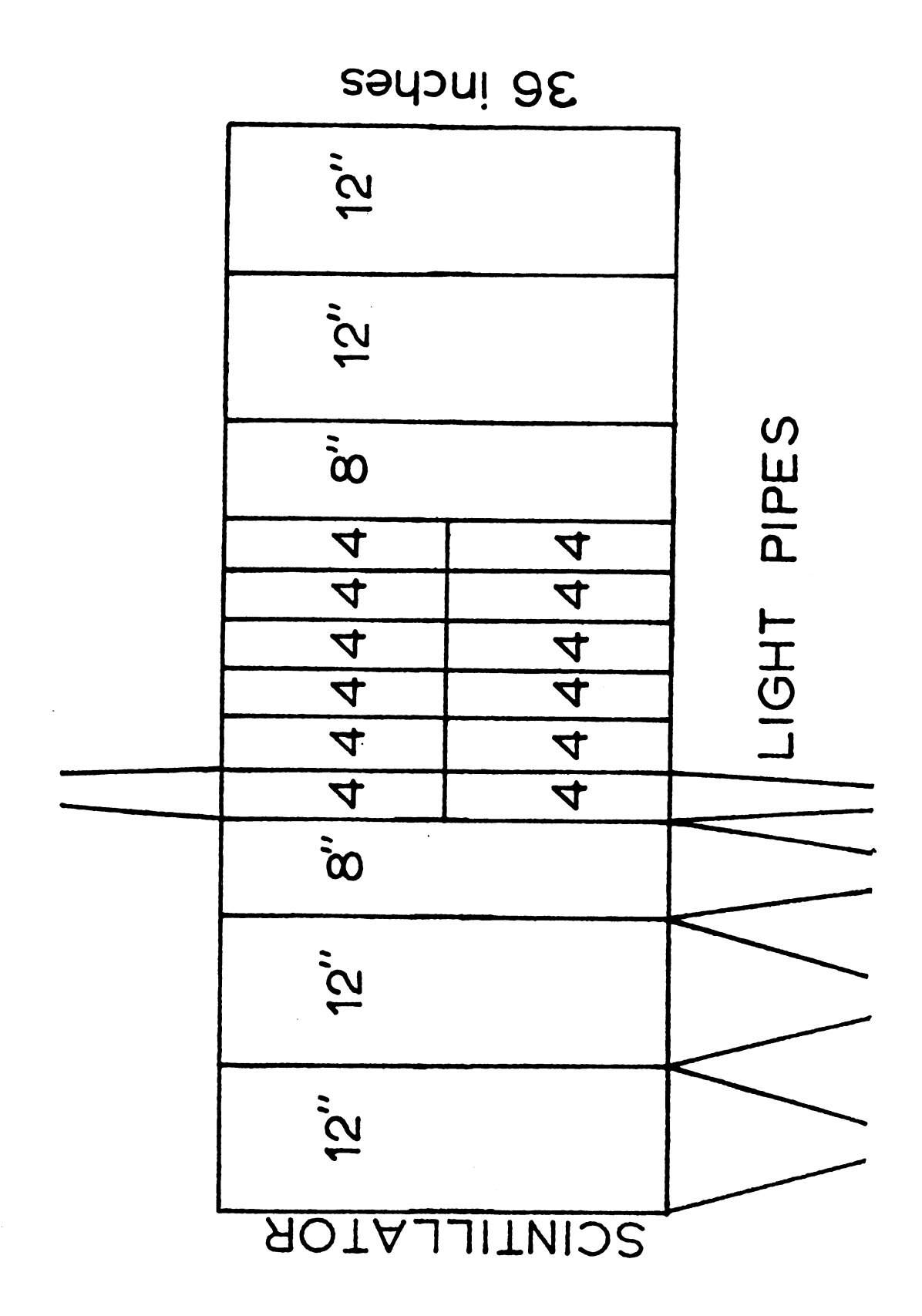
This diagram is an overall plan view of the experiment hardware. The dotted lines represent the position of magnetostrictive wire spark chambers. The solid lines represent the locations of the scintillation counters used in the trigger. The Cerenkov counter is 9 feet long and located about 20 meters further upstream.

SCM-105





The Hodoscope counter array is shown in a front view with lightpipes indicated. Shown are the 4 inch counters split at $\mathbf{Z}=0$ inches near the center and wider full length counters near the edges of the apparatus. Figure 2.2.



The c Dame and have wands. If 5 after a charg breakdown wou chamber wires magnetostric activated by rate of 20 M proportional total data f Varian 620/ construction for a two t have non-or Figure 2.3-

The chambers were wound at the University of Notre Dame and have 48 wires/inch crossing magnetrostrictive wands. If 5 kilovolts was applied to these wires shortly after a charged particle passed through the chamber, a breakdown would occur resulting in current flow in the chamber wires. The acoustical pulses resulting in the magnetostrictive ribbon were used to turn off scalers activated by a common fudicial pulse and counting at the rate of 20 MHZ. The scalar data for a given plane were proportional to the spark coordinate in one dimension. The total data from the 20 planes were read onto tape by the Varian 620/i mini-computer. Figure 2.3-b shows the chamber construction. Unambigous spacial location determination for a two track final states demanded that some chambers have non-orthoginal wire orientation. This is shown in Figure 2.3-a.

Figure 2.3a.

Diagram showing how the four layers of aluminum wires are applied to a chamber and where the magnetostrictive ribbons run.

Diagram showing details of the mechanical and electrical construction of the chambers. Figure 2.3b.

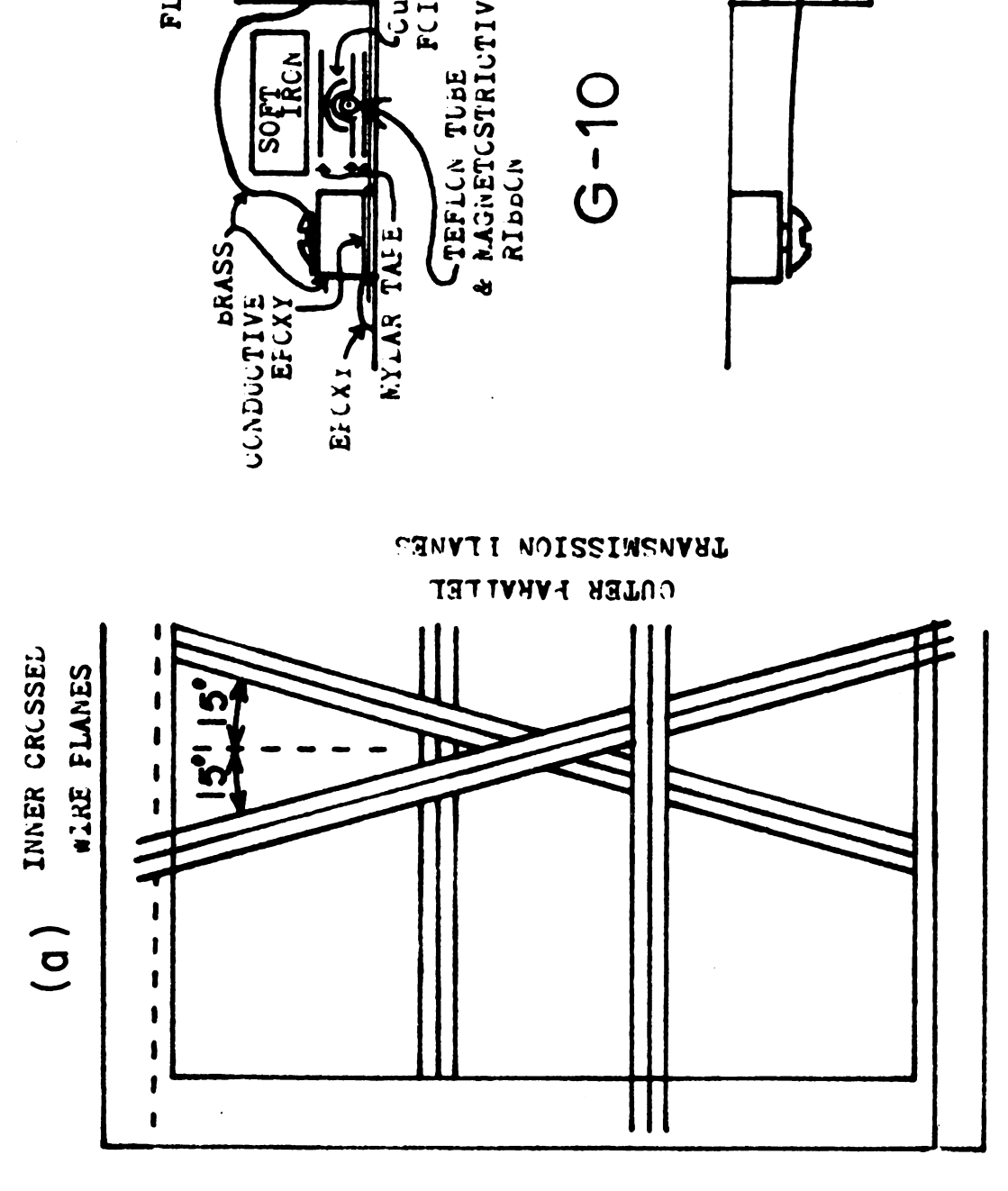
(p)

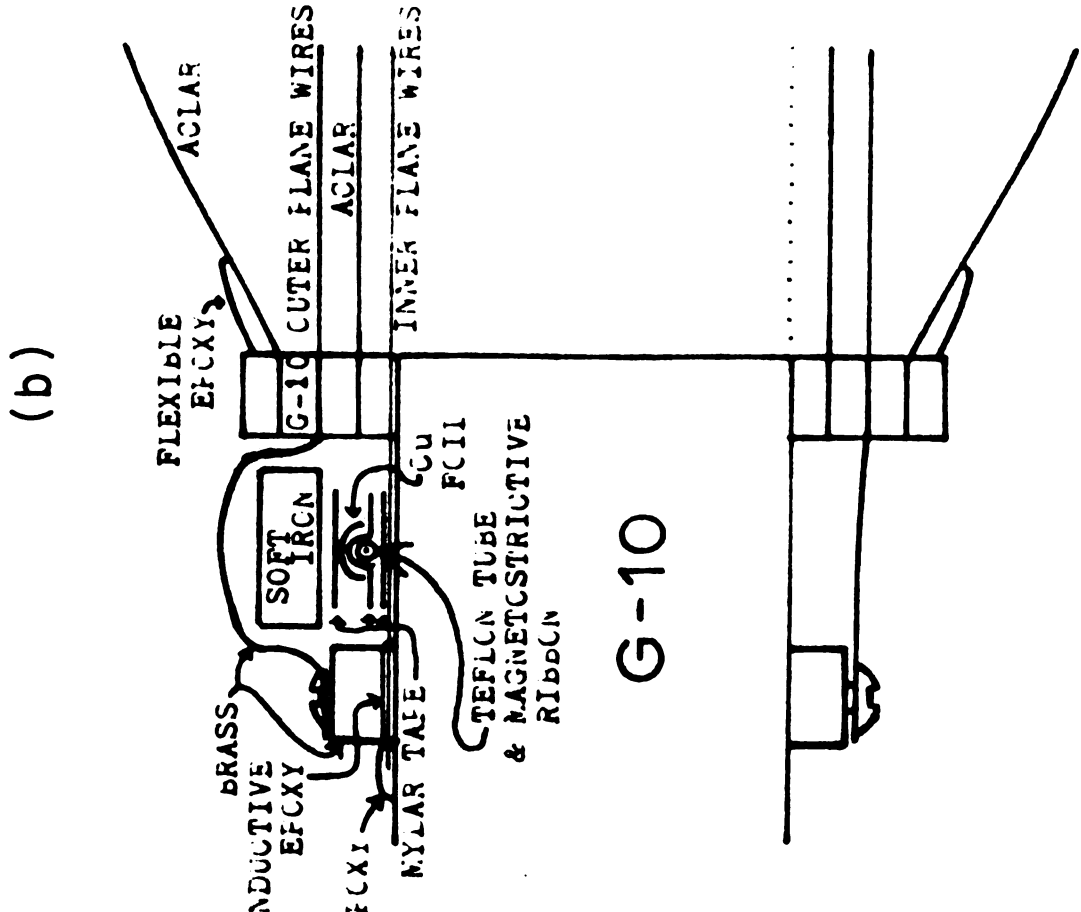
INNER CRUSSEL (0)

WIKE FLANES

T | | | | | | | |

FLEXIDIE





apparatus

GDH, whi

charged p;

anti-coun

gate, the

hodoscope

burst whi

computer

processed

T

Argonne z

D 460.95 R

B.B.Z.C A G

interaction

CHAPTER III

EVENT PROCESSING AND SELECTION

The experiment is divided into a roughly equal number of positive magnetic field and negative magnetic field triggers. A trigger is defined in terms of the apparatus described in Chapter II as: Trigger = B₁B₂C̄ Ā G D H, which means the beam counters have to count a charged particle, the Cerenkov counter does not fire, the anti-counter does not fire, the event occurs during the gate, the DE/DX sees two particles and two separate hodoscopes fire. There are typically 15 triggers per beam burst which are recorded on tape by a Varian 620/i mini-computer over the time span of 400 m sec.

Table 3.1 lists the total number of recorded and processed triggers obtained during the 12 day run at the Argonne Z.G.S.

Due to hardware problems discovered after the run, 460.95 K triggers were not analyzed. Also recorded are the $B_1B_2\overline{C}$ \overline{A} G \equiv BAG count. The sum of available protons for interaction from processed events is given in Table 3.2.

One can cal

1./(BAGpHNA

Table 3.2.-

BAG

₩/event

Th

the filter

tracks and the event.

Puter was

There were

was done w

9-20 and ti

in these p

further ove

given in Te

triggers to

Table 3.1.--Trigger Breakdown.

	Positive Field	Negative Field	Total
Recorded	970 K	950 K	1929 К
Processed	509.25 K	958.80 K	1468.05K

One can calculate the ub/event by the relation ub/event = $1./(BAG\rho_HNAL)$. This is also listed in Table 3.2.

Table 3.2.--BAG and ub/event.

	Positive Field	Negative Field	Total
BAG	51.1 Meg	88.2 Meg	139.3 Meg
ub/event	.03035	.01758	.01113

The 1468.05K good triggers were analyzed through the filter program Crunch, ¹⁴ which attempts to find two tracks and put out the X-Y-Z positions at the chambers for the event. The Michigan State University C.D.C. 6500 computer was used for all event processing and analysis. There were two separate analyses of the events. The first was done with events having 3 sparks per plane in planes 9-20 and the second pass included events which had 4 sparks in these planes. This effectively eliminates the need for further over-flow corrections. The Crunch results are given in Table 3.3. The overall 17% survival rate of triggers to Crunch out events is mostly due to the

inability of averaging seve failure class:

Appendix A.

Table 3.3.--E:

Pc

Pass 1

Pass 2

Circe designed for

experiment it

errors in the

out-going tr

angle for ea correlated e

system used

along the x

system is t

Summarizes

ou1

failure.

failures ar

inability of Crunch to find two good final tracks. After averaging several typical runs one can list the larger failure classifications and their losses. This is given in Appendix A.

Table 3.3.--Events Out of Crunch.

	Positive Field	Negative Field	Total
Pass 1	84433	146018	230451
Pass 2	3962	1884	5846

Circe is a general multi-prong computer program designed for a non-uniform magnetic field. 15, 16 For this experiment it was altered 17 to take the X-Y-Z values and errors in these quantities for the input beam track and two out-going tracks and return a curvature, dip and azimuth angle for each track as well as the vertex and a 12 x 12 correlated error matrix. The definitions of the coordinate system used in Circe is shown in Figure 3.1. The beam is along the x direction and the origin of the coordinate system is the geometric center of the magnet. Table 3.4 summarizes the events out of Circe.

Only 32% of the input Circe events fail. These failures are listed in Appendix A with the cause of failure.

Figure 3

Table 3.

Pass 1

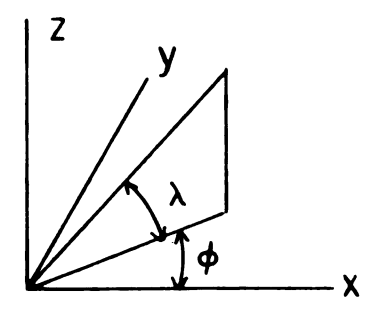
pass 2

three d

their ;

Table

Reacti



 $\lambda = Dip angle$

 ϕ = Azimuth angle

K = 1/P

Figure 3.1. Coordinate system used in Circe.

Table 3.4.--Circe Output Events.

	Positive Field	Negative Field	Total
Pass 1	60010	98812	158822
Pass 2	3181	1484	4666

Teuta¹⁸ attempts to fit the kinematic data for the three output tracks from Circe to event types given with their mark number in Table 3.5.

Table 3.5.--Teuta Fit Reactions.

Reaction Number	Mark Number	Reaction
la	4	PP→PNπ+
lb	104	PP→π+NP
2	2	PP→PPπ°
3		PP+∆++N
4	1	PP→PP

elastic scate geometry of the

stricting t<

Reac

ent reaction

If a

than 10⁻⁵, t

confidence :

the best co

correct rea

by requirir

event conf

selection

confidence

type is th

Appendix A

greater th

sidered go

events who

A, are li:

tesolves a

Reaction type 3 is a sub-class of la and lb restricting t<0.3 Gev^2 and 1.14<M_{p π}+<1.42 Gev. Reaction 4 is elastic scattering and can be shown to be impossible for the geometry of this experiment. No fits of reaction 4 were found. The confidence level distributions for the different reactions is shown in Figure 8.1a-d.

If a reaction type fit has a confidence level less than 10^{-5} , the fit information is not recorded. Fits with confidence levels between 10^{-5} and .03 are failures but are recorded. All fit types greater than .03 are good fits and the best confidence level of the good fits is taken as the correct reaction type. It was found that nothing is gained by requiring the usual factor of 2 or 3 between competing event confidence levels so a simple best confidence level selection rule is applied. The extent to which the best confidence level does not correspond to the true reaction type is the experimental ambiguity discussed in Chapter 8.4. Appendix A summarizes the events which have no fit type greater than 0.03 and are thus considered failures.

Teuta events with a confidence level >3% are considered good fits and are summarized in Table 3.6. The events which survive the target cut, discussed in Appendix A, are listed in Table 3.7. The last section of Table 3.7 resolves ambiguities by a simple best selection rule described earlier.

Tab Pa

Pa

Table 3.6.--Teuta Fits $C_T > 3%$.

	Positive Field	Negative Field	Total
Pass 1	18896	34105	53001
Pass 2	1180	621	1801

Table 3.7.--Good Teuta Events After Cuts.

Fit Mark	Pass 1	Pass 2
2	5177	153
4	9859	277
2 + 4	2857	83
104	8807	290
2 + 104	5731	132
4 + 104	15877	462
2 + 4 + 104	287	4
ΡΝπ+	39325	11146
РРπ°	9270	255
Δ++	14283	402
Total	48595	1401

cut plus sca correction f

In Ch

sample of ever

standard devi

events by the

events before

Table 3.8.-

Total Even

+#25

5540

4+2

a model h

for two t

podoscop, mental d

events to

final sa

In Chapter VIII it will be shown that a cleaner sample of events can be obtained if one applies a Circe standard deviation (S.D.) cut of 0.6 and scale up all Teuta events by the same number to conserve events. The total events before a S.D. cut, after a S.D. cut and with a S.D. cut plus scaling are given in Table 3.8. The S.D. cut correction factor is 1.29.

Table 3.8.--Final Events.

	No. Cut	Sol Cut =.6	Sol Cut + Scaling
Total Events	49996	38738	49996
PNπ+	40471	31908	41180
PPπ°	9525	6830	8815
Δ++	14685	12271	15837

The weighting program described in Chapter V uses a model hodoscope array to eliminate orbited orientations for two tracks which hit the same hodoscope or miss the hodoscope array. This cut was also applied to the experimental data for consistancy. This cut reduces by 270 events the $\Delta ++$ sample. This gives 12001 $\Delta ++$ events in the final sample.

T'

and the r

values as

The zero

planes w

the begi

magnet o

the sam

spark F

separa

is the

given

fitted

values

CHAPTER IV

ZERO VALUE AND BEAM MOMENTUM

4.1 Zero Value

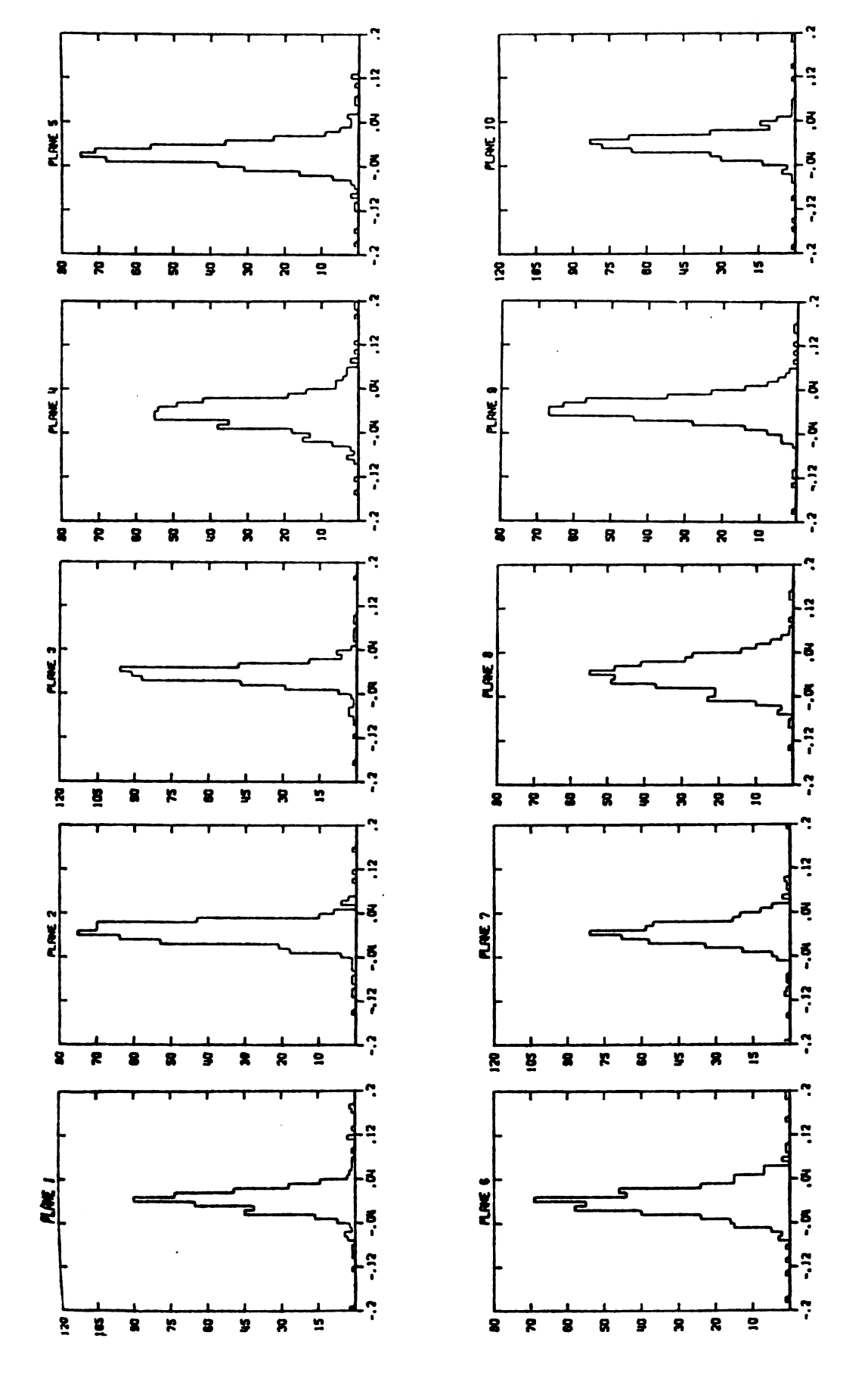
The 20 spark chamber planes were surveyed into place and the relative centers of the various planes were roughly determined with respect to the beam tracks. The initial values as determined by this survey are given in Table 4.1. The zero value is the center to start distance in inches.

To determine the actual zero values for the 20 planes with respect to the beam, data runs were taken at the beginning, middle, and end of the experiment with the magnet off and the trigger set for single beam tracks.

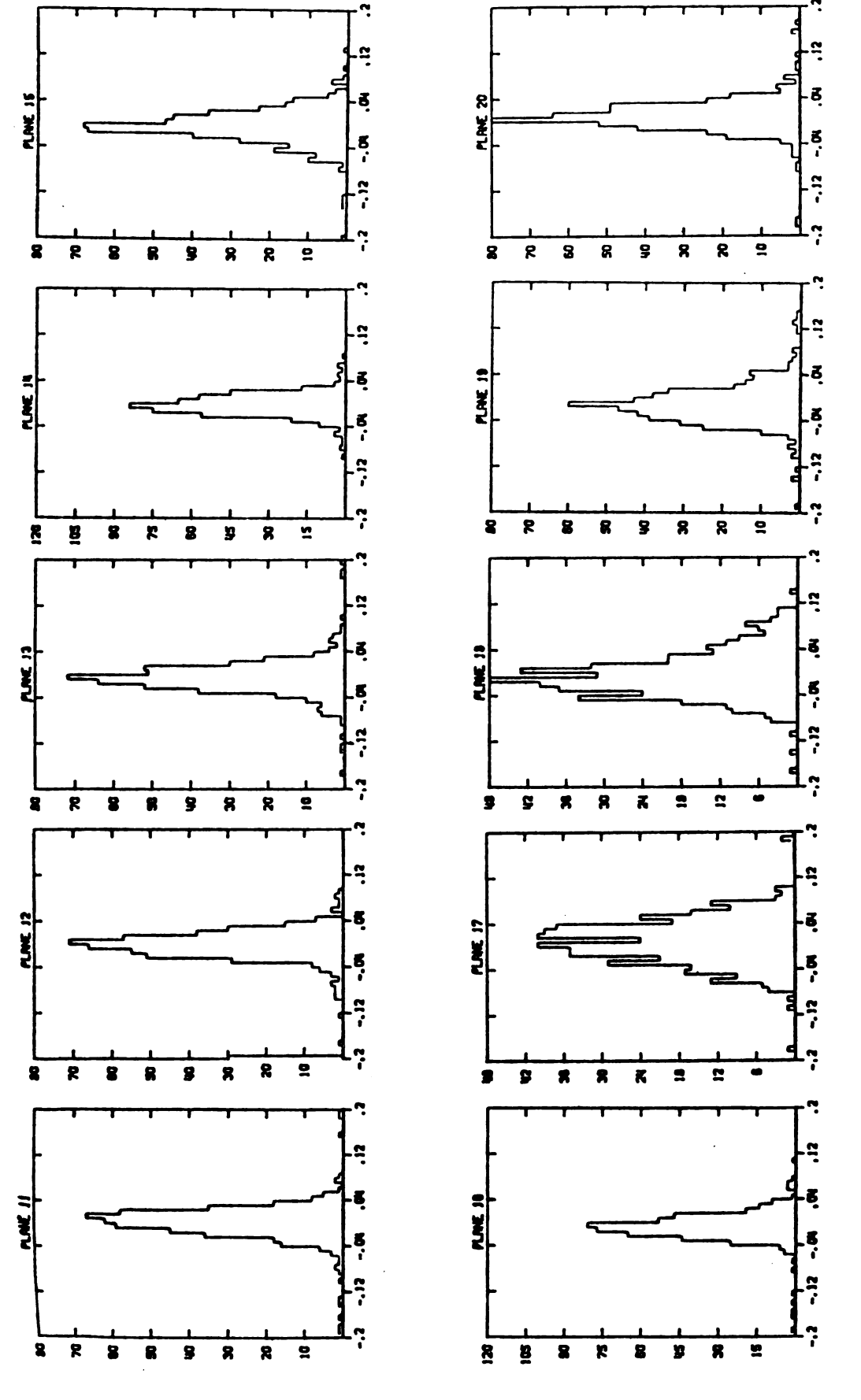
The data used for zero value are processed through the same spacial reconstruction routine as real event triggers. Only straight through tracks with exactly one spark per plane are examined. The Y and Z views are separately fitted to a straight line. The final zero value is the average fitted beam position in the chambers and is given in Table 4.1. The widths and displacements of the fitted beam position with respect to the surveyed zero Values are shown for the 20 planes in Figure 4.1. These

2 2 2 2

The twenty distributions shown in this figure are the fitted minus measured beam track positions for the 20 spark chamber planes used in this experiment. The horizontal scale is inches. Figure 4.1.



VERTICAL IS NUMBER OF EVENTS HORIZONTAL AXIS IS FITTED MINUS MEASURED IN INCHES



VERTICAL IS NUMBER OF EVENTS HORIZONTAL AXIS IS FITTED MINUS MEASURED IN INCHES

Table 4.1.--Initial and Final Zero Values.

	Initial Zero Value	Final Zero Value
1	7.537	7.537
2	7.793	7.796
3	7.537	7.540
4	7.801	7.802
5	7.769	7.766
6	7.547	7.541
7	7.540	7.540
8	7.801	7.797
9	16.475	16.470
10	16.787	16.782
11	16.785	16.787
12	16.588	16.586
13	14.766	46.738
14	46.366	46.367
15	43.290	43.291
16	18.958	18.967
17	43.218	43.220
18	18.955	18.953
19	47.014	47.008
20	46.478	46.477

distri ning o

simila

be 6.0

analys field

tracks

and th

B deta

A Mont

the 10

fittin

listed

Table

Gev/c

6.0

6.0

2.0

fittin

distributions use the magnet-off data taken at the beginning of the experiment. The other magnet-off data give similar distributions.

4.2 Beam Momentum

The beam momentum was determined experimentally to be 6.0 (± 0.5%) Gev/c using a dipole magnet and a momentum analysing slit. 9 As a consistency check on the magnet field fit and the beam momentum determination, single beam tracks with the magnet on were tracked through the magnet and the momentum width and center was determined. Appendix B details the fitting program used to fit the beam tracks. A Monte Carlo program was used to generate X-Y-Z values in the 10 chambers to simulate beam tracks as a check of the fitting program. The results of the fitting program are listed along with the input values in Table 4.2.

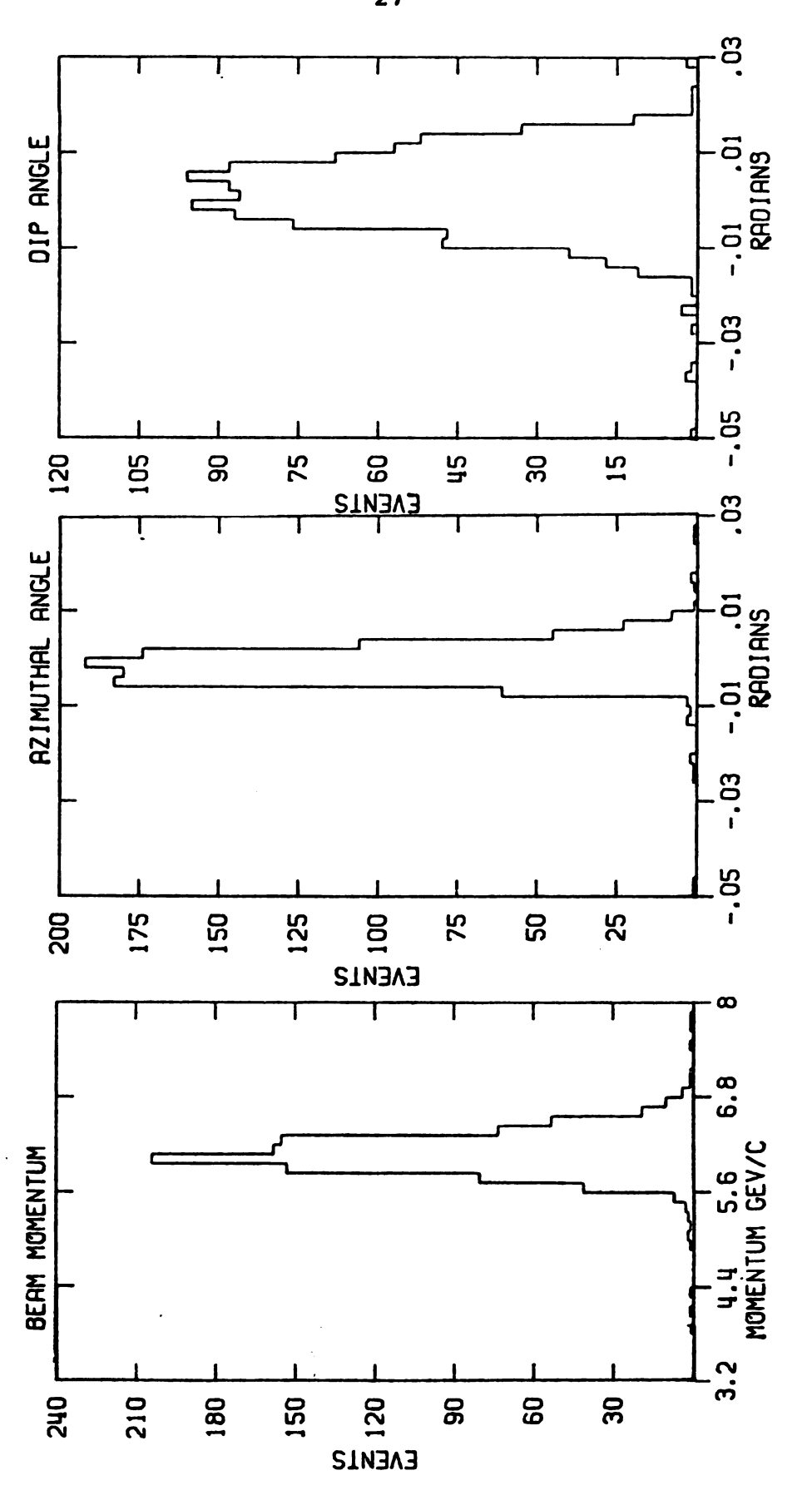
Table 4.2.--Beam Fitting Program Test.

Input Track		Output Track			
P Gev/c	λ Rad	φ Rad	P Gev/c	λ Rad	φ Rad
6.0	0.	0.	5.993	0.006	.000
6.0	.018	.024	6.010	.010	.020
2.0	03	08	1.999	.030	080

Only single perfect beam tracks were used when fitting the data. Figure 4.2 shows a plot of the fitted

Fitted beam momentum and angles using data runs triggered on single beam tracks. Figure 4.2.





centered at
This width i
come from th
These are th
As a

For all pla a width of

field-beam m

a chamber sa

beam momentum and angles. The beam momentum is seen to be centered at 6 Gev/c with a width (FWHM) of 0.5 Gev/c.

This width is roughly consistant with error expected to come from the wire spacing using planes 8 through 20.

These are the planes after the target.

As an additional check on chamber center values and field-beam momentum values coupled with the possibility of a chamber sag or rotation, the Y and Z fitted minus measured coordinates were plotted for magnet on beam tracks. For all planes, these values are centered on zero and have a width of 0.002 inches.

CHAPTER V

ACCEPTANCE

5.1 Geometrical Acceptance

The apparatus as described in Chapter II is designed to have no uncorrectable acceptance losses for reaction number 3. The degree to which this is not true is the subject of section 5.2. The apparatus does have a limited acceptance for reaction numbers 1 and 2. This limited acceptance arises from the wider angle and slower momentum data which comes from 2 and 1 as compared to 3. By designing the spectrometer length and field to be unbiased only for 3, better resolution for this reaction can be achieved.

Not all events of type 3 can make a successful trigger. Due to the rectangular shape of the magnet having limits of ±44 inches in Y and ±13.5 inches in Z, not all events in the X-Z plane survive to the hodoscope. However, the larger X-Y plane acceptance insures that wide angle events are recorded in this orientation, and the losses from the vertical orientation are related by a rotation about the beam axis. A weighting program has been written

to assign each event an acceptance weight equal to the inverse of the probability of detecting the event.

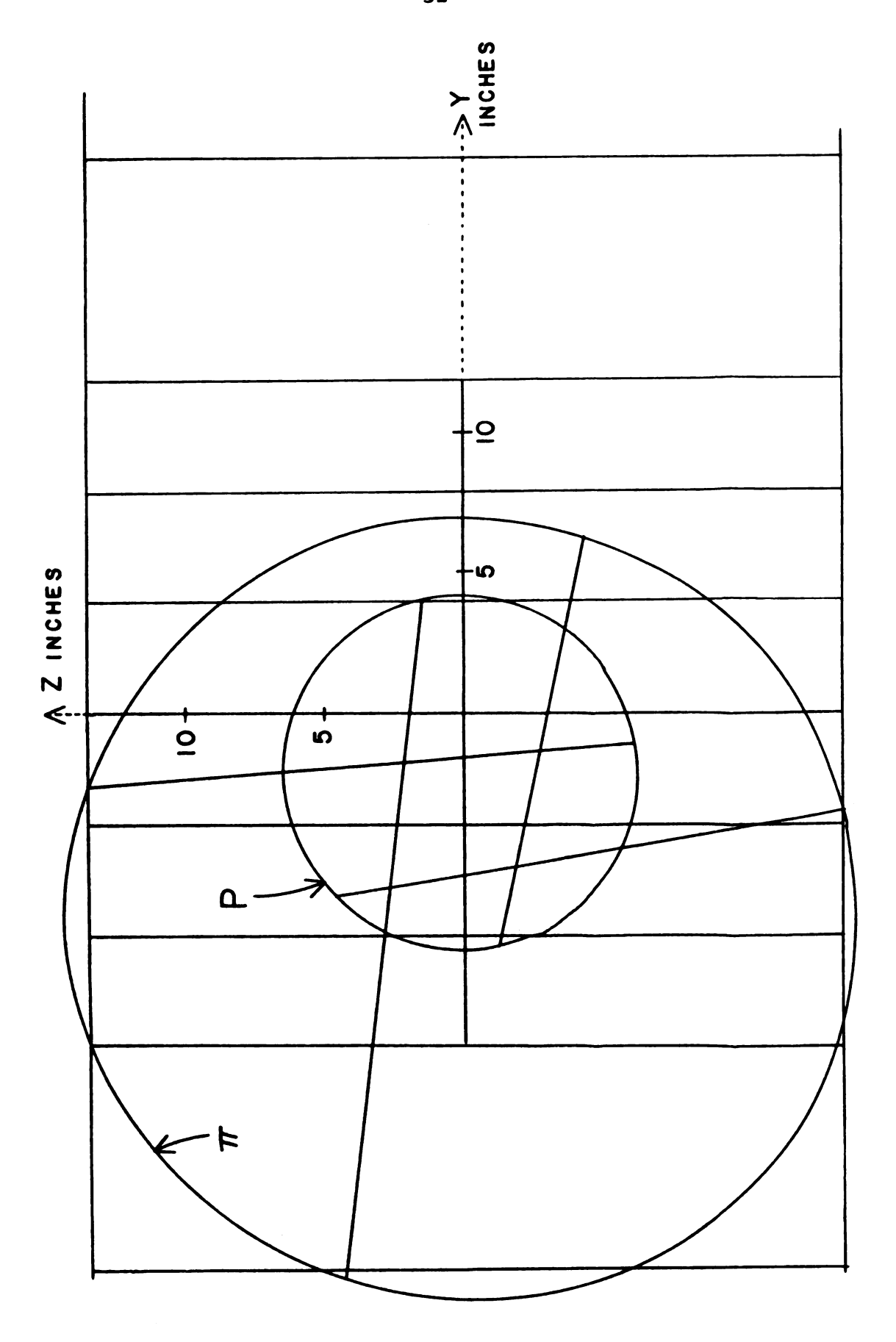
The acceptance program assumes axial symmetry along the X axis. Each of the two outgoing tracks is rotated together about the X axis in 100 steps of 0.0628 radians and the number of times both pass through the magnet and hit the hodoscope is recorded. The acceptance is defined as the hits divided by the total number of steps. The magnet cuts made are $Y = \pm 44$ inches and $Z = \pm 13.5$ inches. The hodoscope is defined as $Y = \pm 44$ inches and $Z = \pm 18$ inches. Also, since actual events require two or more hodoscopes to fire, an event orientation is not counted as a hit if both tracks hit the same hodoscope.

A typical event weighting process is pictured at the hodoscope plane in Figure 5.1. The event shown has the characteristics given in Table 5.1. The outer circle is the pion and the inner the proton. The solid lines connecting the circles are various pion-proton relative position on the circles.

Table 5.1.--Typical Event Weighting Process.

	_p Gev/c	λrad	φrad
Pion	1.46	.0076	.1208
Proton	4.39	.0298	0470

Figure 5.1. Typical event weighting process.



The total number of the moment to neutron, and

It i

Yang angles.

before and a

less of the

back by the

previous se

acceptance

four dimens Possible ra

map M - t -

described i

 $^{ ext{type}}$ can be

is a bias a the bias ge

is a bias ;

The total number of hits for the event shown is 84, giving an acceptance of 0.84 and a weight of 1.19.

Only events of reaction 3 are weighted. Appendix C defines the four independent variables used throughout this analysis. These are the invariant mass of the $p\pi$ + system, the moment transfer squared from the target proton to the neutron, and two Δ ++ decay angles, the Jackson and Treiman-Yang angles. Figure 5.2a-d shows these four variables before and after weighting. The average weight is 2.35.

5.2 Zero Acceptance

It has been found that at 6 Gev/c incident proton momentum, the apparatus described in Chapter II will have zero acceptance for some events of reaction type 3 regardless of their orientation. This loss cannot be corrected back by the normal weighting procedure described in the previous section.

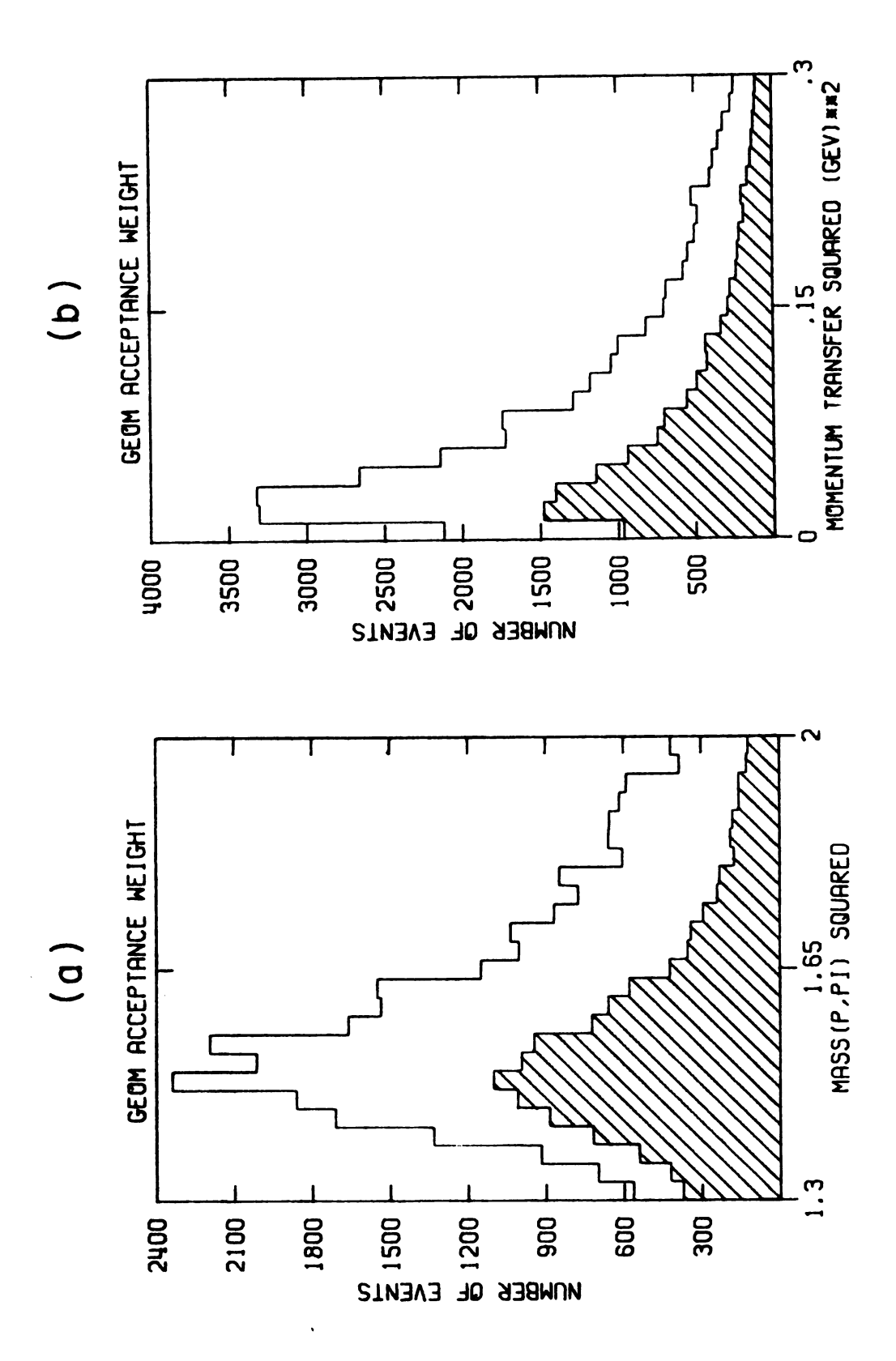
In order to understand the nature of the zero acceptance region with respect to M, t, $\theta_{\rm Jac}$, and $\phi_{\rm TY}$, a four dimensional grid of data can be generated covering the possible range of these variables. The function used to map M - t - θ - ϕ points to proton and pion tracks is described in Appendix C. The acceptance for each event type can be calculated. This investigation reveals there is a bias against low Treiman-Yang angle for low mass and the bias gets larger with increasing mass. It shows there is a bias against low Jackson angle, especially at high

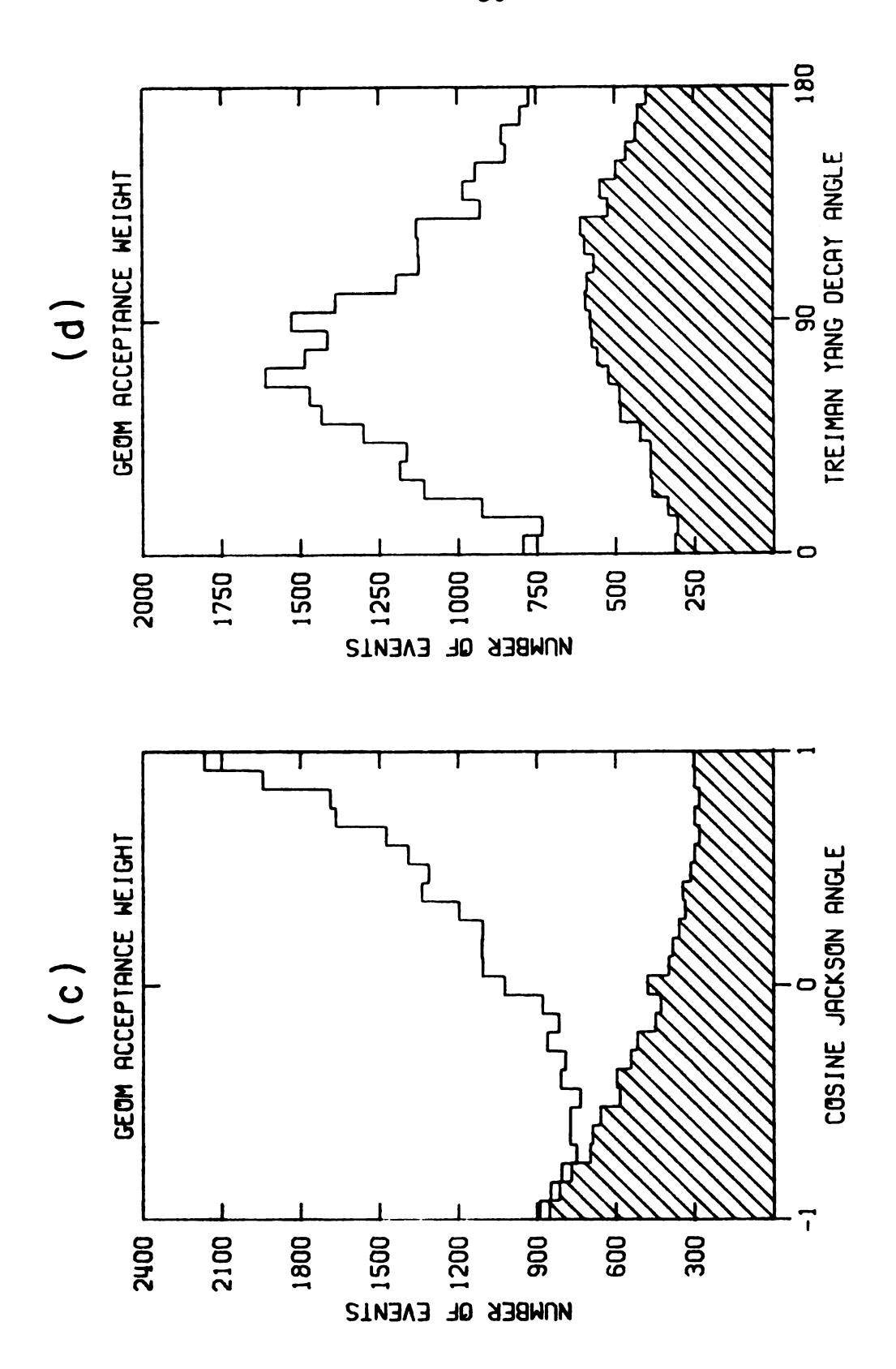
a-d show the mass squared of the pm+ system, the momentum transfer squared, the Jackson angle and the Treiman-Yang angle distributions respectively. The distributions are shown before weighting shaded and after weighting unshaded. Figure 5.2.

GEOM ACCEPTANCE WEIGHT (p) 000h (0)

GEOM ACCEPTANCE WEIGHT

2400





Mass.

a great

explain

region

of the

mass.

the ac

transf

by the

of the

Carlo

the La

descri

of 1.

obtair

The ze

Events

inves

tracke

corre

1.14.

vith ,

the h

there corre

Polat

mass. The bias gets larger at high mass, but does not have a great dependence on momentum transfer. Appendix D explains physically the cause of the zero acceptance region. Figure 5.3a-b shows the three dimensional location of the zero acceptance region as a function of θ , ϕ and mass. The indentation in the lower right corner is where the acceptance is zero. Figure 5.3a-b are at momentum transfer squares = 0.04 Gev² and 0.12 Gev² respectively.

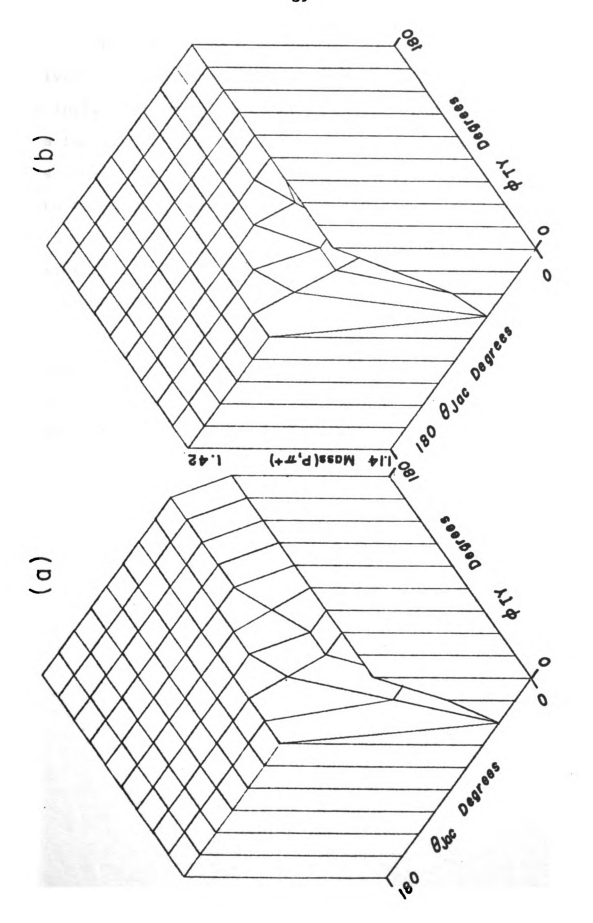
In order to correct for the zero acceptance exhibited by the apparatus to certain data regions. Monte Carlo events of the type PP+P π +N were generated at 6 Gev/c. The Monte Carlo program is described in Appendix E. The events in the A++ region are tracked and weighted for acceptance as described in section 1 of this chapter. Using a mass cut of 1.36 Gev, 1580.7 tracked and weighted events are obtained from an original Monto Carlo sample of 1756 events. The zero acceptance correction in this mass range is 1.1109. Events with the larger mass range up to 1.42 were also investigated. Out of 2001 Monte Carlo events, 1752.3 tracked and weighted events result from the acceptance correction. This gives a zero acceptance correction of 1.14. The zero acceptance correction is similar for data with the mass cut-off at 1.36 and at 1.42 because, although the higher mass does have a marked decrease in acceptance, there are fewer events on which this has an effect. The correction factor of 1.1109 was used for the pole extrapolation analysis.

Three dimensional plot of the zero acceptance region. Points inside the cube have correctable acceptance losses. The indentation occurs where the acceptance is zero. The t value is 0.04 Gev² for a and 0.12 Gev² for b. Figure 5.3a-b.

.04 Gev² for a and 0.12 Gev² for b.

(P)

(0)



derived

the ini

as a fi

to scal

Monte (

for th

Parame

the ra

fitted

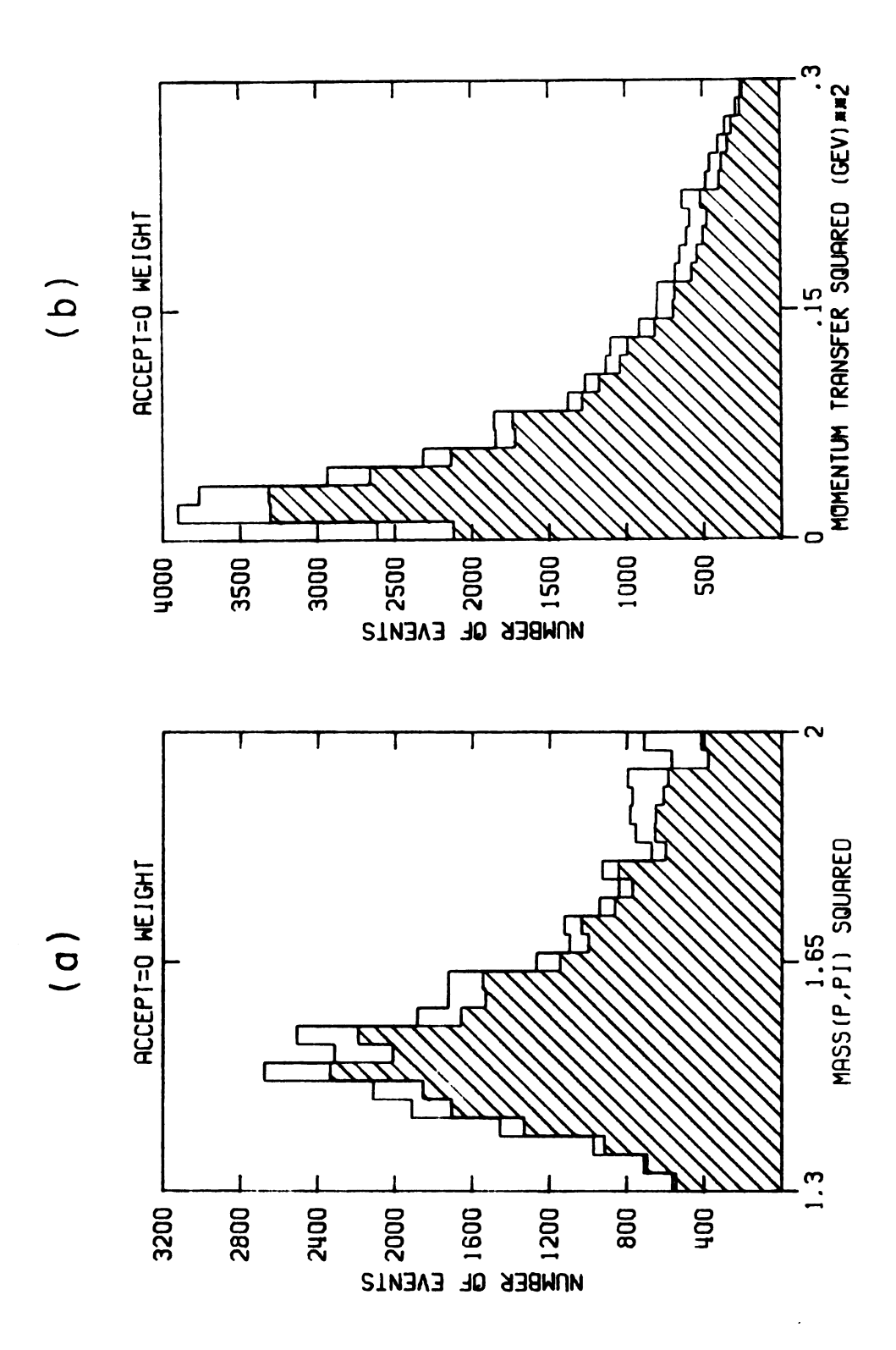
CILAG

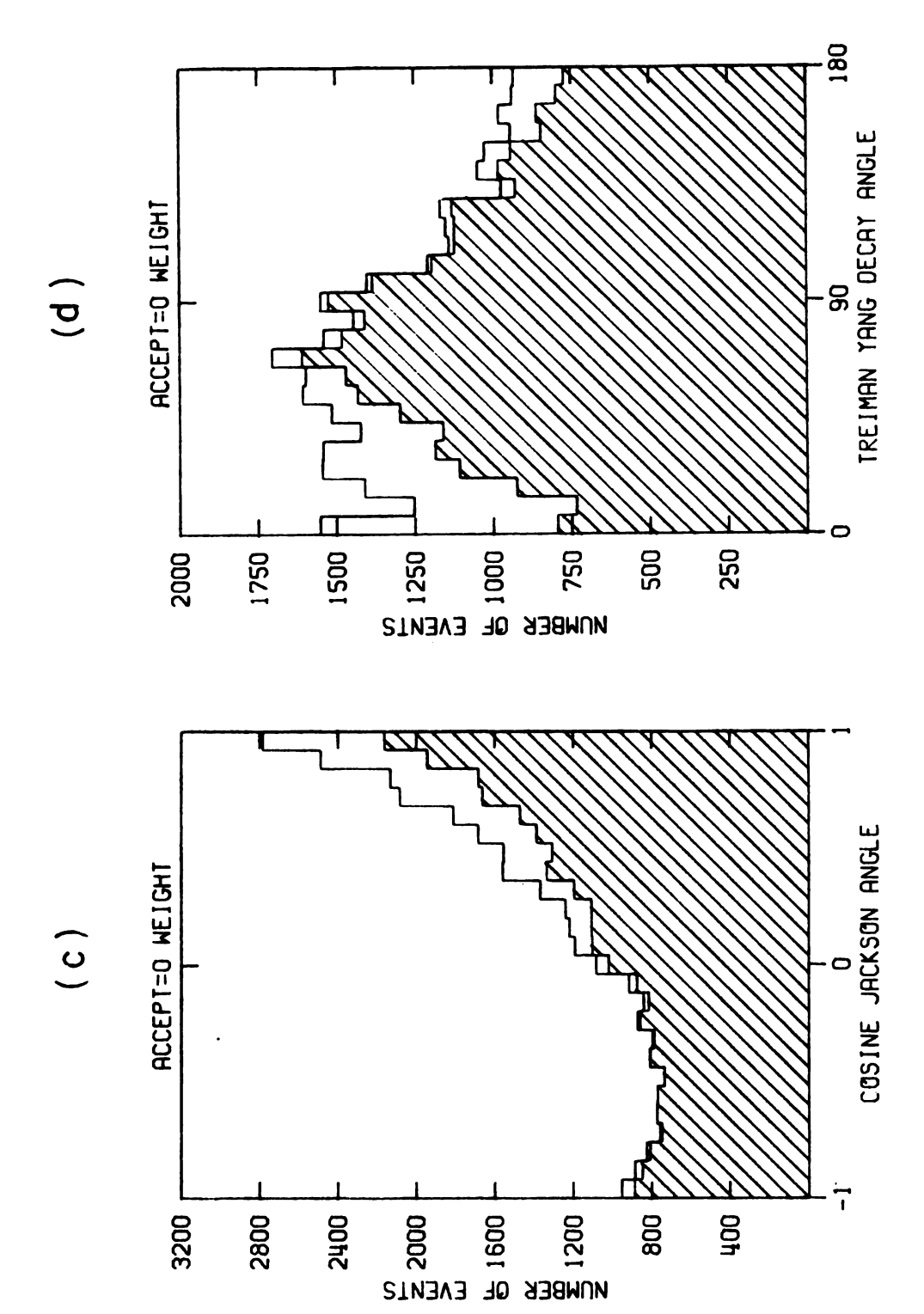
calae

The actual shape correction factors used were derived in a manner which does not drastically depend on the initial distribution. An efficiency curve was derived as a function of the M, t, $\theta_{\rm Jac}$, and $\phi_{\rm TY}$ variables in order to scale-up the distributions where it is necessary. The Monte Carlo data were broken up into 10 bins of equal size for the mass, t, $\theta_{\rm Jac}$, and $\phi_{\rm TY}$ of the event and a four parameter fit of the form A + BX + CX² + DX³ was made to the ratios of the ten bins before and after track-weighting.

Figure 5.4a-d shows the effect of multiplying the fitted curve by the actual experimental data. The shaded curve is the original uncorrected data, and the unshaded curve is the final data corrected for the zero acceptance.

Final experimental data shown before (shaded) and after (unshaded) zero acceptance correction. Figure 5.4a-d.





travel hodosc

Which

may be

^{be} rej the pi

 ${\tt decay}$

Fr

Carlo

track

four-

size

CHAPTER VI

PION DECAY AND SECONDARY SCATTERING

6.1 Pion Decay

Pions resulting from the reaction PP+P π +N will travel approximately 116 inches before hitting the final hodoscope. A decay of the type π ++ μ + ν will produce a muon which can usually traverse the apparatus, but its momentum may be sufficiently different from the pion to cause it to be rejected by the fitting programs. The correction for the pion decays will then be the fraction of pions which decay and make a wrong fit. This is written as:

Fraction of Pions lost =
$$\left(\frac{\text{Decayed pions}}{\text{Tracked events}}\right) \left(\frac{\text{Bad fits}}{\text{Decayed pions}}\right) (6-1)$$

A track decay program is written which uses Monte Carlo $PN\pi+$ events as described in Appendix E. The pion is tracked from the target to the hodoscope in approximately four-inch steps. The probability for decay in each step size ls is then

$$P_{Decay} = 1 - exp(^{-1s}/Lm)$$
, where $Lm = BC \gamma T \pi$ (6-2)

For

a ra

P Dec pion

char

is t

tinu

MUON

outgo types

deter

mate]

stati time.

analy

found

i++ c

decay

restr Y and

exper

gives

track:

 t_{euta}

For a 2 Gev/c momentum pion, L_m is about 4400 inches. If a random number generated between 0 and 1 is less then P_{Decay}, a muon is assumed to emerge isotropically in the pion rest frame back to back with a neutrino, each with the characteristic momentum of 30 Mev/c. The muon four momentum is transformed back to the laboratory and allowed to continue tracking.

The various X-Y-Z positions for the proton and muon can be recorded at the chamber positions. The two outgoing tracks are then reconstructed and fit for event types by Circe and Teuta and a fitting efficiency is determined. These severely altered tracks take approximately 20 seconds each for Circe processing alone, and the statistics on this analysis are restricted by computer time. Table 6.1 summarizes the events generated in this analysis. The total events generated was 15290. It was found that 4.03% of all tracked events decay, while if a Δ++ cut is made 4.66% of the events decay. This higher decay number results from the fact that the $\Delta++$ cut restricts the sample to only slow pions which have reduced γ and $\mathbf{L}_{\mathbf{m}}.$ The final 12001 $\Delta + +$ events obtained from this experiment can be tracked on the individual basis. gives an average decay probability of 4.56% for the pion tracks.

Table 6.2 indicates the results of the Circe and Teuta fitting program on the 100 tracked decayed events.

Tab

A11

Эес

Of

swa dec.

Tab:

100

97

91

77

41

10¹⁹

the a

that

small

nult

³⁰ a

Table 6.1.--Pion Decay Events.

	Tracked Events			
All Events	No Δ++ cut 2508	Δ++ cut 1179		
Decays	100	55		

Of the 77 fits with a confidence level greater than 3%, 15 swap to Mark 2 and 21 swap to Mark 104. The combined pion decay correction is $(4.66) \left(\frac{59}{100}\right) = 2.75\%$.

Table 6.2--Pion Decay Track and Fit Results.

100	Decayed Events
97	Pass Circe
91	Pass Teuta (confidence level >10 ⁻⁵)
77	Pass Confidence level cut of 3%
41	Fit as PNπ+

6.2 Electromagnetic Scattering

When a charged particle penetrates an absorber, it may instantaneously experience electric fields as high as 10^{19} volts/mtr due to the nuclei of the atoms which make up the absorber. For thick absorbers, the chances are good that the charged particle will undergo a large number of small-angle coulomb scatterings in a process called "multiple scattering." In addition the particle may undergo a single relatively large angle scatter with a

proba

•

The t

scatt

numbe

the '

obta

ary

divi

targ The

last

asso

mat

can

gve

gre gre

ela

The

āþi

val

eve

37,7

probability given by the Rutherford scattering formula. The transition region from multiple scattering to single scattering is known as a plural scattering because the number of collisions is larger than 1 but not very large. A precise formulation for the electromagnetic scattering in the three physical domains described above has been used to obtain the scattering angular distributions for the secondary charged particles in this experiment. 19, 20, 21

The matter seen by the secondary particle can be divided into three regions. The first region includes the target, DE/DX and chambers 5 and 6 plus the associated air. The second region includes chambers 7 and 8 plus air. The last region only includes air. These regions and their associated material are listed in Table 6.3. This material can be summarized in Table 6.4. The x position of the material is assumed to be concentrated at the weighted average position of the material in the region.

The Monte Carlo program described in Appendix E is used to generate good $PN\pi+$ events. The two outgoing tracks are tracked through the apparatus and are allowed to elastically scatter in each of the three regions of matter. The two final outgoing tracks have up to three scatters apiece as they traverse the system. The various Y and Z values at the spark chamber planes are recorded and the event is processed by Circe and Teuta. The results of the analysis of 200 Monte Carlo events are given in Table 6.5.

Table

Regio

1

2

3

Table 6.3.--Break-down of Secondary Matter

Region	X Inches	Description
	-74.56	Hydrogen target3" hydrogen
1	-73.06	Hydrogen target wall and vacuum window02" CH ₂
	-70.0	DE/DX1/8" CH ₂
	-70.0	50 mil tape with DE/DX
	-66.4	Chamber Aclar03" CH ₂
	-66.4	Al wires0072" effective width for 2 chambers
	-60.0	Air26" nitrogen
2	-34.9	Chamber Aclar03" CH ₂ for 2 chambers
	-34.9	Al wires0072" effective width for 2 chambers
	-28.	Air45" Nitrogen
3	10.	Air45" Nitrogen

Table

Regio

Tab:

Table 6.4.--Chemical Break-down of Material.

Region	Average x	Element	Z	A	g/cm ²	nuclei cm ² × 10 ²³
1	-71"	H C Al	1 6 13	1 12 27	.659 .45 .0495	3.95 .225 .011
2 .	-32"	N H C	7 1 6	14 1 12	.079 .01 .0602	.0339 .06 .0301
3	10.	Al N N	13 7 7	27 14 14	.0495 .137 .137	.011 .0587 .0587

Table 6.5.--Coulomb Scattering Event Analysis.

<pre>199 Pass Circe 199 Pass Teuta (confidence level >10⁻⁵) 199 Pass 3% confidence level cut 186 Fit as PNπ+</pre>	200	Scattered Events
199 Pass 3% confidence level cut	199	Pass Circe
	199	Pass Teuta (confidence level >10 ⁻⁵)
186 Fit as $PN\pi$ +	199	Pass 3% confidence level cut
	186	Fit as $PN\pi+$

of 4 w

total

events

swappi

scatte

the st

the no

betwee

secti

actio

scatt

nucle

eight

gug e

secon

in th

confi

inter

scatt

P(A,

expa

The thirteen lost events which pass Teuta consist of 4 which fit as Mark 2 and 9 which fit as Mark 104. The total events loss is 7%. It is known that the Monte Carlo events with no modification will lead to a 4% ambiguity swapping of events. The total loss due to the coulomb scattering is taken to be the difference of 3%.

6.3 Strong Interaction Correction

Events of the type PP+Pπ+N will be degraded due to the strong interaction of the secondary proton or pion with the nuclear matter present in the experimental apparatus between the target and the final spark chamber. This section will estimate the magnitude of the strong interaction loss using experimental results of proton and pion scattering on hydrogen, carbon, aluminum, and nitrogen nuclei.

The corrections which results from each of the eight reactions above can be further divided into inelastic and elastic contributions. Good events which produce secondary inelastic strong interactions are entirely lost in the target or charge cut in Circe or a missing mass confidence level cut in Teuta. Elastic secondary strong interactions are also lost due to the magnitude of the scattering angle.

One can estimate the nuclear form factor by $F(A,t)=\rho^{-B\,|\,t\,|}, \text{ with } B=R^2/4\tilde{h}^2. \text{ This is the small argument}$ expansion of the form factor expected for the diffraction

by a

form

Esti

ment

will

firs trac

ela

Par

Car

g g

gen

Tet

Ta:

•

3

10 40

٥٥

10

by a spherical black body of radius R. The optical model form is

$$F^{2}black body = \left\{\frac{2 J_{1}(R/\hbar\sqrt{|t|})}{R/\hbar\sqrt{|t|}}\right\}^{2}$$
 (6-3)

Estimates of the B parameter were made using the experimental data and using only the first diffraction peak. It will be shown that the relatively low angle scatters in the first peak are still too distorting on outgoing event tracks to allow many events to be correctly fitted. P-P elastic scattering at 5 gev is known to fall with a B parameter of about 8.⁵, ²² The B parameter is about 90 for carbon and 100 for aluminum. ²³⁻²⁶ For pions on carbon the B parameter is about 60.²⁷ Elastic scatter events were generated for protons and pions with a B of 10, 40, and 90 and the scattered events were processed by a Circe and Teuta. Table 6.6 summarizes the results of this analysis.

Table 6.6. -- Strong Elastic Scattering.

В	Track	Elast. Scat.		Pass Teuta conf. lvl. >10-5	Conf. lvl. >.03	Good PNπ+
10	P	50	48	35	17	7
40	P	50	50	45	38	10
90	P	50	50	46	43	15
10	π	50	47	34	20	8
40	π	50	50	42	29	9
90	π	50	50	46	26	18

gets 1

it nev

ratio one-th

of eve

Also

Which

havin

reaso

matel

and p will

nucle Table

cross

by re

The p

calcu side

incre

the ,

1gp]

resu

Although the rate for elastically scattered events gets larger for the larger B characteristic of heavy nuclei, it never gets above 30% for protons and 36% for pions. The ratio of good PN π + to the total good Teuta fits is always one-third. This is what one would expect by chance fitting of events among the three fit types PN π +, π +NP, and PP π 0. Also the actual good PN π + fits must all be reduced by 4% which is the ambiant loss level of Monte Carlo events having no induced spark chamber error. Because of the reasons above and because the elastic scattering is approximately one-third²⁸ of the total cross section for proton and pions on larger nuclei such as aluminum and carbon, it will be assumed that all elastic scatters are lost.

One must now obtain the total cross sections for P nucleus or $\pi+$ nucleus scattering where $\sigma_T=\sigma_{el}+\sigma_{inel}$. Table 6.7 summarizes the data used to obtain the fits of cross section to energy. The cross section reviews given by reference 28 and 29 and data from reference 30 are used. The probability for a strong interaction can then be calculated on an event by event basis. The matter considered is summarized previously in Table 6.3 and 6.4. σ_{tot} increases as A and one can infer from the data above the total P-nitrogen and π -nitrogen cross sections. Table 6.8 summarizes the strong interaction correction results.

Table

Reac.

P+C

P+Al

Tabl

Table 6.7.--Elastic and Total Cross Sections for Protons and Pions on Carbon and Aluminum.

Reac.	E Gev	$\sigma_{f T}^{}$ mb	σel mb	Reac.	E Gev	$\sigma_{\mathbf{T}}^{}$ mb	σel mb
P+C	1 2.2 3.0 10. 20.6	370 <u>+</u> 9 367 <u>+</u> 8 390 344 355 <u>+</u> 7	112+15 107 <u>+</u> 6 100	π+C	.442 1.0 1.2 2.86	366+33 316 351+36 280+12	
P+A1	2.2 10.0 18.4	717	236 <u>+</u> 17 214 215 <u>+</u> 11	π +Al	.442 1.0 2.86	782 <u>+4</u> 6 650 588 <u>+</u> 22	379 <u>+</u> 37 178

Table 6.8.--Strong Interaction Correction Factors.

Track	Strong Interaction Loss
Proton	.0377
Pion	.0322

secti

will

Pigu

cons

Cham Numb

Figu

fir

or :

fir

CHAPTER VII

SPARK CHAMBER EFFICIENCY AND DE/DX LOSSES

7.1 Spark Chamber Efficiency

The efficiency will be calculated for the three sections of the apparatus separately and a total efficiency will be derived from these three sub-efficiencies.

Figure 7.1 shows the beam, magnet, and hodoscope sections consisting of 4, 4, and 2 chambers respectively.

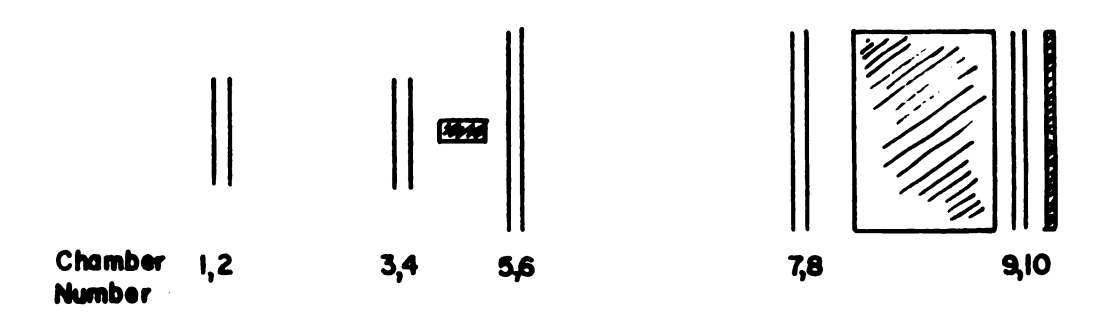


Figure 7.1. Spark chamber classification.

The filter program Crunch demands 3 or 4 chamber firings per track for the beam and magnet sections and 1 or 2 chamber firings per track out of the possible 2 firings after the magnet. Appendix G details the spark

chan

rest

syst

Tab.

ąC(

Pa:

an

Pa Co

S

.

þ

chamber efficiency calculation. Table 7.1 gives the results of the calculations for each section and the total system.

Table 7.1. -- Spark Chamber Efficiency.

Chamber Section	Efficiency	
Beam	.995	
Magnet	.932	
Hodoscope	.987	
Total	.915	

7.2 DE/DX Efficiency

The DE/DX efficiency calculation ³² takes into account the Landau energy fluctuation of energy loss by a particle through the scintillator, scintillator efficiency and photon production spectrum, the light pipe efficiency and the photo tube efficiency.

The Landau energy fluctuation curve for charged particles in matter is a statistical phenomenon because the collisions which result in the energy loss are independent of each other. The energy loss distribution is not symmetric but has a tail due to the infrequent collisions which result in large energy transfer. The half width at half maximum Δ_0 of the low side of the curve is given by 33 , 34

, who

is t

in t

prot

expe

^د - ٥

has

ligh of a

sci

ini

Pho

Dos

13,

3, 1 onl

Cat

tis

to

508

gCt g]:

In

-di

$$\Delta_{o} = 2Cm_{e}c^{2}xb/B^{2} \qquad (7-1)$$

, where C is Euler's constant, m_e is the electron mass, x is the material thickness in gm/cm^2 , and b and B are defined in the references cited above. For a 6 Gev/c momentum proton traversing 1/8" of the scintillator used in this experiment the most probable energy loss is 0.48797 Mev with $\Delta_{\rm C}$ = .0411 Mev.

The pilot F scintillator used in this experiment has a conversion efficiency of 2.72% for energy loss to light. The light emitted peaks at 4000 A° and has a FWHM of about 200 A°. This light will propagate through the scintillator and light pipe resulting with 4% of the initial light arriving on the first photocathode of the photo-multiplier. On the average this means that of the most probable 489.7 Kev of energy lost in the scintillator, 13.3 Kev are made into photons with an energy centered at 3.1 eV. With a light pipe-photo tube efficiency of 4%, only 182 of the initial 4538 photons arrive at the photocathode. The dispersion in this case due to photon statistics is 0.169 Mev. 35 When one compares the width due to photon statistics with the 0.084 Mev width due to energy loss fluctuations in the scintillator, it is clear that the actual experimental width of the single track events is due almost entirely to the photo tube-light pipe efficiency. In practice one knows the experimental width and the Landau width and derives the photo tube-light pipe

eff

in

tra

Tab]

Aver

Prob

Land

Scin Pi

Phot Ef

App1

Number 1

disc

The and

to c

the

COMP

the o

calcu

efficiency to be consistant with these numbers. Summarized in Table 7.2 are various specifications for a 6 Gev/c proton track.

Table 7.2--DE/DX Counter Characteristics for 6 Gev/c Proton.

Hardware Da	ıta	Physics Quantities		
Average Wavelength	4225. A°	Photon Energy	2.95 eV	
Conversion Efficiency	0.0272	Number of Photons	4538.	
Probable Energy Loss	0.4897 Mev	Landau Dispersion	0.0841	
Landau Width	0.0411 Mev	Photons at Cathode	182.	
Scintillator-Light	0.04	Photoelectrons	38.	
Pipe Efficiency	0.04	Photo Tube Dispersion	0.1694	
Photo Tube Quantum Efficiency	0.21	Total Dispersion	0.1891	
Applification Factor	0.49x10 ⁶			
Number of Stages	10			

Figure 7.2 compares the differential experimental discriminator curve, given by Table 7.3, to the calculation. The experimental curve has a width of 1.6±0.1 disc units and is centered at 2.95 disc units giving a ratio of width to center of 0.542±0.035. The width to center ratio for the calculated curve is 0.48. The width discrepancy is comparable to the error and does not significantly effect the overlap of singles to doubles.

Using the efficiency determined above, one can calculate the pulse shape expected for a 4.5 Gev/c momentum

Figure 7.2. The triangles mark differential discriminator curve points. These points are obtained by taking differences between successive values of the experimentally measured fraction of beam tracks given in Table 7.3. The solid curve is calculated as described in this chapter.

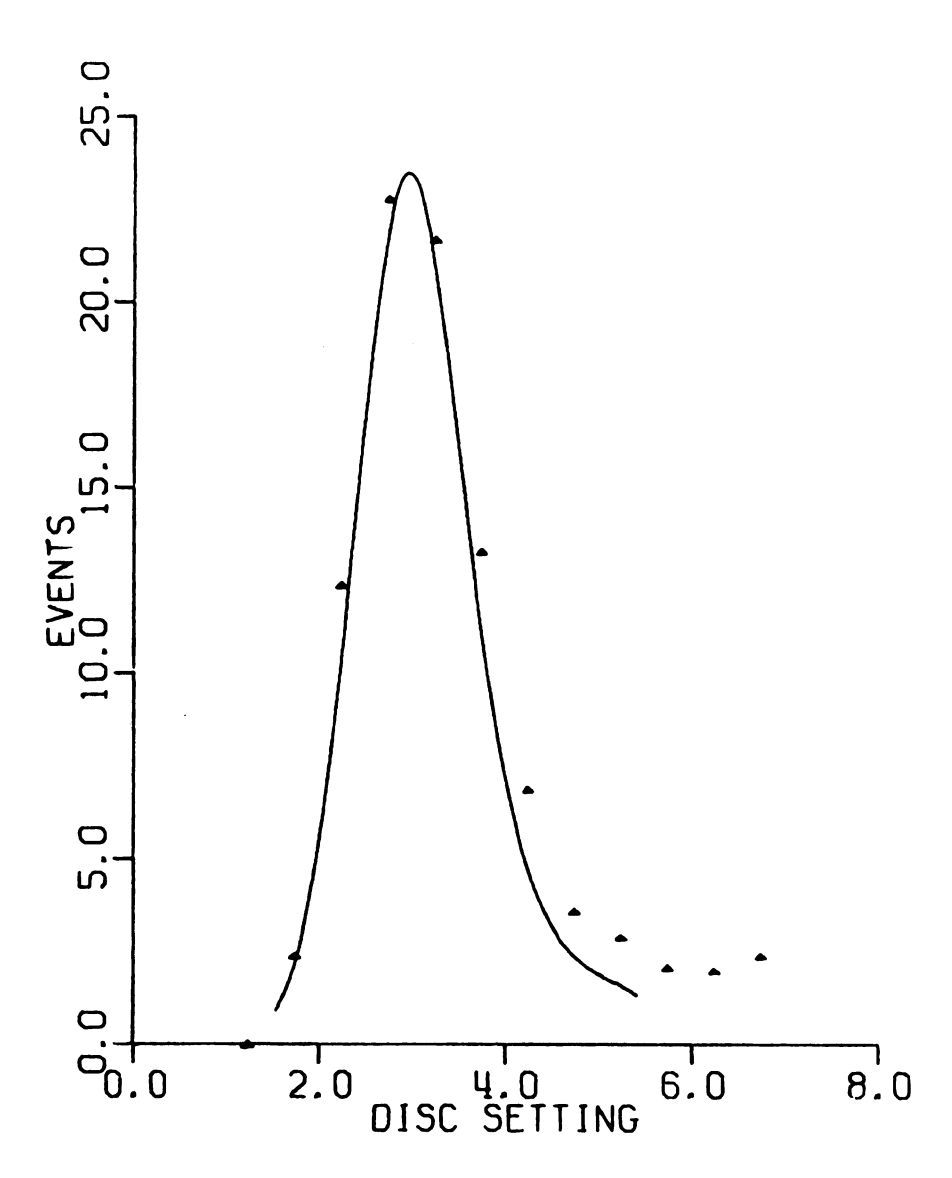


Table 7.3.--Experimental Discriminator Curve.

Disc Setting	Fraction of Beam Tracks	Disc Setting	Differential
1	99.8	1.25	0.1
1.5	99.7	1.75	2.5
2.	97.2	2.25	12.5
2.5	84.7	2.75	22.9
3.	61.8	3.25	21.8
3.5	40	3.75	13.4
4.	26.6	4.25	7.0
4.5	19.6	4.75	3.7
5.	15.9	5.25	3.0
5.5	12.9	5.75	2.2
6.	10.7	6.25	2.1
6.5	8.6	6.75	2.5
7.	6.1		

pro

in

Tab

Tab.

Ave

H

Con

Land

Scir Pi Phot

Arp:

Numi

alc

the

cou tha proton and a 1.5 Gev/c momentum pion as are typically seen in the experiment. This calculation yields the results in Table 7.4.

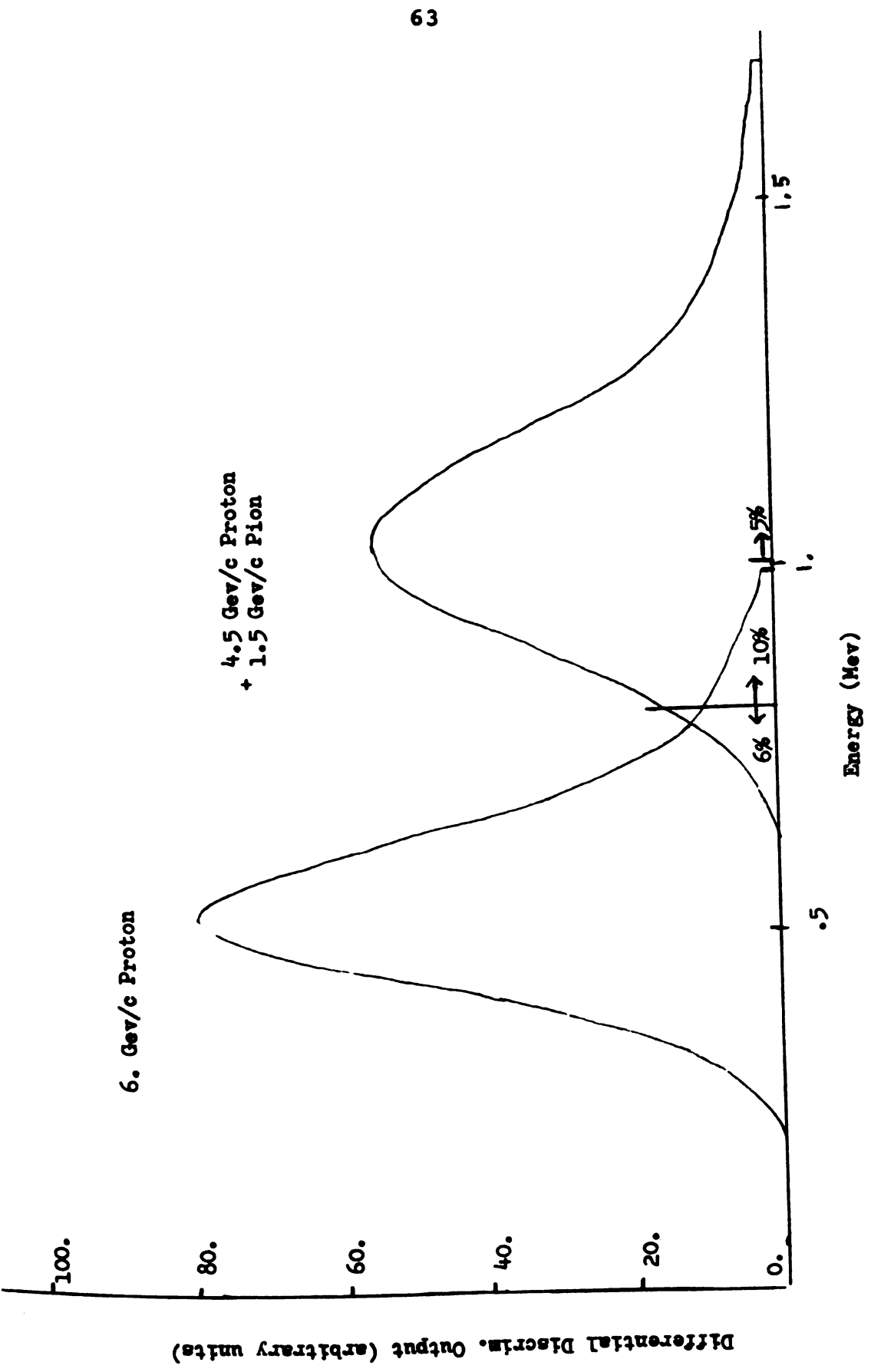
Table 7.4.--DE/DX Counter Characteristics for Real Event Triggers.

Hardware	Physics		Quantities
Average Wavelength	4225. A°	Photon Energy	2.948 eV
Conversion Efficiency	0.0272 Mev	Number of Photons	9116.
Probable Energy Loss	0.9836 Mev	Landau Dispersion	0.0593
Landau Length	0.0583 Mev	Protons at Cathode	365.
Scintillator-Light		Photoelectrons	77.
Pipe Efficiency	0.04	Photo Tube Dispersion	0.1192
Photo Tube Quantum Efficiency	0.21	Total Dispersion	0.133
Amplification Factor	0.49x10 ⁶		
Number of Stages	10		

Figure 7.3 shows the results of the calculation along with the singles energy spectrum. Real events had the discriminator set so that 10% of the singles are counted. Integration under the doubles curve indicates that 6% of the real events are lost at this setting.

Single and double energy loss curves and percent trigger loss due to discriminator setting. Figure 7.3.





noti

shif

and (

fider

facto

dist

٤++ و

Were

error

strai funct

fits

infor

crite

CHAPTER VIII

RESOLUTION AND AMBIGUITIES

8.1 Missing Mass

Early in the experimental data analysis it was noticed that the confidence level for Teuta fit events was shifted to be too high around 1 indicating χ^2 was too small and the errors were too large. It was found that the confidence level was flat after multiplying χ^2 by a factor of 7.2 which indicates that the errors are too large by a factor of 2.68. Figure 8.1a-d shows the confidence level distributions of all events together, the PNT+, PPT°, and Δ^+ + events after multiplying χ^2 by 7.2. Since both fits were one constraint fits, it was possible to multiply the error matrix as a whole by a common factor since one constraint fits have an error which can be written as a function of one variable only.

Figure 8.2a shows the 40471 neutron missing mass fits using the CIRCE geometric fit and the track fit information as provided by Teuta. A simple best selection criteria is made to determine the proper fit. Figure 8.2b

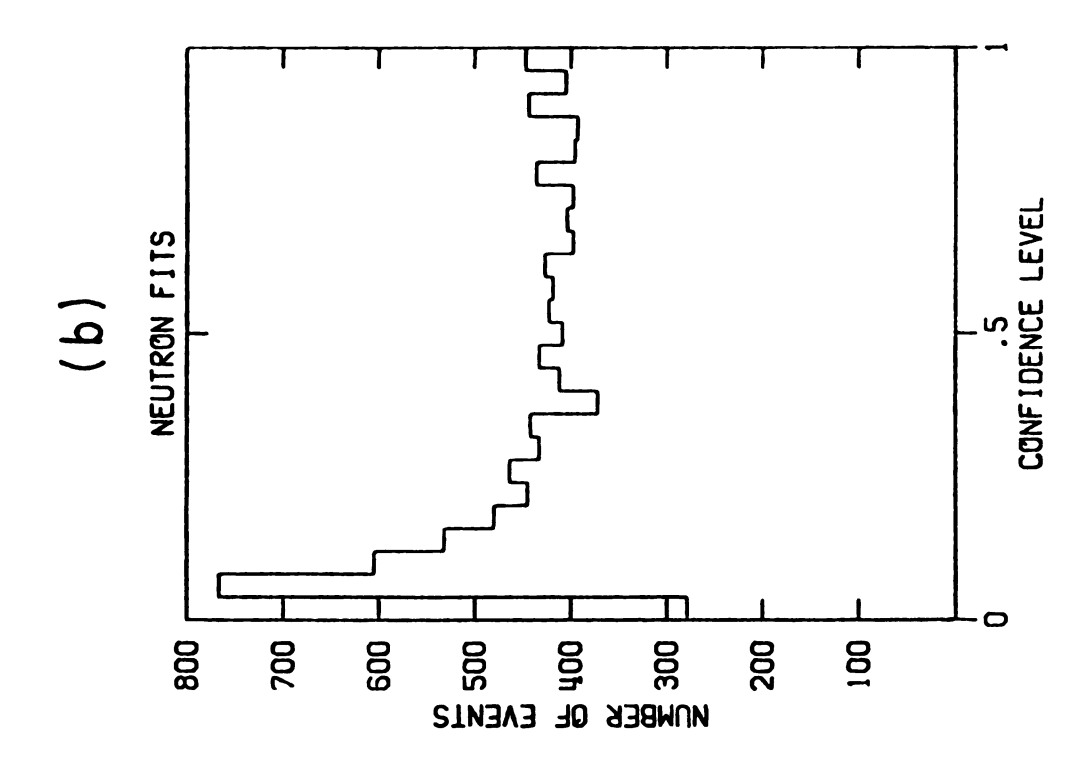
Confidence level distribution after the χ^2 is multiplied by 7.2. Events with a confidence level less than 3% are not plotted. Figure 8.la-d.

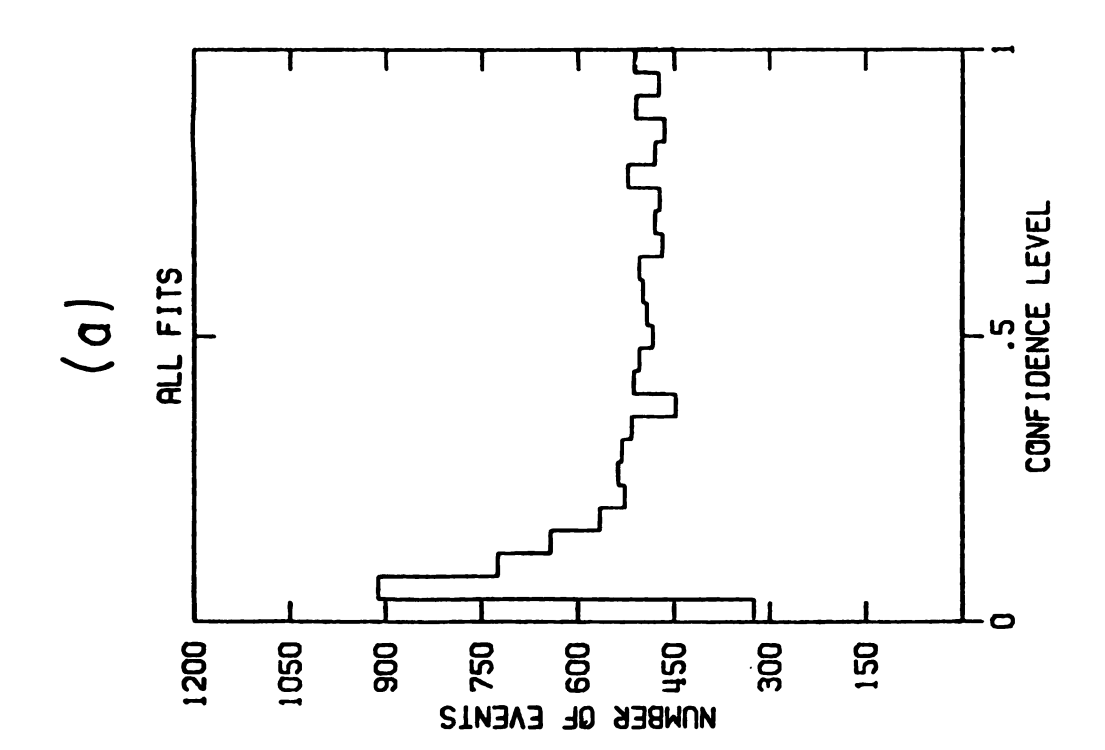
a. All events.

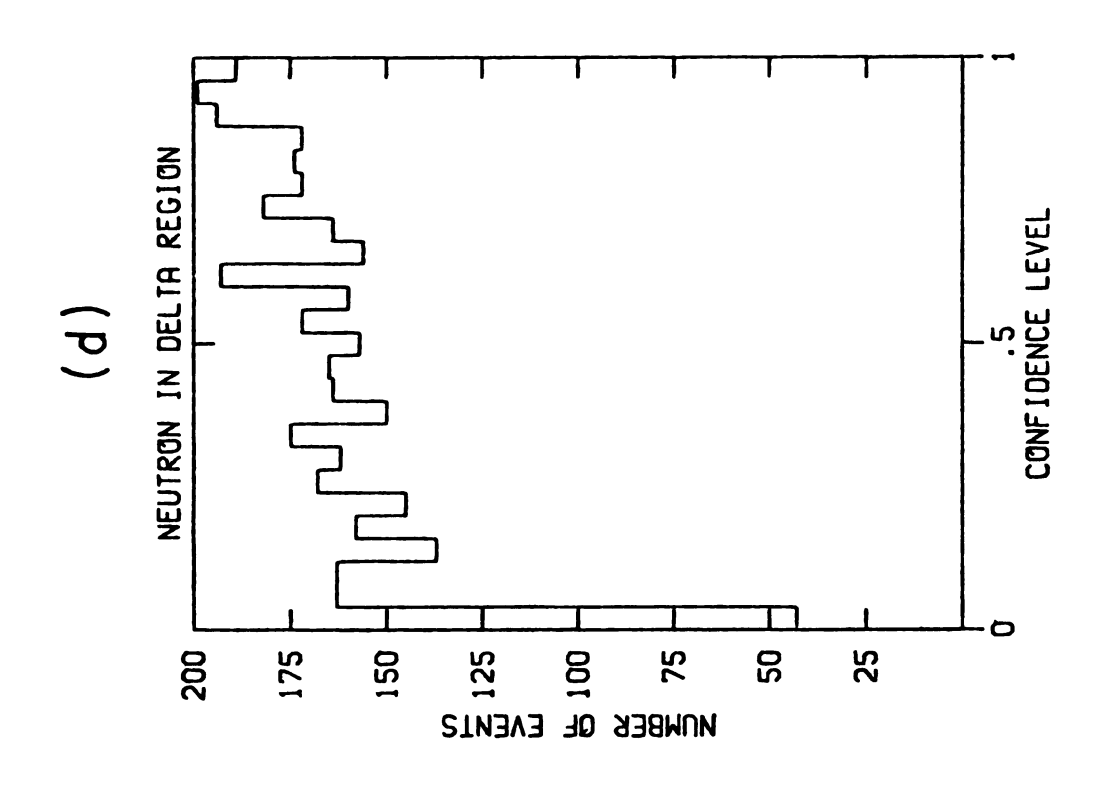
b. PNn+ events.

c. PPm events.

d. Events in ∆++ region.







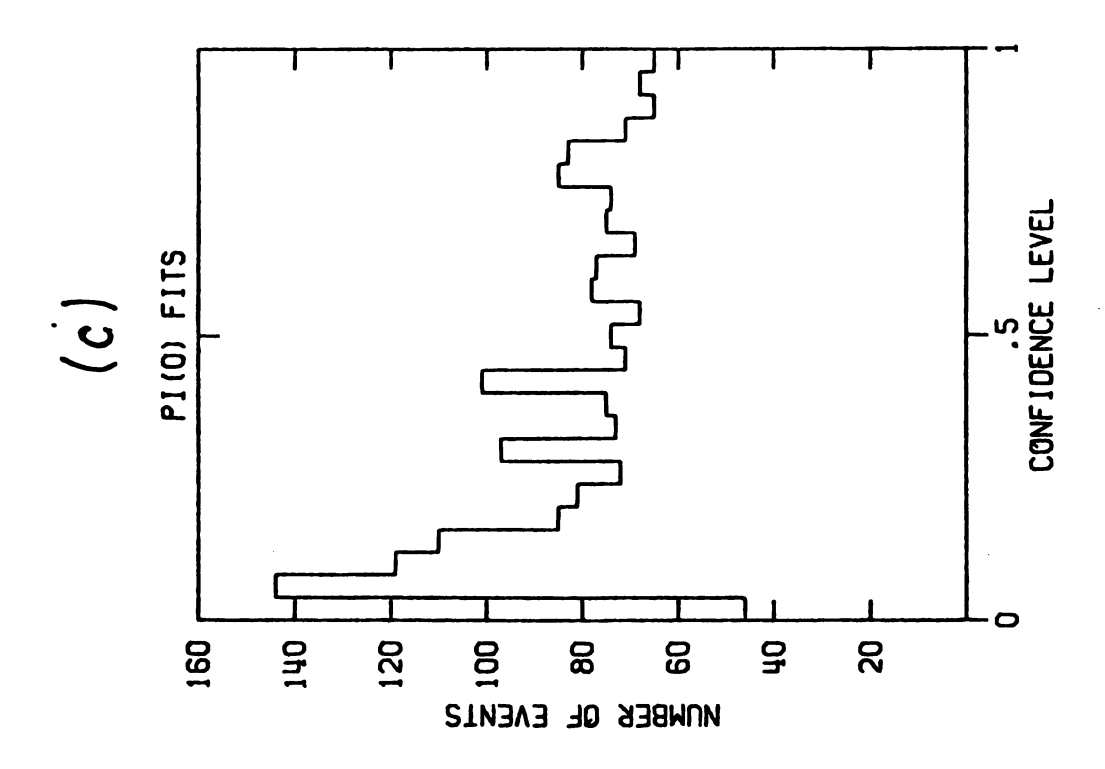
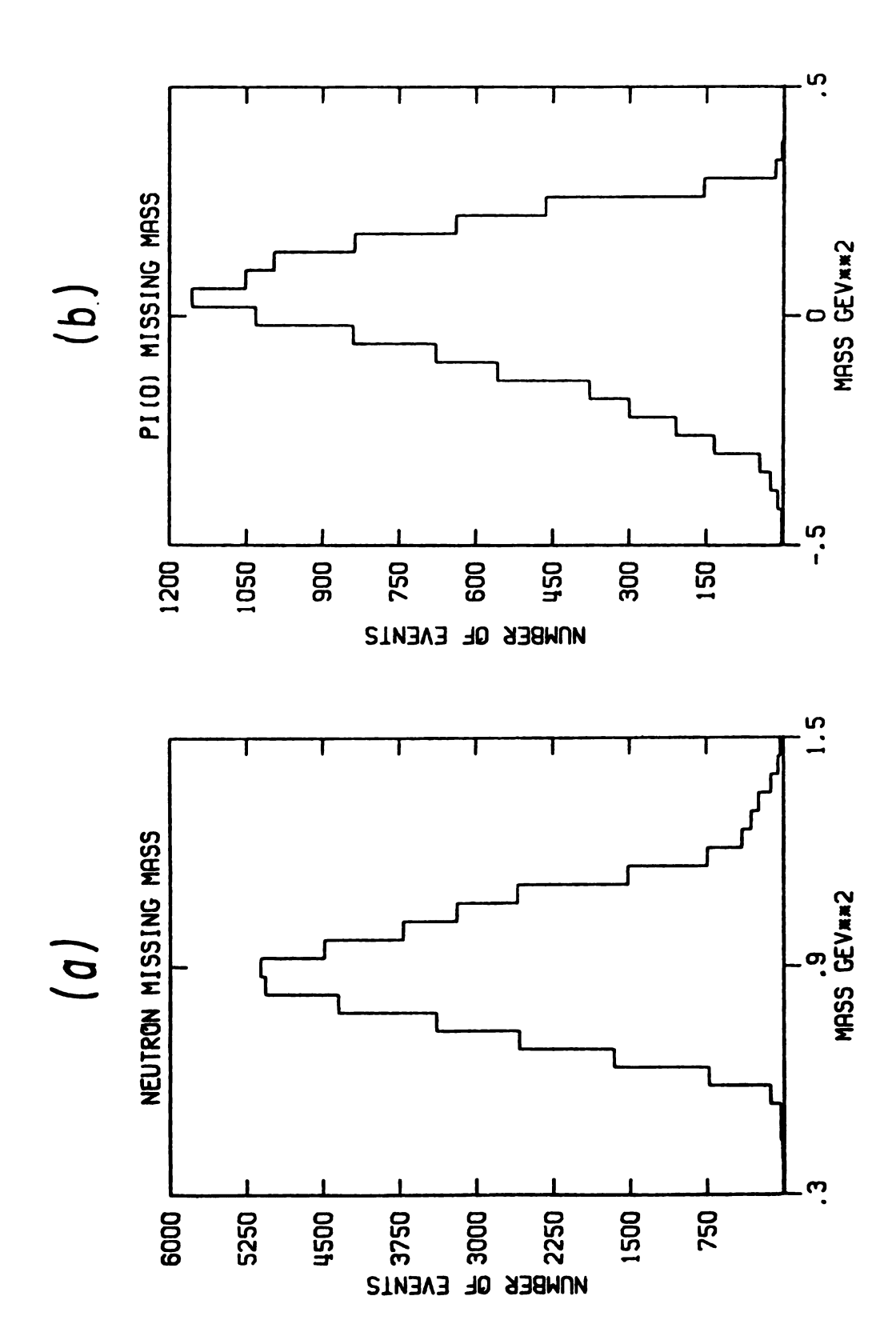


Figure 8.2. Missing mass squared distributions after event reconstruction.

a. 40471 neutron missing mass fits.

b. 9525 neutral pion missing mass fits.



shows the 9525 neutral pion missing mass fits obtained in this experiment.

Figure 8.3a shows the error in missing mass squared distribution for all 4047l PN π + fits where the Circe error matrix is made to be consistant with a flat confidence level as in Figure 8.1a-d. This error is calculated as described in Appendix H. The pion-proton track ambiguity is resolved using the Teuta confidence level criteria. Figure 8.3b shows a Gaussian ideogram using these errors centered at $M_N^2 = 0.88 \text{ Gev}^2$. The Gaussian ideogram width of 187 Mev compares with the experimental neutron width of 197 Mev as will be shown later.

Figure 8.4a shows the best Gaussian fit of the form

$$\sigma(MM) = (Norm) \exp\left[-\left(\frac{M-M_0}{\Gamma}\right)^2\right]$$
 (8-1)

to the pion data with the mass constrained to be at the pion mass squared of $M\pi^2 = 0.019 \text{ Gev}^2$. The error bars are statistical errors only. Figure 8.4b shows the best Gaussian fit to the neutron data, shown by the error bars. The fit results are summarized in Table 8.1. The widths are the 1/e half widths.

8.2 Invariant Mass

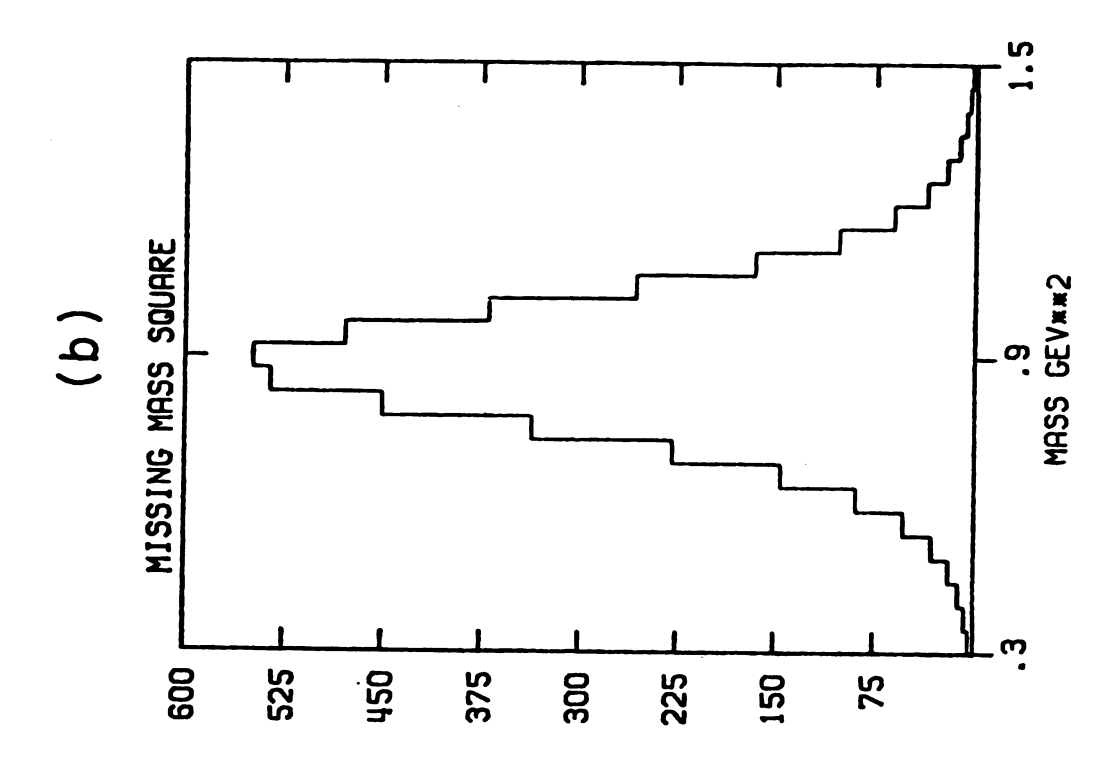
The Breit-Wagner form used throughout this section

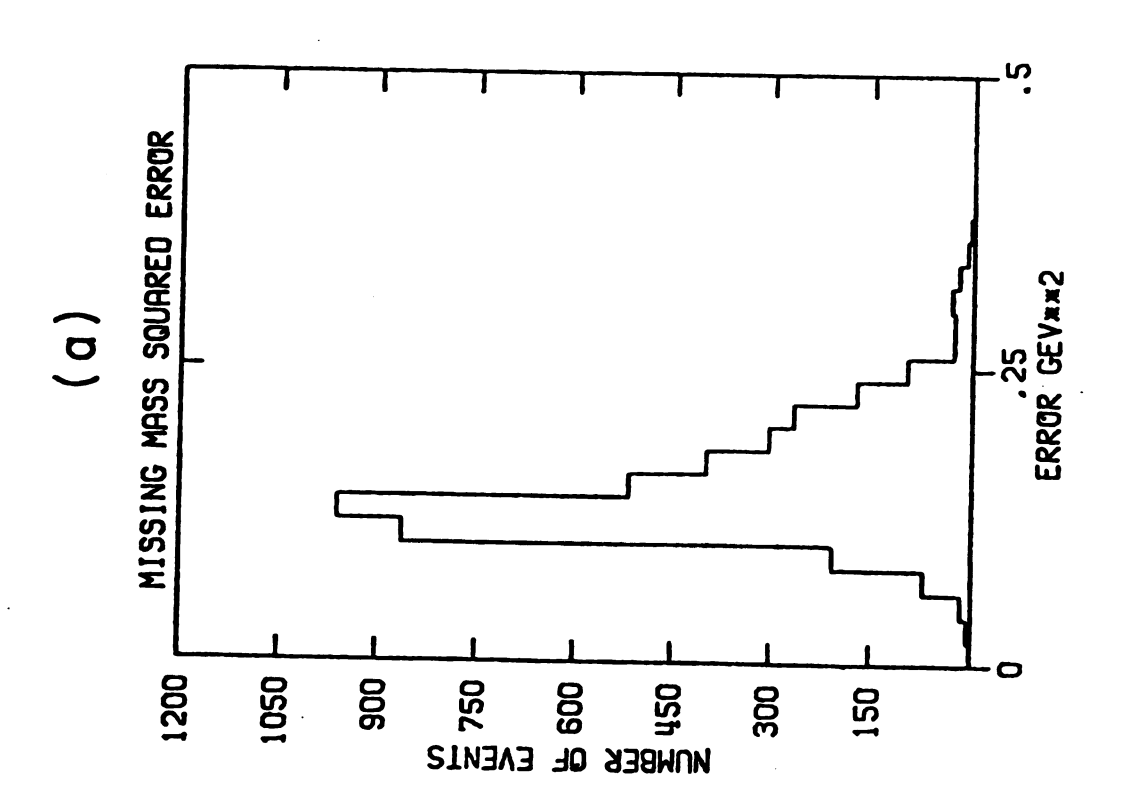
to analyse the experimental invariant mass distribution

is given by

Neutron error distribution consistant with flat confidence level. Gaussian ideogram around $M_N^2=0.88~{\rm Gev}^2$ using errors. ٠ ت Figure 8.3.

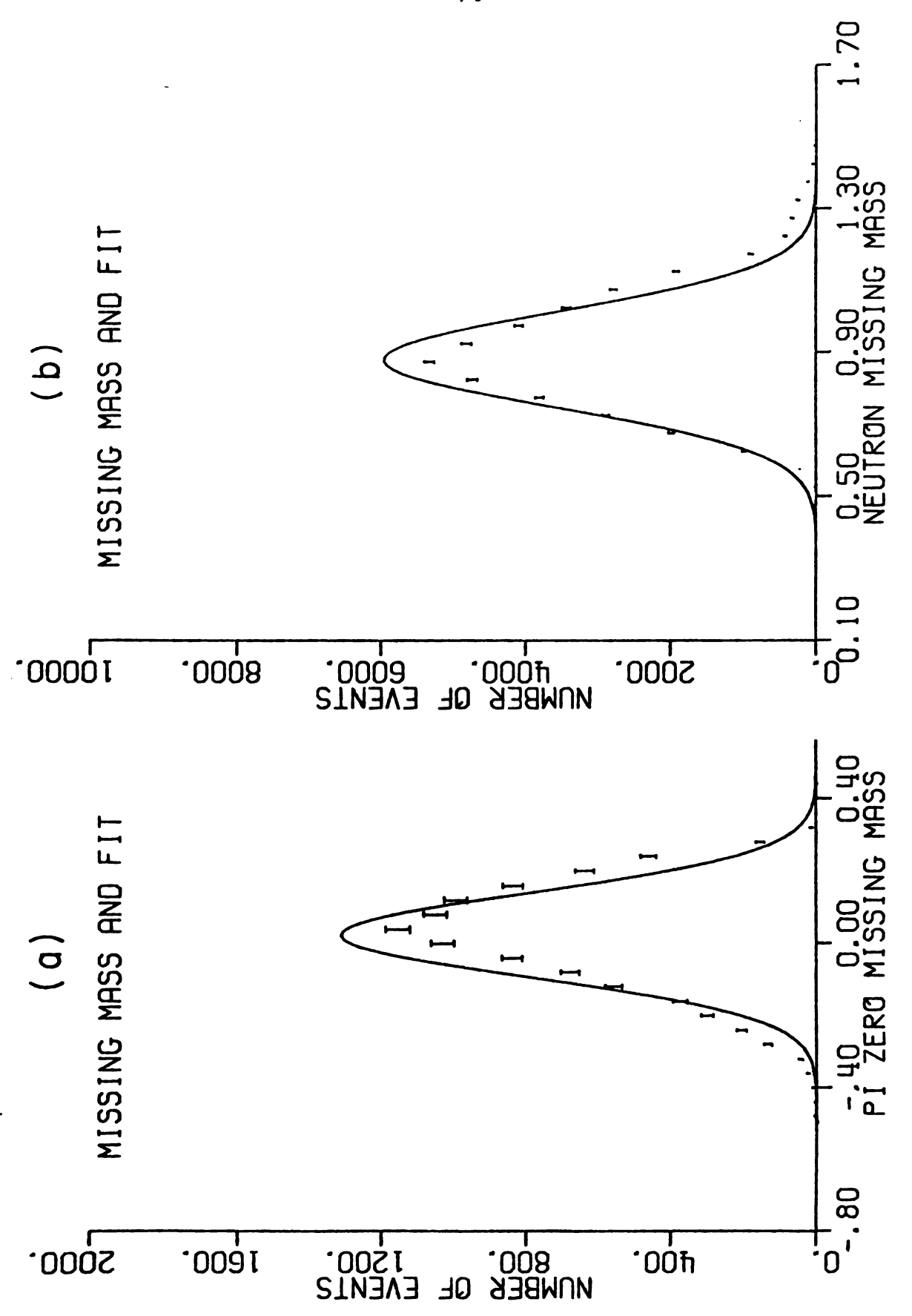
P





Pion missing mass data and Gaussian fit for $M^2\pi$ and $\Gamma\pi$. Neutron missing mass data and Gaussian fit for Γ_N with M 2 = 0.88. Figure 8.4.

Ď.



Fit Type	Variables	M Fit-Gev	Γ Fit-Mev
Neutron	м, Г	0.908	199.
Neutron	Γ	${\tt M}_{ m N}^2$	186.
Pion	м, Г	0.0227	164.
Pion	r	m ²	165.

Table 8.1.--Results of Gaussian Fit to Missing Mass Plots.

$$\sigma(M) = \frac{\Gamma}{(M^2 - M_0^2)^2 + \Gamma_M^2}$$
 (8-2)

where

$$\Gamma = \frac{M_0 \chi (QR)^3}{[1 + (QR)^2]}$$
 (8-3)

 M_O and γ are determined by fitting and R is the $\Delta + +$ radius take as 4.0 Gev⁻¹. Q is the momentum of the proton in the $\Delta + +$ center of mass given by $Q=R(M_p,M\pi,M)$, where M is the $\Delta + +$ mass, $M\pi$ is the pion mass, M_p is the proton mass and R is defined by equation (10-21). An estimate of the S1/2 wave background was determined using bubble chamber data in a wider mass range. The 3-body phase space is

$$R_{3} = \int \frac{d^{3}P_{1}d^{3}P_{2}d^{3}P_{3}}{2E_{1}2E_{2}2E_{3}} = \int \frac{d^{3}P_{3}}{2E_{3}}R_{2} = \int \frac{d^{3}P_{3}}{2E_{3}}\frac{TQ}{M} \quad (8-4)$$

where R_2 is the two body phase space term. This gives

$$\frac{dR_3}{dP_3} = \left(\frac{4\pi P_3^2}{2E_3}\right) \frac{\pi Q}{M} \qquad (8-5)$$

where P_3 is the $\Delta++$ momentum in the over-all center of mass and E_3 is the center of mass energy. P_3 is given by

 $P_3=R(M_N,M,E_3)$, where M_N is the neutron mass. The chain rule gives

$$\frac{dR_3}{dM} = \frac{dR_3}{dP_3} \frac{dP_3}{dM} . \qquad (8-6)$$

This leads to the Lorentz invariant phase space given by

$$\frac{dR_3}{dM} = \frac{2\pi^2}{E_3} QP_3 \qquad (8-7)$$

A fit of the form σ^T (M) = σ (M)+A (Phase Space) is made to the bubble chamber data for 1.14 M<1.66 GeV and t<.3 GeV². The errors are assumed to be given by statistics and a maximum likelyhood fit results in a X^2 /point of 1.08. The best fit parameters for the width γ , M_O and A are given in Table 8.2.

Table 8.2--Bubble Chamber Background Estimates Fit Parameters.

$$M_O = 1.245 \text{ GeV}$$
 $\gamma = 0.726 \text{ GeV}$
 $A = 1.115 \text{ mb}$

The S wave contamination is estimated for the mass range 1.14<M<1.42 Gev as the following:

Fractional Contribution =
$$\frac{\int A(\text{Phase Space}) dM}{\int \sigma^{T}(M) dM}$$
 (8-8)

This leads to a 4% non-delta background. The fit parameters M_O and γ are not sensitive to the addition of the phase space term. When the mass range is restricted to M<1.42 Gev, the entire phase space term is too small to give a meaningful fit. Figure 8.5 shows the bubble chamber data along with the phase space curve, the Breit-Wigner curve, and the sum of these. The data peak at 1.228 Gev has a F.W.H.M. of 0.111 Gev as mentioned earlier. The lower Breit-Wigner curve peaks at 1.228 Gev and has a F.W.H.M. of 0.128 Gev. A simple Breit-Wigner fit to the data without a phase space curve peaks at 1.226 Gev and its F.W.H.M. is 0.129 Gev. The conclusion from this analysis is that the S_{1/2} wave background has no appreciable effect on the peak, width, or shape of the mass data.

The error in invariant mass can be calculated similar to the missing mass. Appendix H contains the details of the transformation $\Delta M(p,\pi+) = T(K_i, \Delta k_i, \lambda_i, \Delta k_i, \Delta$

Figure 8.5. Breit-Wigner plus phase space fit to bubble chamber data.

- a. Phase space curve.
- b. Breit-Wigner curve.
- c. Sum of phase space and Breit-Wigner curve fit to date.

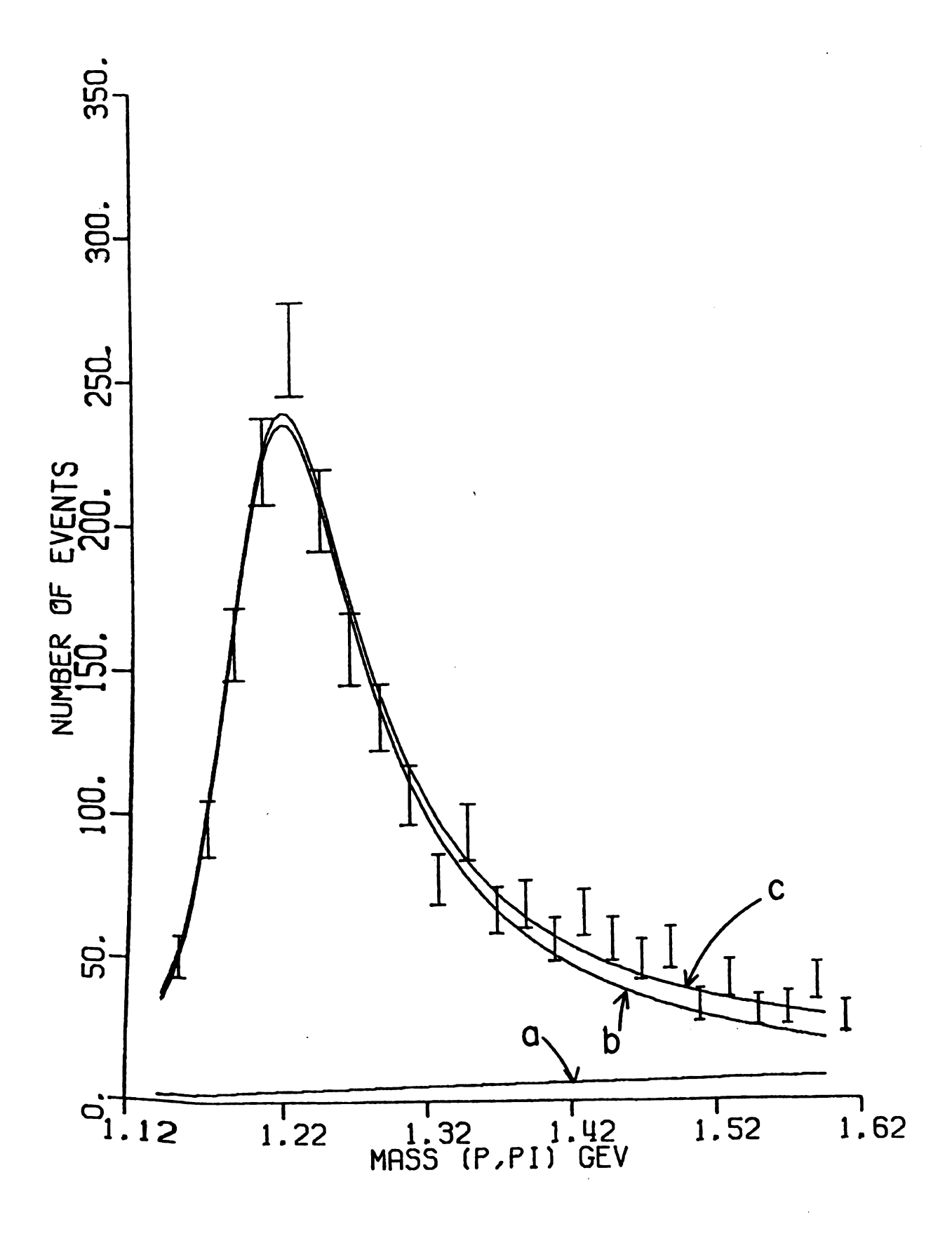
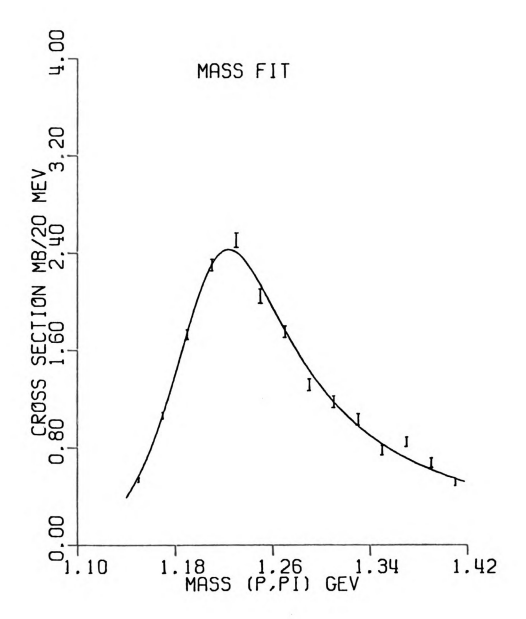


Figure 8.6. Breit-Wigner fit to experimental mass distributions.

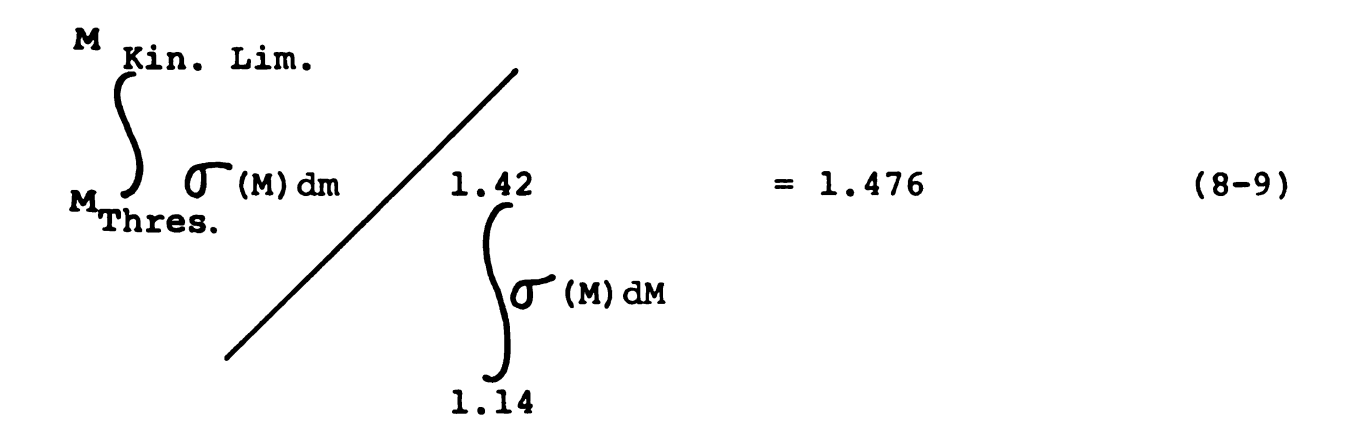


to the actual data. The uncorrected and corrected mass parameters are given in Table 8.3.

Table 8.3.--Mass Parameters for $\Delta++$ (1236) Resonance.

	F.W.H.MGev	Peak Position-Gev
Experimental	0.133 <u>+</u> 0.006	1.226 <u>+</u> 0.004 Gev
Corrected	0.126 ± 0.006	1.266 ± 0.004

For cross section purposes, one can get from the experimental fit



8.3 Momentum Transfer Squared Resolution

The momentum transfer squared resolution can be infered from the Teuta output errors. Appendix H outlines the method of obtaining the momentum transfer squared error from the Teuta output errors. Figure 8.7a-b shows a plot of the error in t versus t where t is the negative momentum transfer squared. Figure 8.7a has t bins proportional to the experimental t distribution. Figure 8.7b has the curve normalized so W(t,E) is constant, where W(t,E) is the probability of finding an error E at momentum transfer squared t. To a good approximation, one can say the error is 2% except at small t. This small error has an insignificant effect on the shape of the momentum transfer squared distribution.

8.4 Ambiguities

In order to simulate the experimental ambiguity problem, Monte Carlo events were generated as discribed in Appendix E and are given a Gaussian error spread about their central tracked values equal to the original input Circe production errors. This choice for the error parameter produces a χ^2 distribution for Monte Carlo events out of Circe equal to the experimental event χ^2 distribution centered at 0.6. If no error is applied, this Monte Carlo χ^2 distribution is centered at 0.1.

Probability of finding an error E at momentum transfer squared t. a. Figure 8.7.

Probability of finding an error E at momentum transfer squared t normalized so that **.**

 $\int W(t,E) dE = CONSTANT.$

The circe output events with the induced error were processed by Teuta and the fit confidence levels were examined. All input events were known to be Mark 4.

Because of the ambiguity resulting from simulated errors in the spark position in the chambers, not all Teuta fits are Mark 4 when a best confidence level selection rule is applied. The Monte Carlo analysis yields 5424 Teuta events with confidence level greater than 10⁻⁵, 4968 events with confidence level greater than 3% and 4296 events pass a standard deviation cut for Circe reconstruction of 0.6. The drop from 5424 Teuta events to 4968 events after a 3% confidence level cut represents an 8% lost. This is believed to be due to the Monte Carlo accuracy and will not be used to support the notion that an 8% confidence level correction is to be applied.

Out of the 4296 original PN π + events, there were 1977 Δ ++ events if all were interpreted as Mark 4 fits. If a best confidence level selection rule is applied, as was done with the experimental data, only 1233 Δ ++ events are obtained. This loss of Δ ++ events is due to miscalling the Mark 4 fits as Mark 104 and Mark 2 fits. These results are summarized in Table 8.4.

The 1233 $\Delta++$ events from the 4 + 104 category come from interpreting Mark 4 fits as 4 and Mark 104 fits as 104. The 470 $\Delta++$ events under the 104 category are how many of the original 1977 $\Delta++$ events with the correct 4 interpretation are in the 104 category. The 25% ambiguity

Table 8.4--4296 Mark 4-Teuta Fit Breakdown.

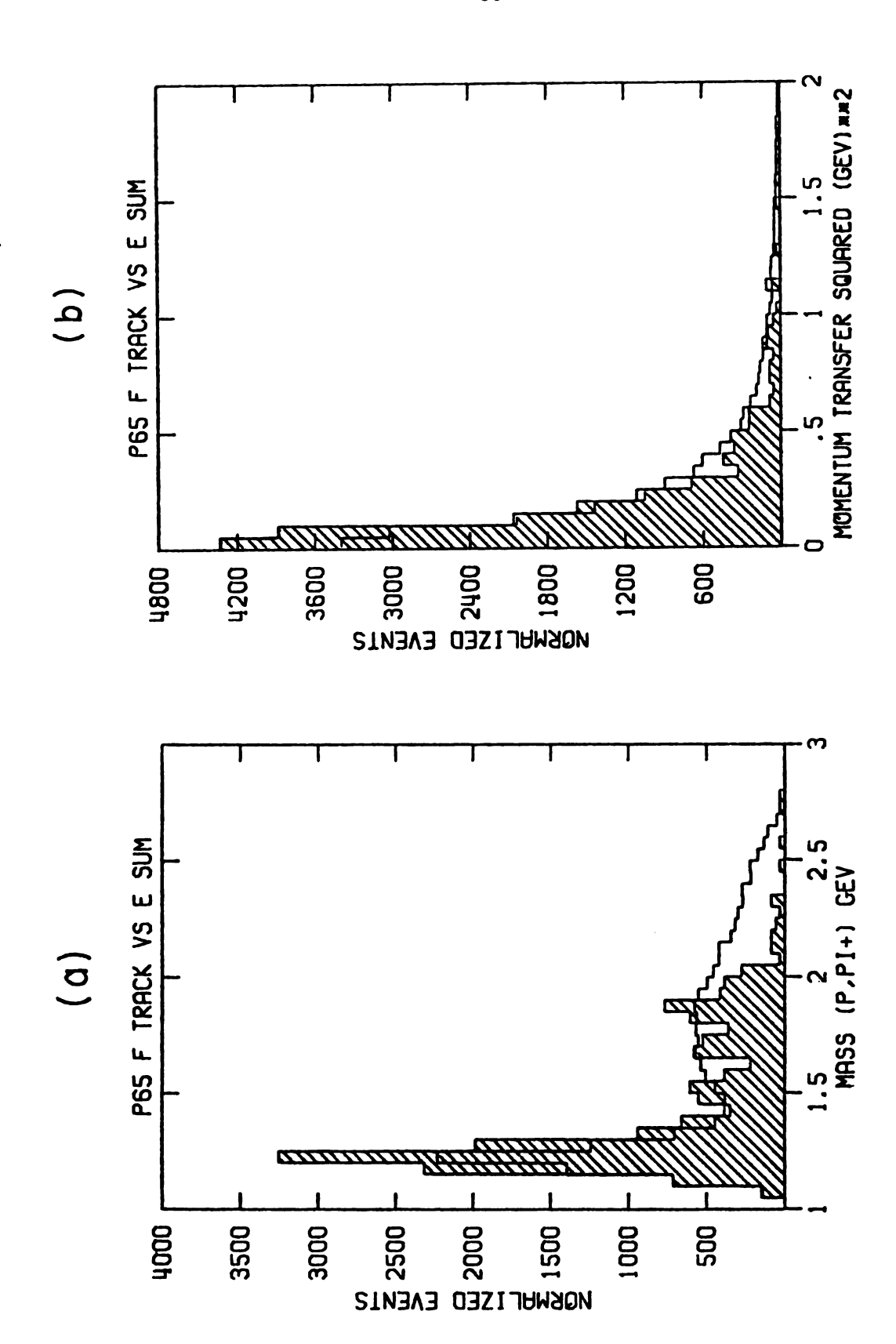
Mark Number	PNπ+	Δ++
4	2485	1107
4 + 104	3 552	1233
2	744	400
104	1067	470

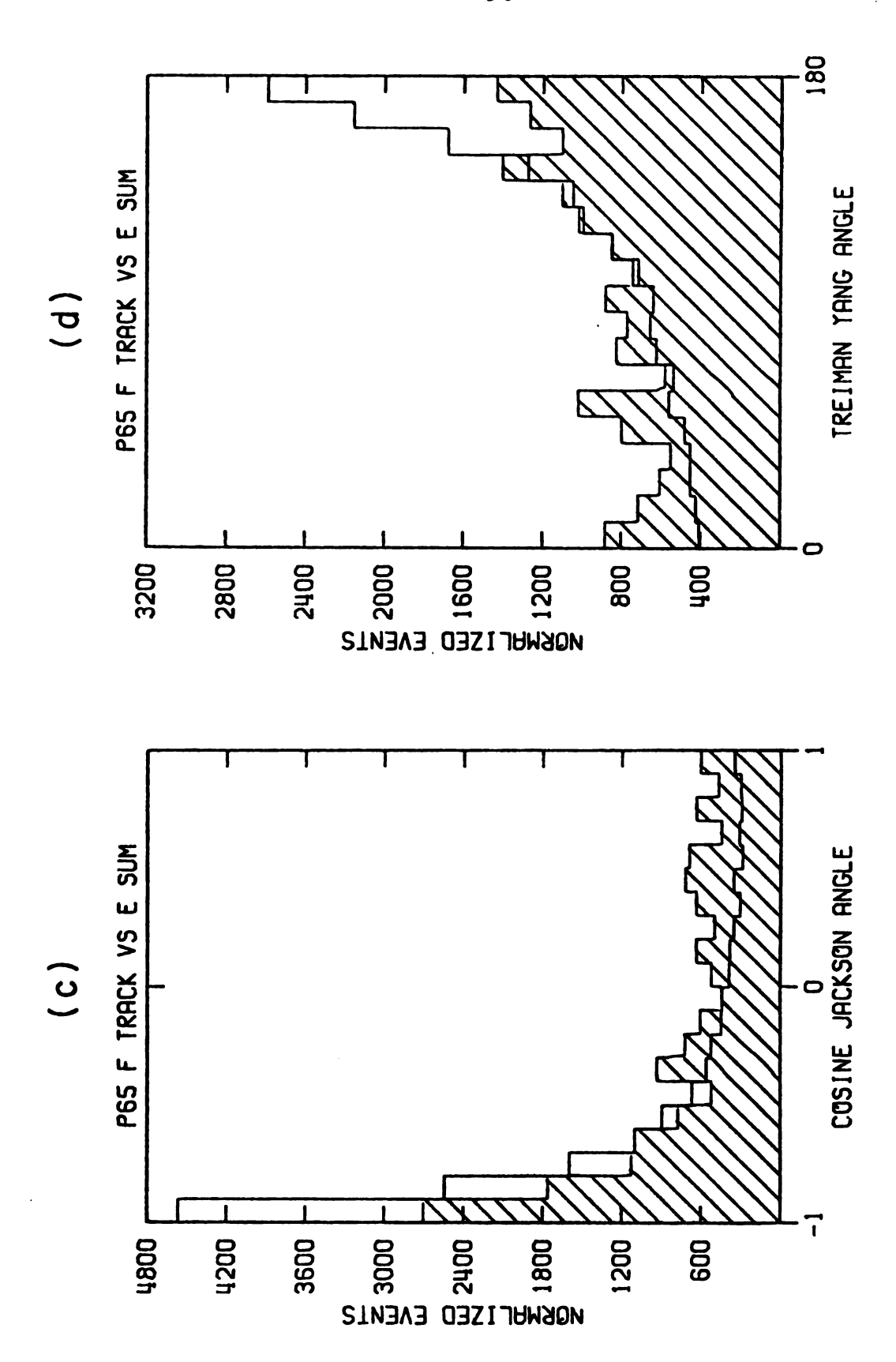
level of this experiment will have an effect on both the cross section and distributions of physical quantities.

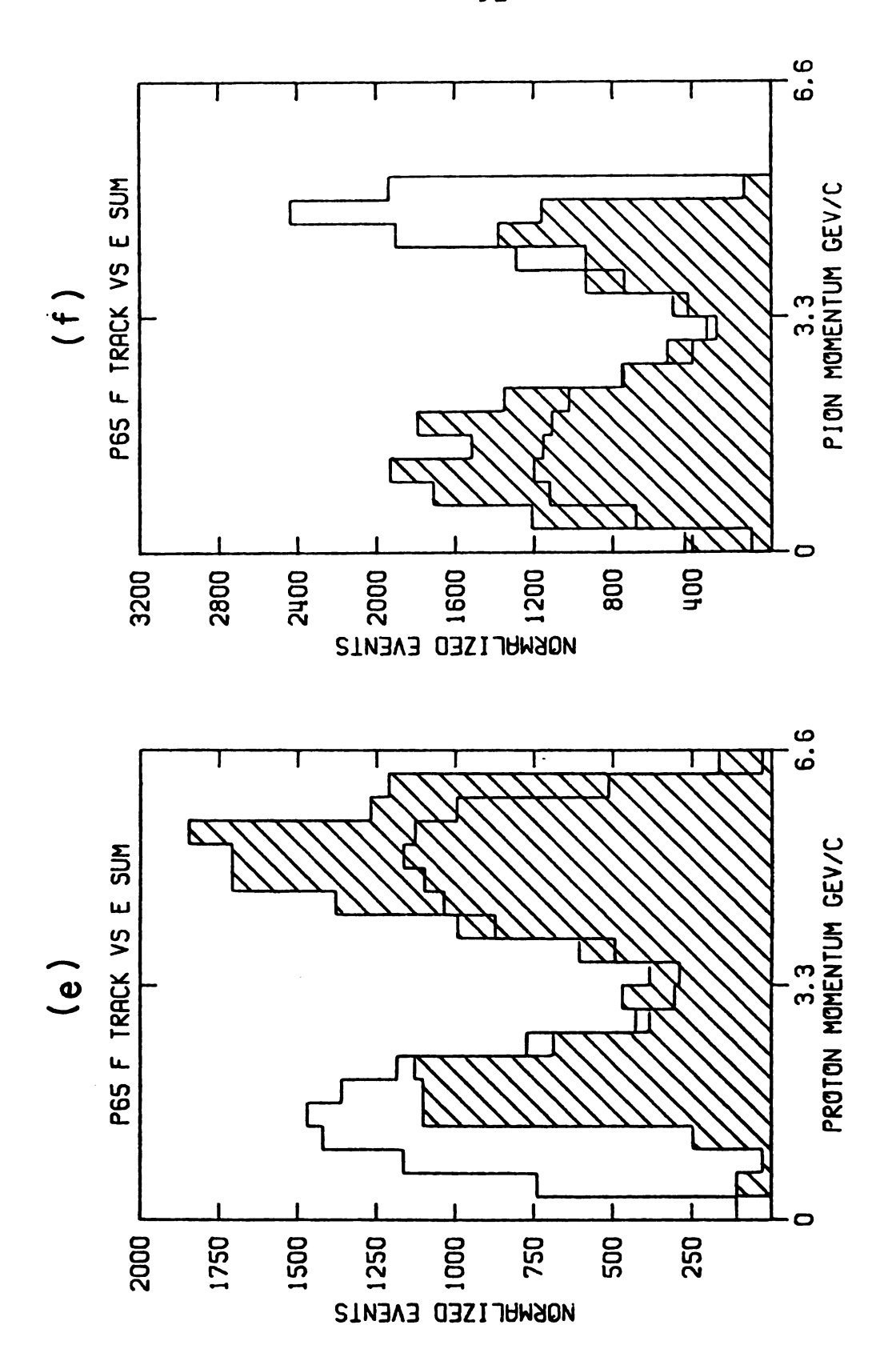
The dominate process which can change distribution shapes is the ambiguity between Mark number 4 and 104. The shape changes occurring from ambiguities between Mark 4 plus 104 and Mark 2 events were studied and found to be minimal. The total ambiguity related shape changes on the Pole extrapolation results were shown to be less than the statistical error in the data. The effect of event ambiguity on the Mp π +, t, $\theta_{\rm Jac}$, $\phi_{\rm TY}$, proton momentum and Pion momentum distributions is shown in Figure 8.8a-f. Figure 8.8a shows the spark chamber data mass distribution unshaded and the simulated ambigious Monte Carlo distribution shaded. Both distributions have a smaller Δ ++ peak and have more events at high mass as compared to the bubble chamber data shown in Figure E.1-a.

The $\Delta + +$ peak was shown to be entirely due to fast Protons and slow pions in the forward hemisphere. The

Spark chamber data (unshaded) and Monte Carlo events with induced errors selected by best confidence level (shaded). Figures 8.8a-f show the Mpπ+, t, θ_{Jac} , ϕ_{TY} , proton momentum and pion momentum distributions respectively. Figure 8.8.







unmodified Monte Carlo and bubble chamber data predict a two to one dominance of fast protons to slow protons for the entire $PN\pi+$ sample. The pions are predicted to have the opposite momentum distributions. The actual momentum distributions from the ambigious data, shown unshaded in Figure 8.8e-f, show a dominance of slow protons and fast pions. The effect of the ambiguity is to swap protons and pions. Since originally most protons were fast, they turn into fast pions after being miscalled. When a mass plot is made, these one time fast proton-low mass events are now fast pion-high mass events. If a low mass $\Delta++$ cut is made, these events are eliminated from the sample. As mentioned earlier, this swapping of protons and pions has almost no effect on shapes of interest in the $\Delta++$ region, but has a large effect on the over-all cross section.

The shape correction will be defined as

Correction Factor = $\frac{\text{Original Weighted } \Delta + + \text{ Events}}{\text{Experimentally Determined Weighted}}$ $\Delta + + \text{ Events}$

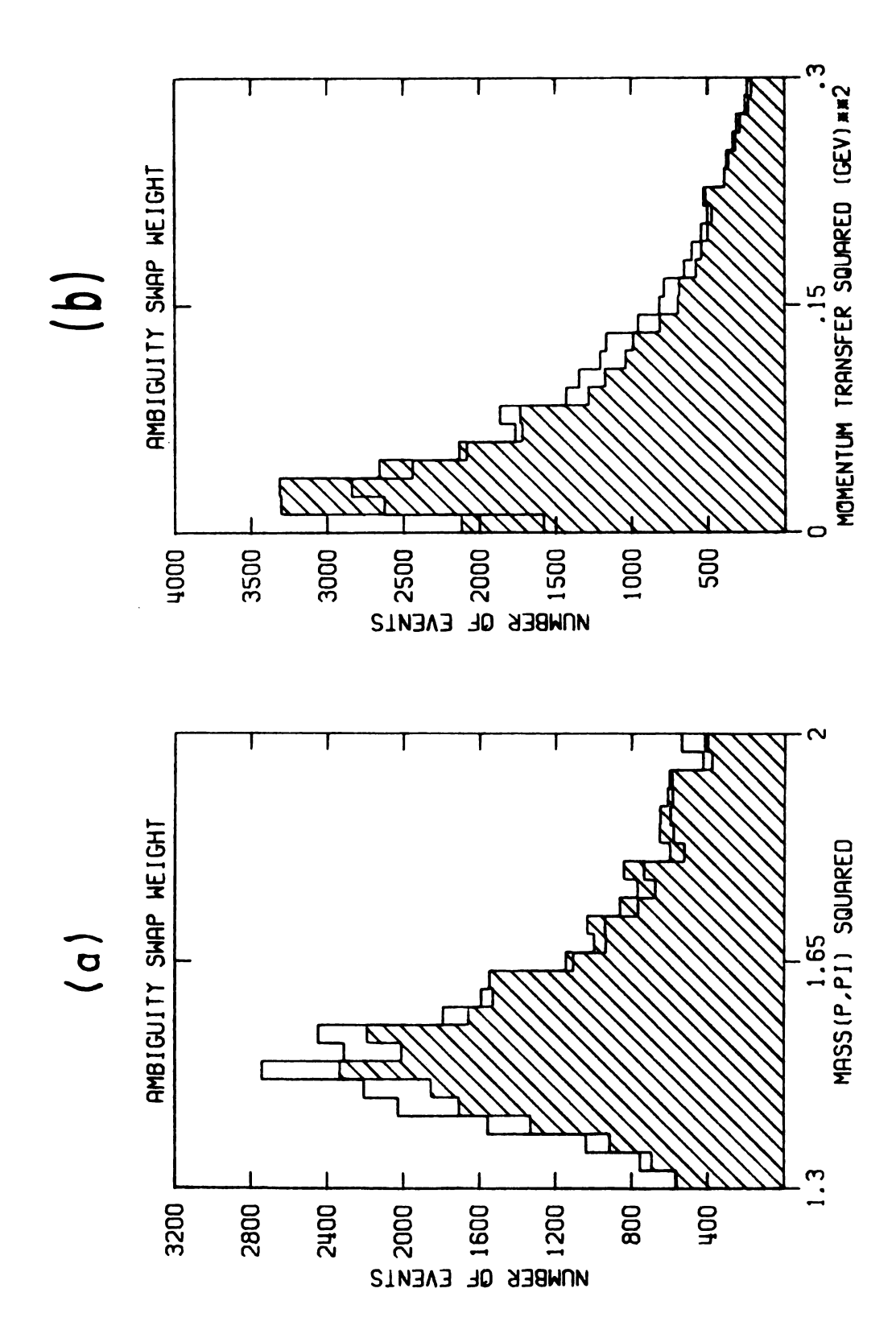
All original 1977 $\Delta++$ events, plus the 104 new $\Delta++$ events from the Mark 4+Mark 104 swapping, were weighted for acceptance to make sure that if the swapping has any strong kinematic dependence, these could be incorporated into the final correction factor. No strong dependence was found. The average weight factor for the 2081 events is found to be 2.38 giving 4748.9 weighted events. If a $\Delta++$ cut is

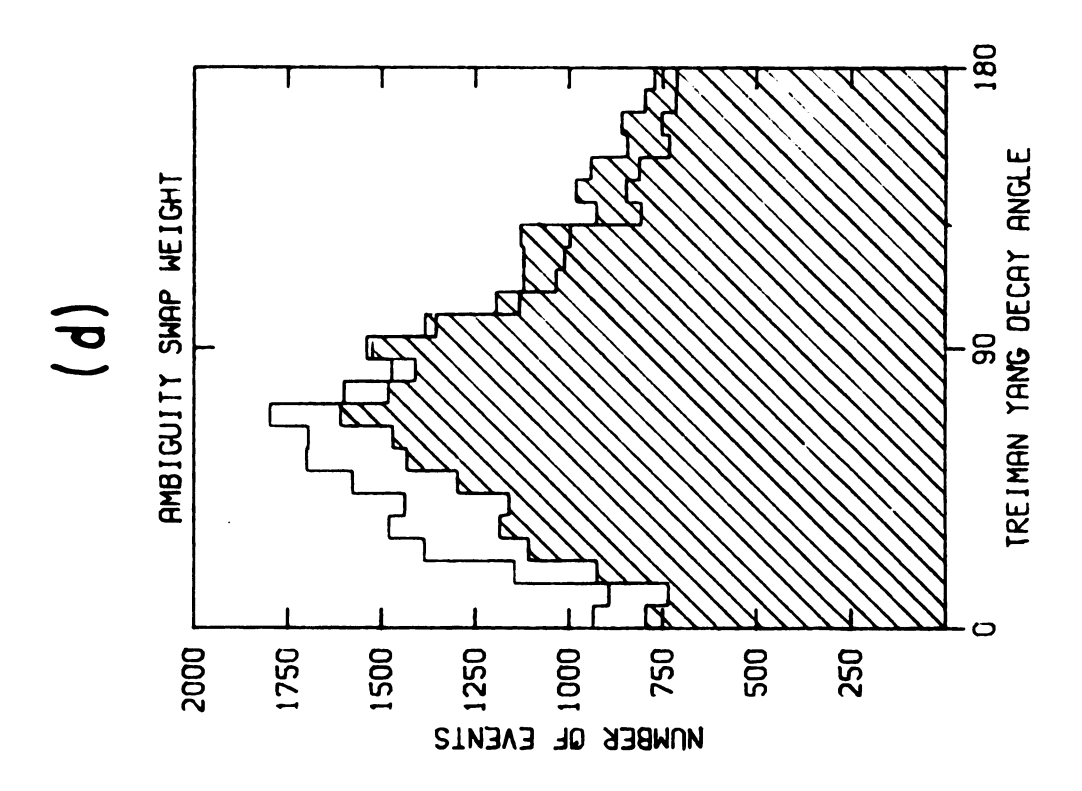
applied using the Teuta confidence level criteria one gets 2924.8 $\Delta + +$ events. The mass, t, and $\theta_{\rm Jac}$ and $\phi_{\rm TY}$ plots are divided into 10 bins and the ratio of original $\Delta + +$ to be fitted $\Delta + +$ is calculated for the 10 bins. The errors are assumed to be statistical only and a four-parameter fit is made to the ratios. Figure 8.9a-d shows the uncorrected and corrected mass, t, $\theta_{\rm Jac}$ and $\phi_{\rm TY}$ distributions normalized to have equal areas.

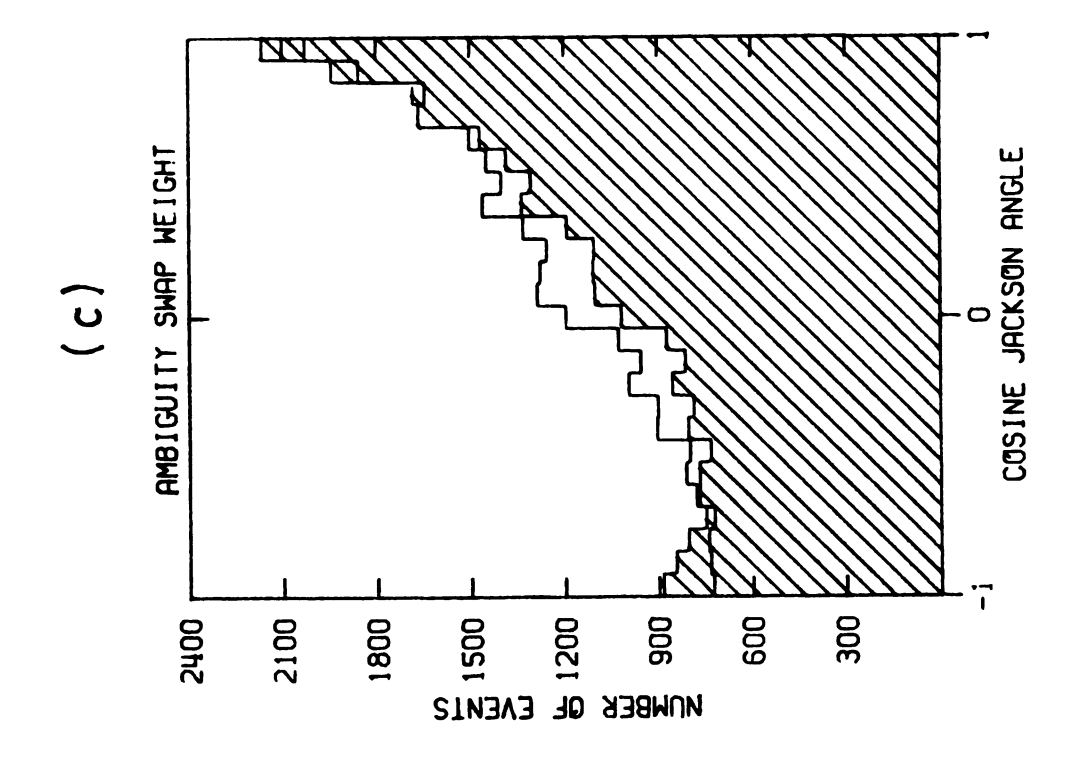
The correction factor for the cross section is the ratio of actual $\Delta ++$ in the Monte Carlo sample divided by the number of $\Delta ++$ as determined by the experimental data analysis. The Monte Carlo events are known to have 1977 $\Delta ++$ in the initial sample of PN $\pi +$ because the correct name of all these tracks is known from the generation process. The events are made to simulate the actual spark chamber events and are processed in the same manner, and one ends up with only 1233 $\Delta ++$ events. The correction factor is then 1977/1233.

The correction factor above considers only event losses resulting from Mark 4 events being misinterpreted as Mark 104 or Mark 2 events. Monte Carlo studies were made using Mark 104 and Mark 2 events and the fractional event misinterpretation due to the ambiguity was shown to be symmetric for all fit types. This means for example that the fraction of Mark 4 miscalled as Mark 104 is equal to the fraction of Mark 104 miscalled as Mark 4. The cross

Figure 8.9. Distributions are plotted without ambiguity correct efficiency (unshaded) and after (shaded) the normalized correction is applied. Figures 8.9a-d are the Mp π , t, θ_{Jac} and ϕ_{TY} respectively.







section correction factor for Mark 2 miscalled as Mark 4 or Mark 104 in the $^{\Delta++}$ region is 0.934. This will be discussed more in Chapter IX.

CHAPTER IX

CROSS SECTION AND NORMALIZATION

The corrections from Chapters V-VIII can be tabulated to give a cross section for the final sample. The $\Delta ++$ cross section normalization factors are given in Table 9.1.

Some of the errors derived above are purely statistical. Others have other factors folded in. The pion decay error, for example, combines the 2% decay error with a 16% Teuta fitting error. The strong interaction error includes the error due to the posibility that for heavy nuclei, all elastic scatters may not be lost in the production programs and includes also an average error in the experimental cross section.

The ambiguity over-correct correction is the best estimate of how many events are corrected twice, once due to one of the first four items on the list and again in the ambiguity weight correction.

The two zero acceptance corrections are due to the lower acceptance for high mass. In the pole extrapolation,

Table 9.1.-- A++ Cross Section Factors.

Correction	Factor
Strong Scattering Proton	1.0377 7 0.0018
Strong Scattering Pion	1.0322 + 0.0017
Coulomb Scattering	1.03 ± 0.0012
Pion Decay	1.0275 <u>+</u> 0.005
DE/DX Efficiency	1.06 ± 0.005
Spark Chamber Efficiency	1.093
Forwards Backwards Symmetry	2.0
Confidence Level Cut	1.03 ± 0.005
Acceptance = 0 M<1.36 Gev	1.11 ± 0.007
Acceptance = 0 M<1.42 Gev	1.14 ± 0.007
Circe Standard Deviation Cut	1.29
Ambiguity Weight	1.62 ± 0.032
PPπ° Correction	0.934 ± 0.01
Ambiguity Overcorrect	0.96 <u>+</u> 0.005

the data are cut at $Mp\pi+<1.36$ GeV and the zero acceptance correction for this data is 1.11. For the $\Delta++$ cross section, the mass cut is $Mp\pi+<1.42$ GeV and so the larger 1.14 zero acceptance weight is used here. The Circe standard deviation weight comes from the ratio given by

$$R = \frac{\text{Total Teuta Fits}}{\text{Teuta with Stan. Dev. } < 0.6}$$
 (9-1)

This cut was applied to the total 49996 good Teuta fits and reduced it to 38738 as mentioned in Chapter III. The Mark 2 correction is obtained to account for the fraction of $PN\pi$ + events in the Δ ++ region which fit as $PP\pi$ °. A program using PP+PPπ° data at 6.6 Gev/c³⁶ similar to the $PN\pi$ + Monte Carlo program was written to generate fake $PP\pi^{\circ}$ events. Errors were induced in these events and it was found that the loss ratio for PP π ° is the same as PN π +. This fact can be used to estimate the $PN\pi+$ events gained from $PP\pi^{\circ}$ which tend to decrease the effect of events going the other way. This requires a knowledge of the acceptance of $PN\pi+$ and $PP\pi^{\circ}$ events by our apparatus and the cross sections at P = 6 Gev/c. Table 9.2 list the acceptance for $PN\pi+$ and $PP\pi^{\circ}$ as determined by comparing the actual bubble chamber data orbited through the magnet and the Monte Carlo fake events generated at $P_R = 6$ GeV/c for each event class. Also listed are the interpolated cross sections. 5

Because of the simulated event ambiguity using Monte Carlo events, 400 events out of 1977 good PN π + are

Table 9.2.--Acceptance for $PN\pi+$ and $PP\pi^{\circ}$.

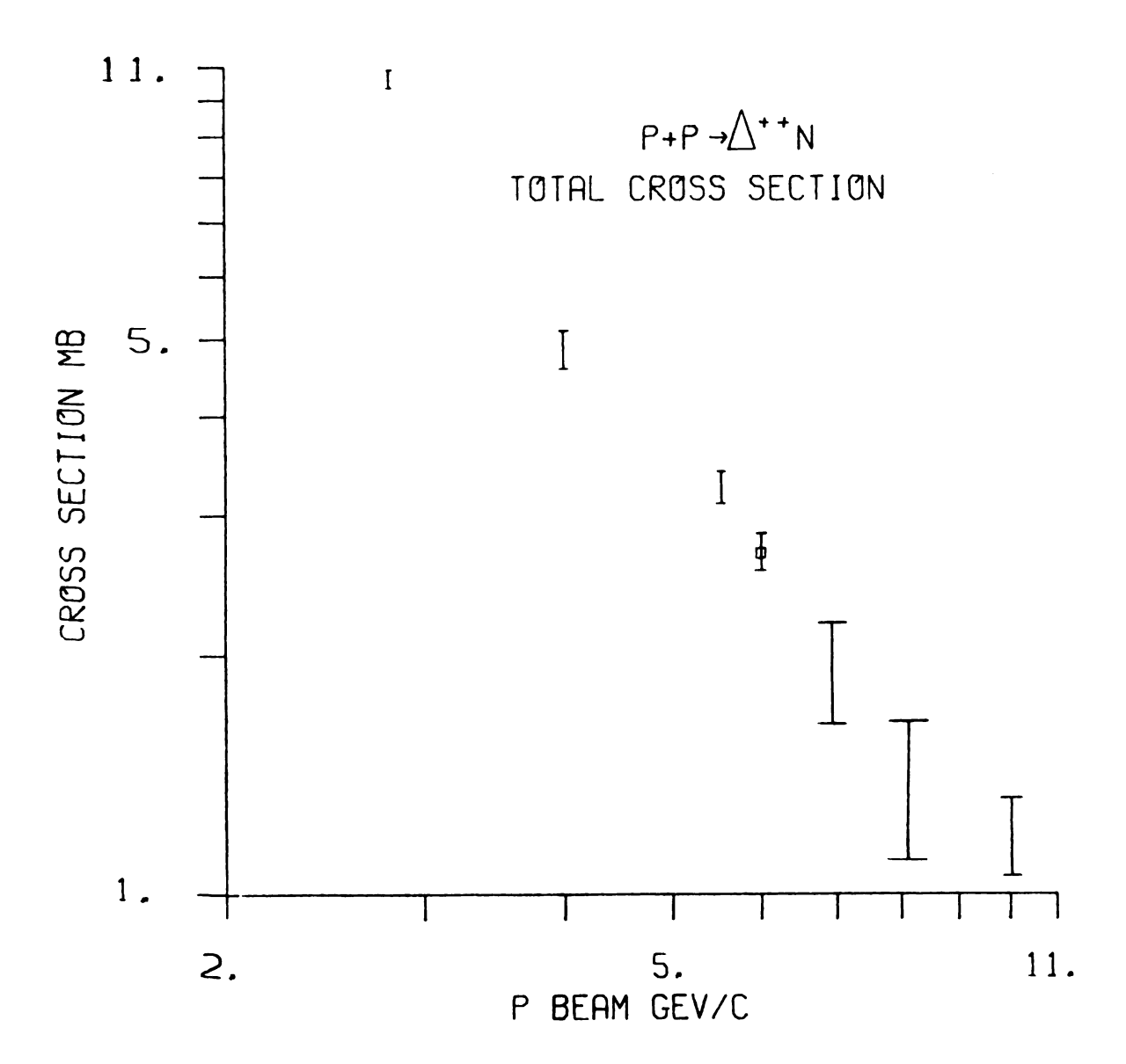
	PNπ+	PРπ°
Acceptance	0.0898 <u>+</u> .006	0.047 <u>+</u> .005
Cross Section at 6 Gev/c	6.86 mb	2.8 mb

lost to PP π °. Combining this with the data in Table 9.2, one calculates that 88 PP π ° events should swap back decreasing the swapping correction by 0.934.

The combination of all factors in Table 9.1 is 5.83. As listed in Chapter III, this experiment yields $12001 \Delta ++$ events at a mb/event of 0.01113. This combined with the average geometry weight of $2.35 \pm .11$ gives the $\Delta ++$ cross section of 1.83 ± 0.1 mb for t<0.3 Gev² and 1.14< M<1.42 Gev. Equation 8-9 gives the ratio of the Breit-Wigner fit events to the mass cut events as 1.476. This leads to $\sigma(\Delta ++) = 2.702 \pm 0.15$ mb (9-2). This cross section can be seen plotted along with near by values⁵ in Figure 9.1.

The total PP+PNm+ cross section is presented here
Only for completeness. The error is large because the
experiment has no way of determining the acceptance for the
entire class of PNm+ events. An attempt was made to get
the acceptance by orbiting the bubble chamger events
through the apparatus. 22 Also Monte Carlo studies have
been made to determine the acceptance at 6.0 Gev/c. The

Figure 9.1. $\Delta ++$ cross section at 6 Gev/c plotted with near by values.



 $PN\pi+$ acceptance is given in Table 9.2. Other correction factors that apply are identical to those in Table 9.1. The changes are listed in Table 9.3.

Table 9.3--PN π + Cross Section Factors.

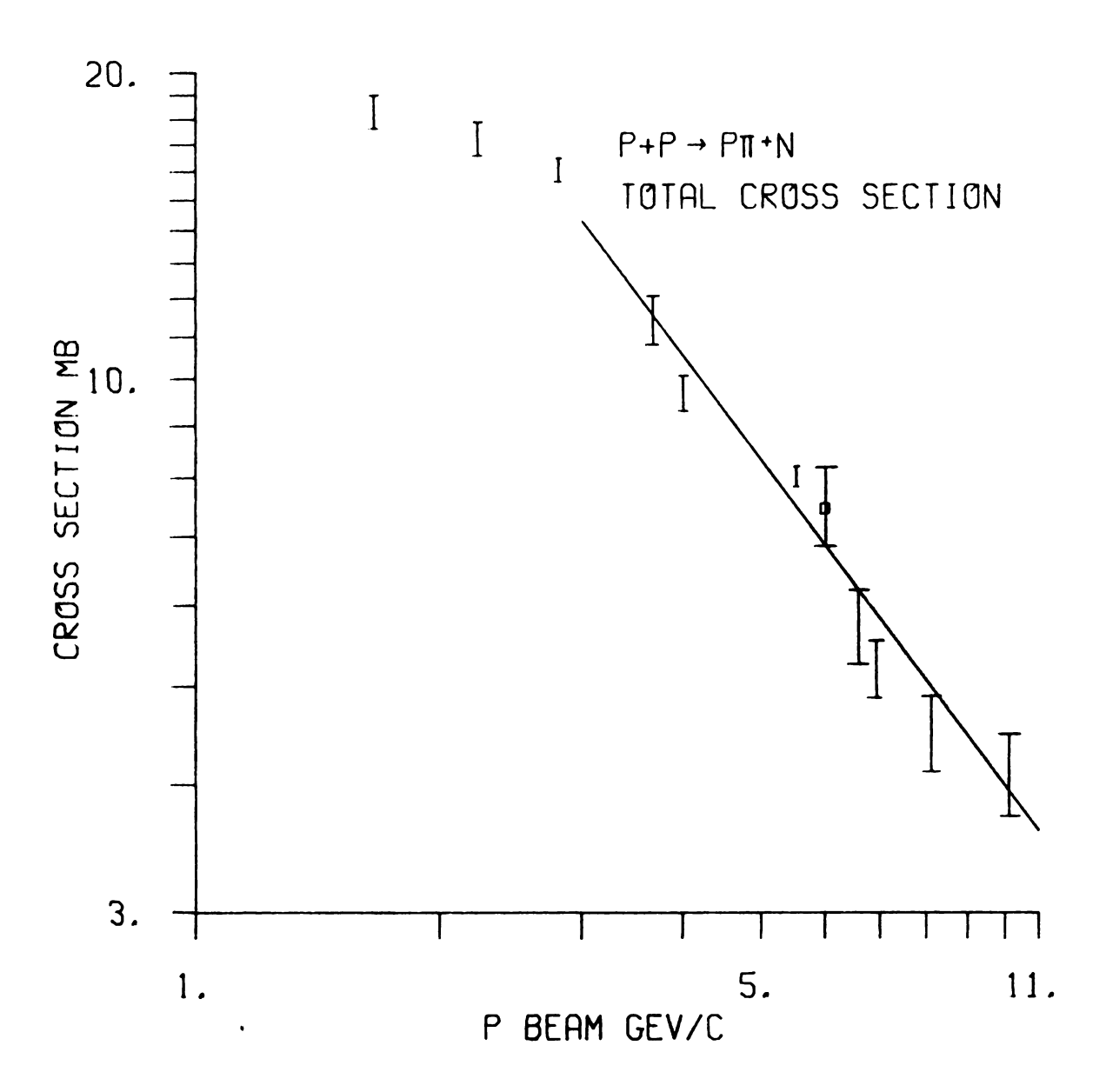
Correction	Factor
Swap Weight	1.209 <u>+</u> 0.024
Mark 2 Correction	0.956 <u>+</u> 0.01

There are 31908 PN π + after a Circe standard deviation cut of 0.6 and 41180 after the correction factor of 1.2906 is applied. This gives

$$^{\sigma}PN\pi + = 7.58 \pm 0.7 \text{ mb}$$
 (9-3)

This cross section is plotted in Figure 9.2 along with near by values.⁵ The line is a fit to the data of the form $\sigma = a(|P_{lab}|)^b$. The fit values previously known²² with a = 45.9 and b = -1.06 are used.

Figure 9.2. PN π + cross section. This experiment at 6 GeV/c along with other values.



CHAPTER X

ONE PION EXCHANGE

10.1 Kinematics

In 1959 G. F. Chew and F. E. Low presented a scheme for analyzing experiments so that elementary cross sections of constituents of complex targets can be obtained. They argue that residues of poles known to exist in field theory are related to measurable quantities in physical regions of scattering and the value of the residues can be found by extrapolating off-shell scattering data into the unphysical region to the pole. The diagram considered here is shown in Figure 10.1.

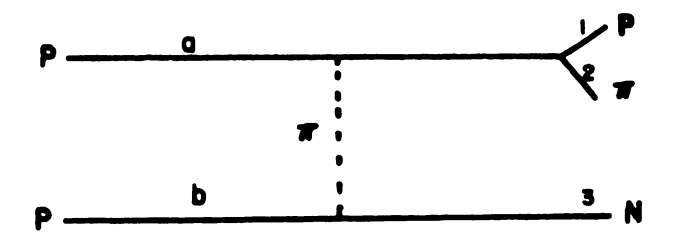
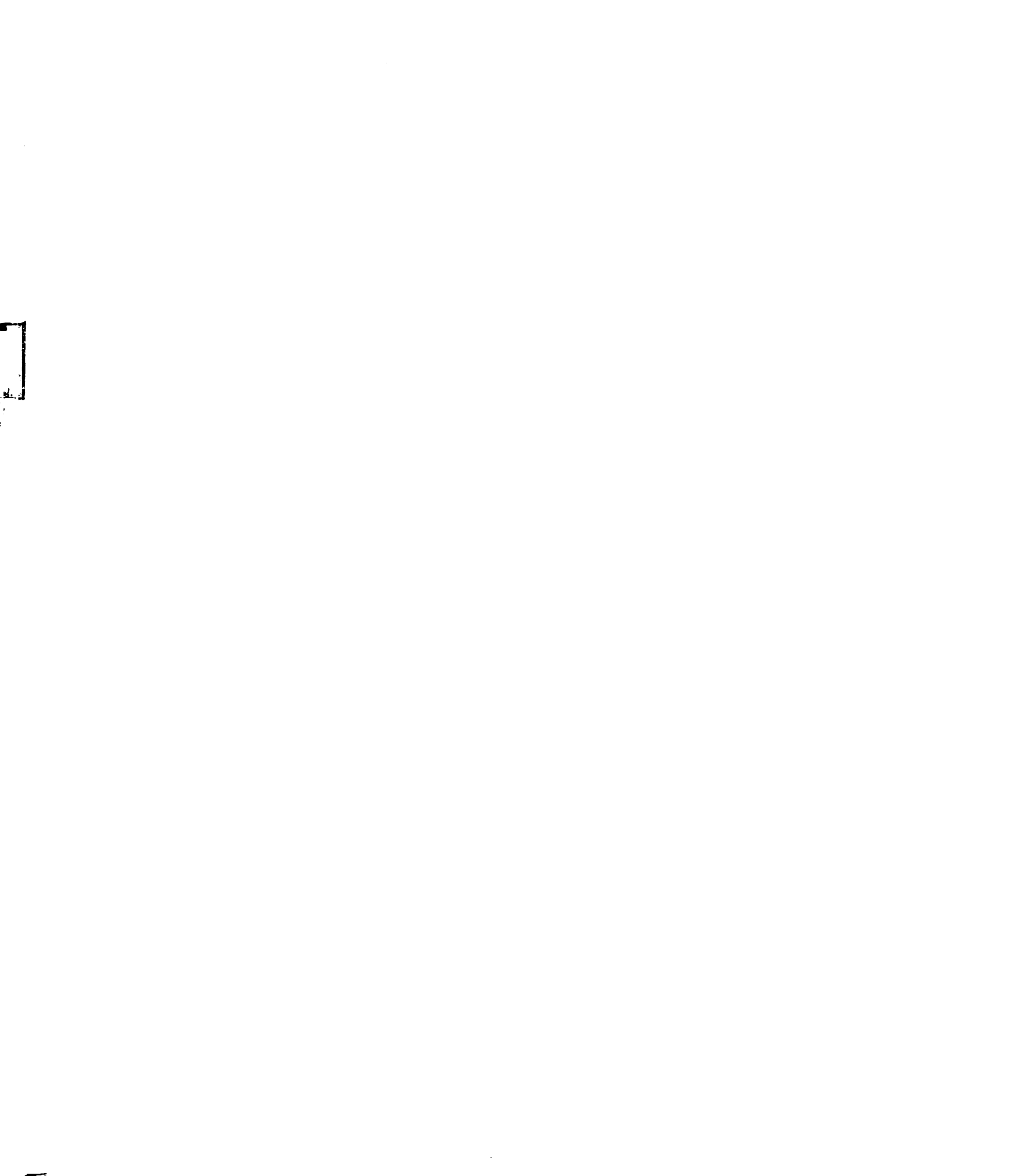


Figure 10.1. One pion exchange (OPE) diagram for PP+P π +N.



The cross section σ is the transition probability per unit flux of incident particles where the flux is the product of the particle densities, $4E_aE_b$, and the relative velocity v. One can write 37

$$\frac{d\sigma}{d^{3}\vec{P}_{1}d^{3}\vec{P}_{3}d^{3}\vec{P}_{3}} = \frac{(2\pi)^{4}}{4E_{4}E_{4}V} \frac{1}{(2\pi)^{9}} \int_{0}^{(4)} (P_{1}^{M} + P_{2}^{M} + P_{3}^{M} - P_{4}^{M} - P_{4}^{M}) \frac{|\vec{M}|^{2}}{2E_{1}2E_{2}2E_{3}}$$
(10-1)

If the initial state is denoted by $|\alpha\rangle = |a,b\rangle$ and the final state is denoted by $|\beta\rangle = |1, 2, 3\rangle$ then $|\overline{M}|$ is $\sum_{\alpha} \sum_{\beta} |\langle \beta | T | \alpha \rangle|^2$. In this calculation one needs to write the cross section in terms of M_{12}^2 , θ_{Jac} , ϕ_{TY} , S and t where $M_{12}^2 = (P_1^{\ \mu} + P_2^{\ \mu})^2$, $S = (P_a^{\ \mu} + P_b^{\ \mu})^2$, $t = (P_3^{\ \mu} - P_b^{\ \mu})^2$ and θ_{Jac} and ϕ_{TY} are defined in Appendix C.

In this chapter, the four-vector P^{μ} of a particle is related to its three-vector \vec{P} and energy E by P^{μ} = $(E,i\vec{P})$. One can define $K^{\mu} = P_1^{\ \mu} + P_2^{\ \mu}$ and note $M_{12}^{\ 2} = K^{\mu}K^{\mu} = K^2$ and also $E_a E_b v = M_b |\vec{P}_a|$. One can multiply the integral of equation (10-1) times 1, where

$$1 = \int \int_{0}^{(4)} (P_{1}^{M} + P_{2}^{M} - K^{M}) d^{4}K \int_{0}^{4} (K^{2} - M_{12}^{2}) dM_{12}^{2} \qquad (10-2)$$

and substitute $K^{\mu} = P_1^{\mu} + P_2^{\mu}$ to get

$$d\sigma = \frac{1}{4M_b |\vec{P}_{a}| (2\pi)^5} \int \frac{d^3 \vec{P}_1 d^3 \vec{P}_2 d^3 \vec{P}_3}{2E_1 2E_2 2E_3} \int_{0}^{(4)} (K^M + P_3^M - P_a^M - P_b^M) \cdot \int_{0}^{(4)} (P_1^M + P_2^M - K^M) d^4 K |\vec{M}|^2 \delta(K^2 - M_{12}^2) dM_{13}^2$$
(10-3)

One can define K_0 by $K^{\mu} = (K_0, i\vec{K})$ which implies $K^2 = K_0^2 - \vec{K}^2$. One can write

$$\delta(K^2 - M_{12}^2) = \delta\left[\left(K_0 + \sqrt{\frac{2}{K^2 + M_{12}^2}}\right)\left(K_0 - \sqrt{\frac{2}{K^2 + M_{12}^2}}\right)\right] (10-4)$$

Also remembering $\int_{0}^{\infty} dx \, \delta$ (ax) = 1/a, one obtains after integrating over K_{0}

where $K_0 = \sqrt{M_{12}^2 + K^2}$ is implicitely implied in the two remaining δ functions in this expression.

It is useful to consider now only the two body phase space term

$$\int \frac{d^{3}\vec{P_{1}} d^{3}\vec{P_{2}}}{2E_{1} 2E_{2}} S^{(4)}(P_{1}^{M} + P_{2}^{M} - K^{M}) \qquad (10-6)$$

contained in equation (10-5).

The integral over d^3P_2 can easily be done, and the remaining integral can be done by recalling

$$\int \int (g(x)) f(x) dx = f(x_0) / g'(x_0) \qquad (10-7)$$

where $g(x_0) = 0$.

Equation 10-6 can now be integrated to give

where Q refers to the proton momentum in the $\Delta ++$ center of mass. Equation (10-5) now becomes

where $\sqrt{\hat{K}^2 + M_{12}^2}$ has been replaced by E_{Δ} . The remaining variables of integration in equation (10-9) can be evaluated in the over-all center of mass. One can concentrate on the two body phase space integral

$$\left(\frac{d^{3}\vec{K}d^{3}\vec{P}_{3}}{2E_{3}}S^{(4)}(K^{M}+P_{3}^{M}-P_{a}^{M}-P_{b}^{M})\right) \qquad (10-10)$$

This integral has exactly the same form as equation (10-6) except it is missing a factor of $2E_{\Delta}$ in the denominator. Equation (10-10) can be integrated to give

where P is $|\vec{P}_1 + \vec{P}_2|$ or $|\vec{P}_3|$ in the over-all center of mass and E_{Δ} is $\sqrt{(\vec{P}_1 + \vec{P}_2)^2 + M_{12}^2}$.

Combining equation (10-9) and (10-11) gives

One can expand t in the center of mass as given earlier in this chapter as

$$t = M_a^2 + M_{12}^2 - 2 E_a E_b + 2 |P||P_a| \cos \theta$$
 (10-13)

and it follows that

$$P = \frac{dt}{2|P_a| d\cos\theta}$$
 (10-14)

One can write 37

$$P = \frac{M_b |P_a|}{\sqrt{S}} \qquad (10-15)$$

Combining equations (10-12), (10-14), and (10-15), and integrating (10-12) over all angles but $\cos \theta$ gives

$$\frac{d\sigma}{dM_{12}dt} = \frac{Q |\vec{M}|^2}{128 (m_b P_a)^2 (2\pi)^3}$$
 (10-16)

10.2 Vertex Contributions Without Form Factors

If one considers for the moment the particles in Figure 10.1 to have no spins, the invariant amplitude $|\overline{M}|^2$ will be a function of five independent energies 37 s_{ij} = $(P_i + P_j)^2$ (i, j = 1, 2, 3, 4, 5). When 1 and 2 are known to produce a resonance, one can assume a plausable form for T as

To describes the background term which when integrated by itself becomes the phase space term for the reaction. The term is neglected here because in Chapter 8.2 the phase space was observed to be 4%. The Breit-Wigner term and the coupling constant G in equation (10-17) will be replaced by the on-shell cross section.

When spins are taken into consideration, one gets additional t dependence. The amplitude for pseudo-scalar exchange for a spin 1/2 to spin 3/2 baryon is

where v is a vector required for the expression to be Lorent z invariant. One can let $v = P_a$ and one can write the spin 3/2 vector $\bar{U}_{\lambda 12}$ (P_{12}) as 38

where $\varepsilon^{*\lambda}(P_{12})$ is the spin 1 spinor and μ^{λ} (P_{12}) is the spin 1/2 spinor.

The vertex factor can be averaged over initial spins and summed over final spins to give 11

$$G_{\Delta P \pi} \frac{Q_t}{m_a} \sqrt{(m_a + m_{12})^2 - t}$$
 (10-20)

 $^{G}\Delta P\pi$ is the coupling constant for the p- π - Δ vertex and is related to the on-shell cross section $\sigma(M)$. Q_{t} is the offshell pion and proton momentum in the $\Delta++$ center of mass. One can define the function $R(M_{1}, M_{2}, M)$ as

$$R(M_1, M_2, M) = \sqrt{[M^2 - (M_1 + M_2)^2][M^2 - (M_1 - M_2)^2]}/2M$$
(10 - 21)

 $R(M_1, M_2, M)$ is the momentum of the two particles of mass M_1 and M_2 in their center of mass with a center of mass energy of M. Q_t in equation (10-20) can be written as

$$Q_t = R(Ma, t, M_{12})$$
 (10-22)

In order to incorporate the resonance part of the transition matrix properly, it is necessary to relate the Off-shell scattering to the on-shell scattering. Following Jackson³⁹ one can calculate the ratio of off-shell cross section to the on-shell cross section with a real pion in the cross channel. This leads to a form factor

$$\frac{d\sigma}{d\sigma_{p}} = \frac{Q_{t}^{2}}{Q^{2}} \left[\frac{(M_{a} + M_{12})^{2} - t}{(M_{a} + M_{12})^{2} - \mathcal{U}^{2}} \right] (10 - 23)$$

Q is defined using equation (10-22) as

Notice that as $t+\mu^2$, the ratio is unity, but in the physical scattering region, the ratio is greater than unity and increases with increasing t.

The lower vertex of the amplitude in Figure 10.1 can be calculated using Feyman rules neglecting for now the form factors. The helicity amplitudes associated with the lower vertex can be calculated from

One can write the helicity amplitudes explicitely in the center of mass for scattering along the x axis in the x-z plane. Equation (10-25) can be reduced to $\text{Tp+N}\pi = \text{Gp}\pi\text{N}^{\bullet}$. Neglecting the proton-neutron mass difference gives

$$T_{P \to N\pi} = G_{PN\pi} \sqrt{|t|} \qquad (10-26)$$

 $G_{p\pi N}^2/4\pi$ is taken for the charged pion coupling as 29.2

One can combine the phase space factors, lower vertex factors and upper vertex factors along with the appropriate normalizations. 2, 40, 41 to give

$$\frac{d^{2}\sigma}{dtdM_{12}} = \frac{QM_{12}^{2}G_{PRN}^{2}|t|}{2\pi M_{2}^{2}P_{a}^{2} + \pi} \frac{|t|}{(t-M_{1}^{2})^{2}} \sigma(M_{12}) \left\{ \frac{Q_{4}^{2}}{Q^{2}} \left[\frac{(M_{a}+M_{12})^{2}-t}{(M_{a}+M_{12})^{2}-M_{2}^{2}} \right] (10-27) \right\}$$

Considering the 1-2 or proton-pion system to be the $\Delta++$ resonance, Q is the on-shell momentum of the pion in the $\Delta++$ rest frame and Q_t is the momentum when the pion is off-shell. M_b and M_a are the proton mass and P_a is the lab momentum of the beam. T is the momentum transfer square for the target-neutron system and $\sigma(M_{12})$ is the on-shell cross section for $\pi+-P$ elastic scattering. The expression before the curly brackets is the Chew-Low¹ pole expression and the curly brackets come from the spin sum of the $\Delta++$ production vertex.

10.3 Dürr-Pilkuhn Corrections

Dürr and Pilkuhn¹² utilized a technique well known to Nuclear Physics⁴² to arrive at a vertex correction which takes into account the lack of the angular momentum barrier for $r < R_O$, where r is the distance of the pion to the baryon and R_O is the interactive radius of the baryon. One can substitute for $r < R_O$ a complex radial symmetric potential. One can obtain the transmission coefficient as the ratio of incident intensity to reflected intensity by equating the

first derivatives of the inside and outside solution of the nonrelativistic radial Schrodinger equation at r = R. The transmission coefficient is

$$t_L(x) = \frac{S_L h_L}{(g_L - \Delta_L)^2 + (S_L + h_L)^2}$$
 (10-28)

where Δ_L and S_L are the real and imaginary parts of the logarithmic derivative of the outgoing spherical wave and g_L and h_L are the real and imaginary parts of the logarithmic derivative of the total radial wave in the outside region. The usual penetration factor can be given as

$$V_{L} = S_{L}(KR)/k_{R}. \qquad (10-29)$$

The reaction cross section can be written as

$$\sigma_{x,L} = \frac{4\pi}{K^2} (2L+1) t_L(x) . (10-30)$$

If the energy is not high we have k << K; then the derivatives from the total radial solution are proportional to KR which is larger than the kR from the outgoing wave derivative and results in

$$t_{L}(x) = {}^{S_{L}/KR} = k/_{K} V_{L}.$$
 (10-31)

One can see that the penetration factor is proportional to the reaction cross section for a given K and k. The penetration factor for L = 1 is $V_1(x) = \frac{x^2}{1+x^2}$.

The form factors used by Dürr and Pilkuhn for L = l are

$$F_{(t)} = \left(\frac{1 + R^2 Q^2}{1 + R^2 Q_4^2}\right) \qquad (10-32)$$

The parameters R, Q, and Q_t have the same meaning for both the $P\pi\Delta++$ and the $P\pi N$ vertex. R is the radius of the $\Delta++$ or nucleon. Q_t is the momentum of a pion of mass square t in the $\Delta++$ or neutron center of mass and Q is the same quantity taken on-shell. The expression for Q_t and Q were taken for the $\Delta++$ vertex in equation (10-22) and (10-24) in terms of equation (10-21). If one is considering the $P\pi N$ vertex then the values for the on-shell momentum are $q = R(M_D, \mu, M_3)$, where M_D is the proton mass, μ is the pion mass, M_3 is the neutron mass and R is defined by equation (10-21). q^2 in this case is negative. One also gets $q_t = R(M_D, t, M_3)$. The radius are taken from Wolf as $R_N = 2.66$ Gev and $R_A = 4.0$ Gev $R_A = 4.0$ GeV

10.4 Benecke and Dürr Corrections

In 1967 Benecke and Dürr¹³ (B.D.) derived form factors which can be used for a resonance vertex to account for finite extension of the strong interacting matter. Consider the upper vertex of Figure 10.1 where the reaction π off + P+ π on + P occurs. Figure 10.2 illustrates the exchange graph considered by Benecke and Dürr.

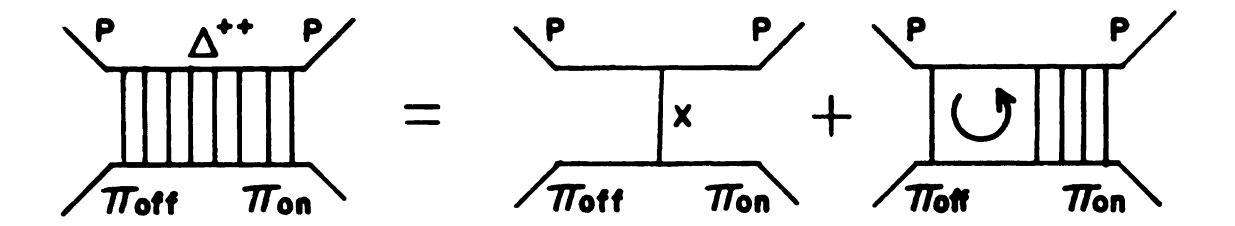


Figure 10.2. Exchange graph of scalar particle with mass X.

One can write the jth partial wave projection of the Bethe-Salpeter equation with the above form as $g_j = g_j^0 + \lambda g_j K_j$, where g_j^0 is the Born term and K_j is the jth partial wave projection of the propagator for the loop integral indicated by the arrow in Figure 10.2 One can see the a schematic solution 43 of the equation is $g_j = g_j^0/(1-\lambda K_j)$ where if one considers this as describing a resonance propagating in the S-channel then the vertex coupling is that of the Born approximation type and the denominator can be made to look like $(M_i^2 - i M_j \Gamma_j - S)$.

In practice the form factors arise by obtaining the imaginary part of the denominator of the approximated solution. The penetration factor can be identified by comparison of this width term to the non-relativistic width to give $v_j(x) = 1/2x^2 Q_j(1 + 1/2x^2)$, where Q_j are the Legendre functions of the second kind. For a p-wave resonance, one obtains

$$V_1(x) = \frac{1}{2 \times 2} \left[\frac{2 \times 2 + 1}{4 \times 2} \ln(4 \times 2 + 1) - 1 \right]$$
 (10-33)

It will be noted that these penetration factors go to 0 as $x \rightarrow \infty$ unlike the Durr Pilkuhn penetration factors which approach 1 as $x \rightarrow \infty$. Also the form above will give a complex number when the argument of the log becomes negative. This does occur for non-resonance decays like $P \rightarrow \pi + N$ when the pion is considered on-shell.

One can write the Benecke Dürr form factors for the $\Delta + + \mbox{ vertex}$ as

$$F_{\Delta N\pi}(t) = \frac{V_1(Q_tR_{\Delta})}{V_1(Q_tR_{\Delta})} \quad (10-34)$$

where Q_{t} and Q are the off and on-shell pion momentums in the $\Delta++$ center of mass given by equations (10-22) and (10-24) and the R_{Δ} is obtained from Wolf to be $R_{\Delta}=2.2~{\rm Gev}^{-1}.3$

10.5 Corrected Cross Section and Pole Extrapolation

The double differential cross section was written (equation 10-27) in the Born approximation in the absence of form factors as

$$\frac{d\sigma}{dM_{12}dt} = \frac{1}{2\pi} \frac{G_{PNR}^{2}[t]}{4\pi} \frac{G_{PNR}^{2}[t]}{4\pi} \frac{Q_{12}^{2}[t]}{(t-M_{12})^{2}} \frac{Q_{12}^{2}[(M_{0}+M_{12})^{2}-t]}{Q_{12}[(M_{0}+M_{12})^{2}-t]} Q_{12}(\eta_{12})$$
(10-35)

 $g^2(t)$ is an addition form factor fitted to the data. One obtains for $g(t) = (C - u^2) / (C - t)$ a value for C of 2.3 Gev².³ The M₁₂ above is the mass of the resonance in Gev and $\sigma(M_{12})$ is the on-shell mass value at M₁₂.

The Durr-Pilkuhn model modifies the vertex factors to give

$$t \rightarrow t \left[\frac{1 + R_N^2 g^2}{1 + R_N^2 g^2} \right] \qquad (10 - 36)$$

and

$$Q\left(\frac{Q_{t}}{Q}\right)^{2}\sigma(M) \rightarrow Q\left(\frac{Q_{t}}{Q}\right)^{2}\left[\frac{1+R_{0}^{2}Q^{2}}{1+R_{0}^{2}Q_{t}^{2}}\right] (10-37)$$

The Benecke Durr cross section can be obtained for the resonance vertex by the following substitution:

$$Q\left(\frac{Q_{t}}{Q}\right)^{2}\sigma(M) \rightarrow Q\left(\frac{Q_{t}}{Q}\right)^{2} \frac{V_{1}(QR_{0})}{V_{1}(Q_{t}R_{0})} \quad (10-38)$$

where

$$V_1(x) = \left[\frac{2 \times^2 + 1}{4 \times^2} \ln (4 \times^2 + 1) - 1 \right]$$
 (10-39)

The pole extrapolation can be illustrated by using the pole equation and the various off-shell effects are substituted as described above. At the pole, the cross section becomes 4

$$\frac{d\sigma}{dMdt} = \frac{1}{2\pi M_b^2 P_a^2} \frac{G_{PN\pi}^2}{4\pi} \frac{1+1}{(t-u^2)^2} M_{12}^2 Q \sigma(M_{12}) (10-40)$$

and one can write for the quantity "to"

"to" =
$$\frac{N/s}{\int dM dt} \frac{2\pi M_b^2 P_a^2 4\pi (t-M^2)^2}{M_{12}^2 Q G_{PNR}^2}$$
 (10-41)

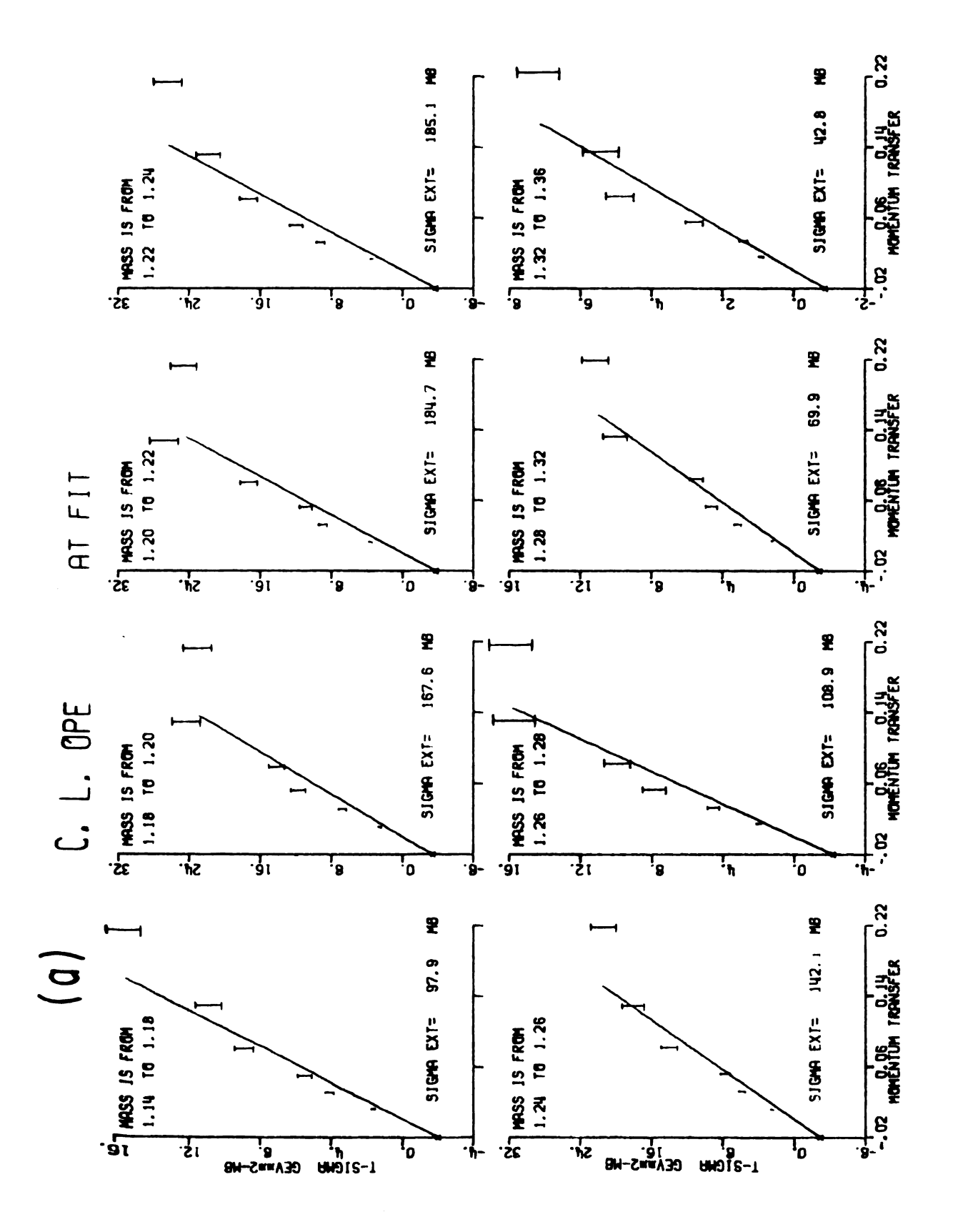
To evaluate "to" one can divide the experimental off-shell scattering data into bins of mass and t. N is the number of events in a particular bin and S is the ub/events in the experiment; $s = 0.00001113 \text{ m}_{b}/\text{event}$ as given in Chapter III.

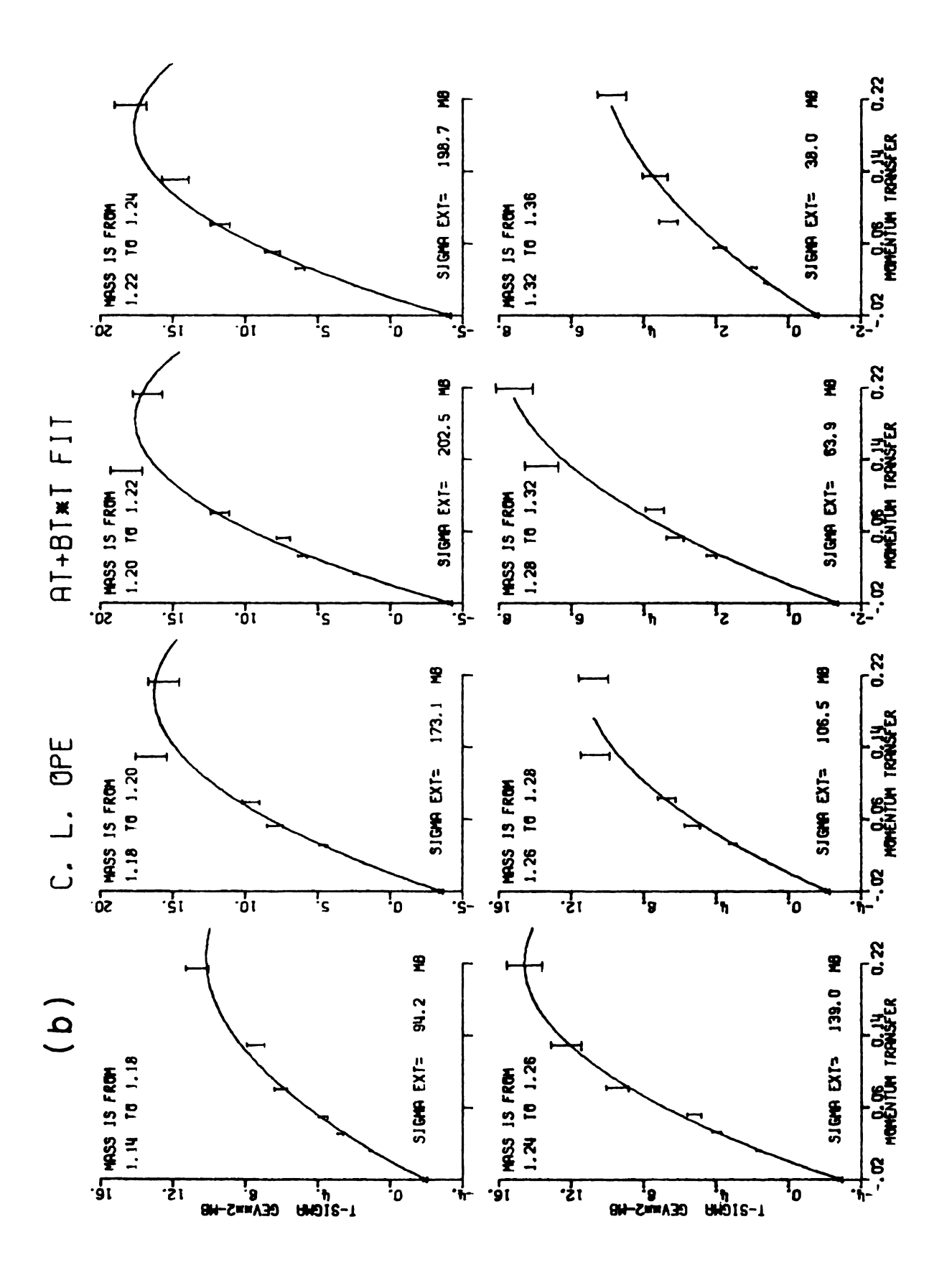
The expression \int dMdt is taken over the portion of the M - t bin experimentally accessible after kinematical restrictions like t_{min} effects are considered. The average of the factors on the right hand side of equation (10-41) are used to represent "to" at the average t and M point of the interval. The extrapolation form factors can be incorporated into the above expression to give a smoother off-shell dependence for the data. Various extrapolation polynomials are used for the Chew-Low formula given above or with the Dürr Pilkuhn and Benecke Dürr corrections. Figures 10.3a-f shows the "to" points and fitted curve for polynomials of the type at and at + bt 2 for the Chew-Low, Dürr Pilkuhn and Benecke Dürr off-shell correction factors. Table 10.1 shows a summary of the χ^2 for these fits and also for fits of the type at + bt² + Ct³. The column marked Fac is a multiplication factor used to scale all experimental

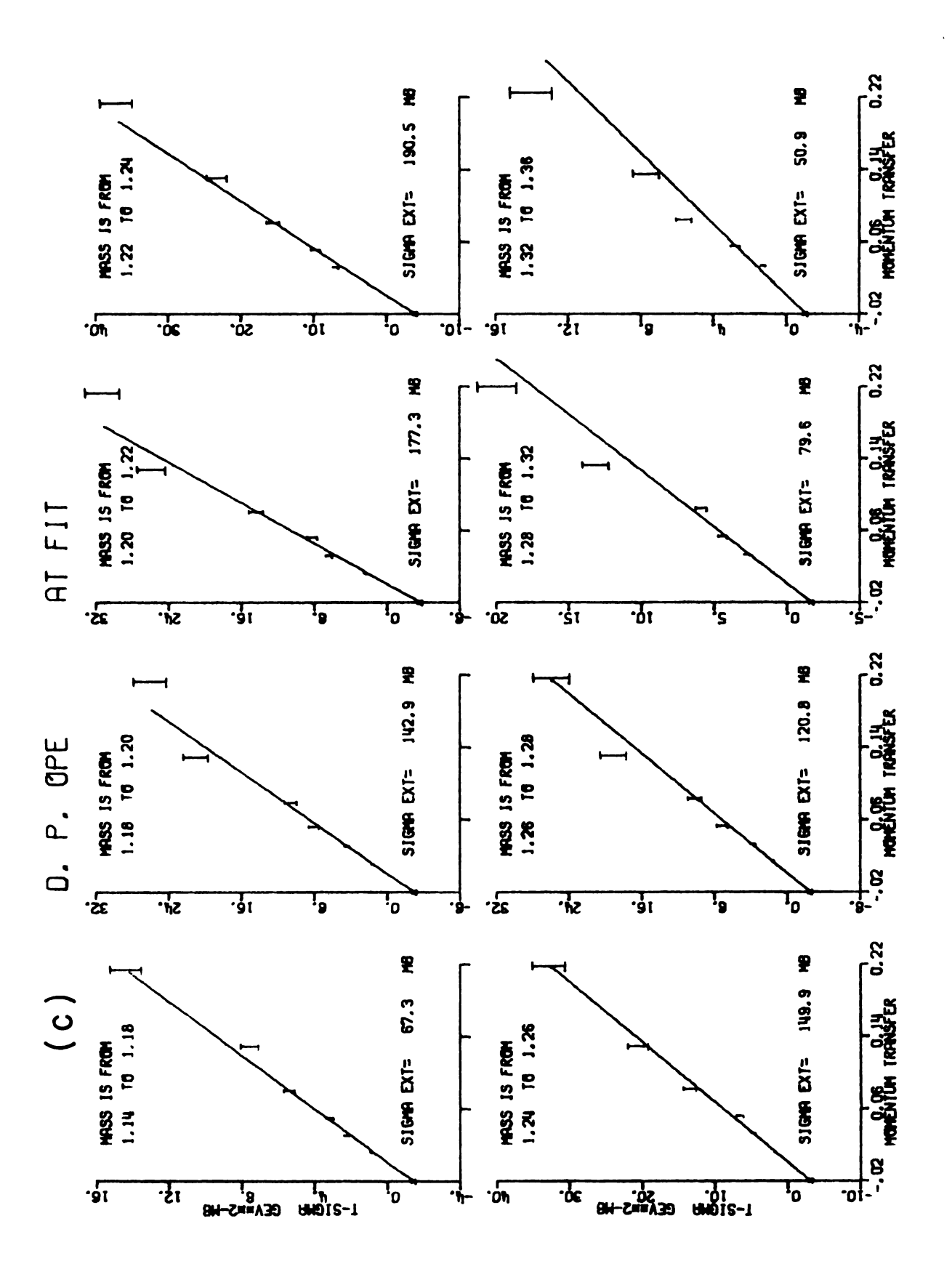
Figure 10.3. a-b. Chew-Low extrapolation curves.

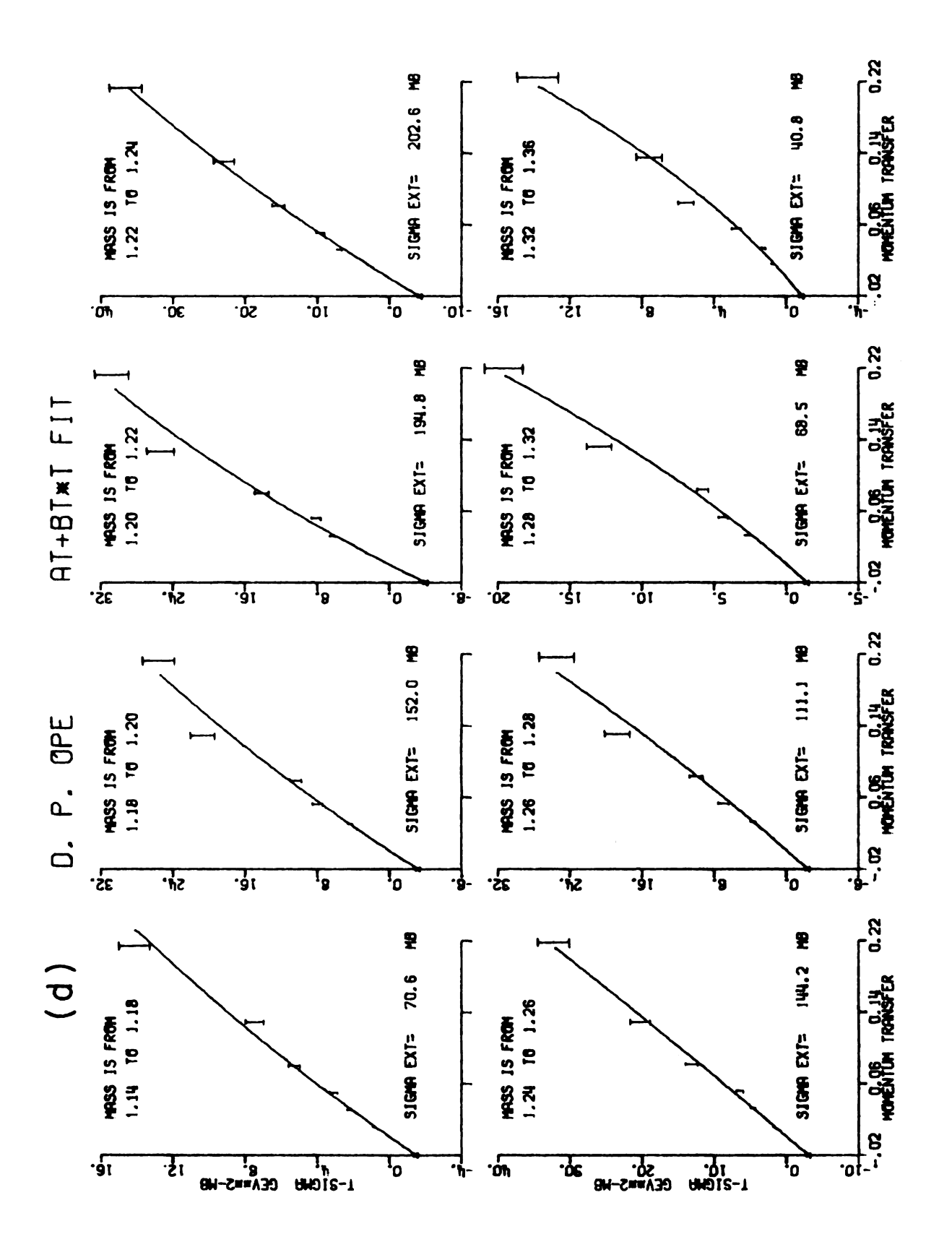
c-d. Dürr Pilkuhn extrapolation curves.

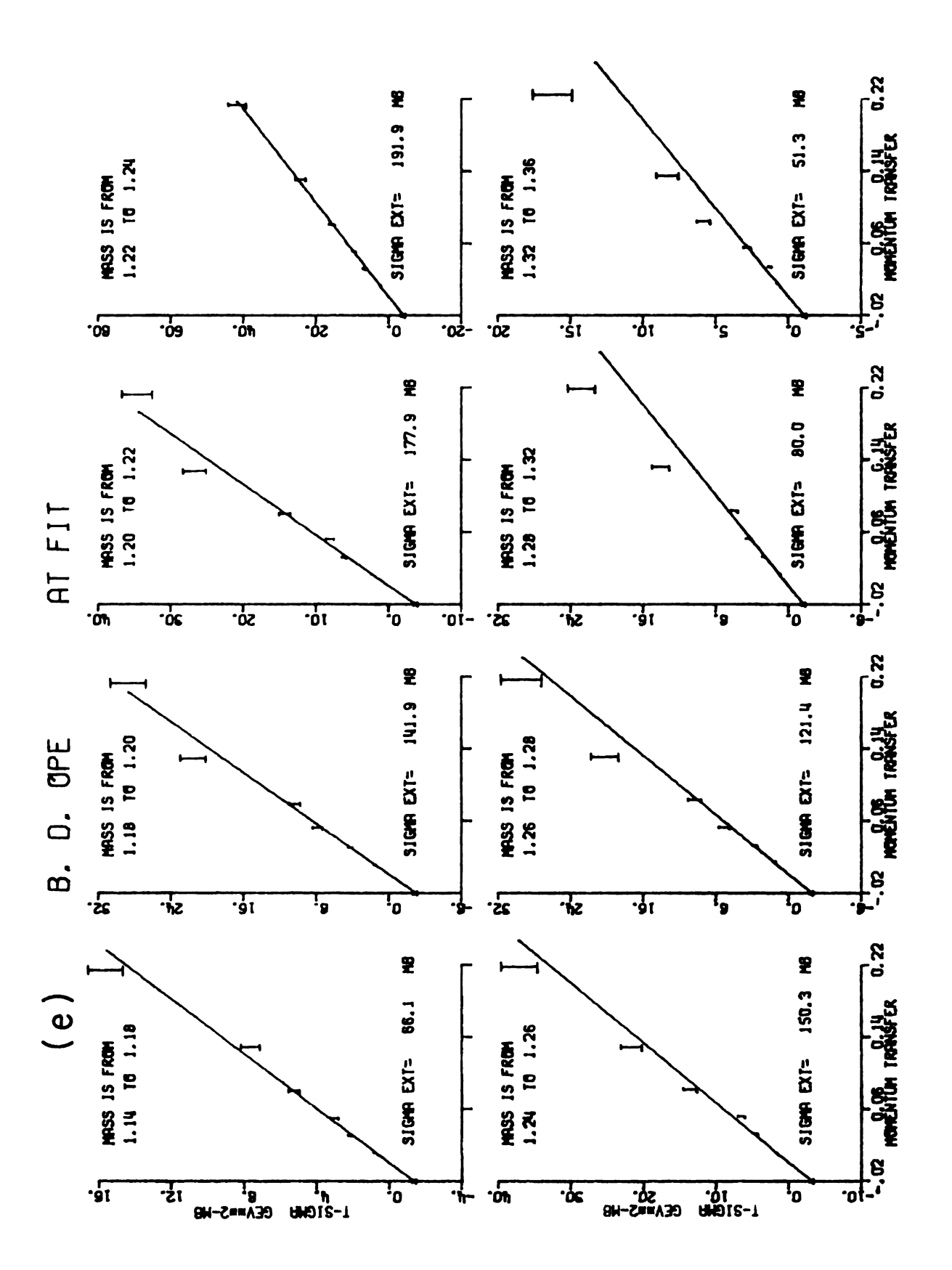
e-f. Benecke Dürr extrapolation curves.











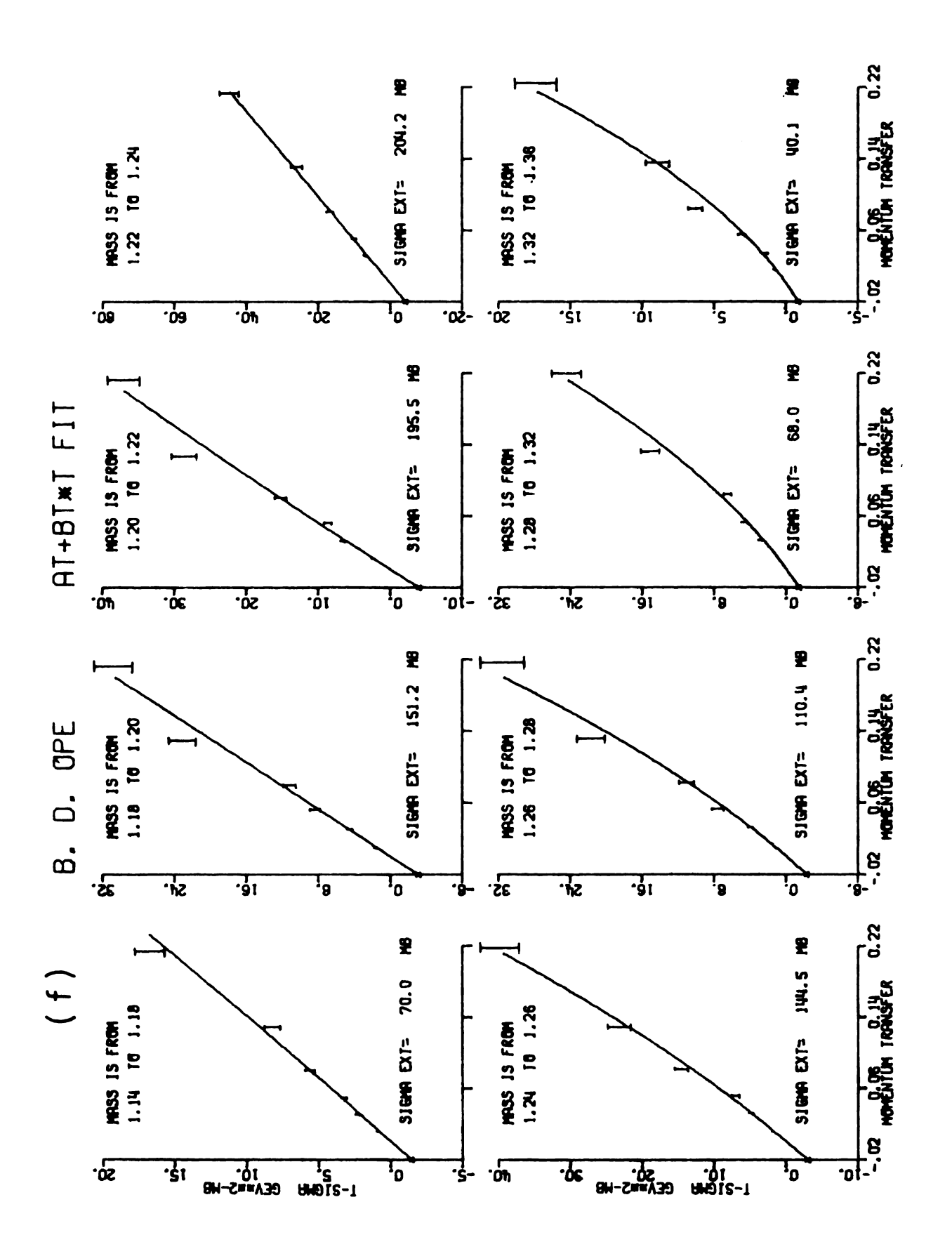


Table 10.1.--Chi-Square and Multiplier for at, at + bt² and at + bt² + ct³ fits.

Fit Type	1	2	3	4	5	6	7	8	Fac	χ²
DP - AT	10.	12.	26.	10.	9.	12.	25.	31.	.98	60.
BD - AT	9.	8.	16.	5.	16.	21.	42.	45.	1.07	57.
CL - AT	83.	114.	189.	160.	89.	68.	65.	41.	.68	241.
DP - AT + BT ²	8.	8.	15.	5.	8.	9.	15.	17.	.999	15.
BD - AT + BT ²	8.	8.	15.	5.	8.	9.	15.	16.	1.002	13.
CL - AT +	7.	7.	13.	7.	8.	6.	14.	15.	.998	129.6
DP - AT + BT ² + CT		7.	14.	5.	8.	3.	15.	14.	.95	25.
BD - AT + BT ² + CT		7.	14.	5.	8.	3.	15.	14.	.96	23.4
CL - AT + BT ² + CT		6.	12.	6.	8.	3.	14.	14.	.99	58.4

points equally. Because of the uncertainty on the total cross section it was felt that a shape comparison using a scale factor to minimize the χ^2 between the extrapolated on-shell cross section and experimental on-shell cross section would be most revealing. The factor listed is the ratio of the actual scale factor to the known experimental correction factor given in Chapter IX. If this number deviates from 1 by no more than the 6% cross section error, the fit results should be regarded as valid as they stand. Only two sets of extrapolation curves have factors outside this 6% error; the B.D. -at and the C.L. -at fits. would indicate that the linear extrapolation is not good even for the Benecke Durr model. This table indicates that the D.P. -at + bt² and the B.D. -at + bt² fit types are the best. Not only are their multiplicative scale factors almost one, but their χ^2 are smallest for the extrapolated on-shell cross section values. Figure 10.4a-f shows the extrapolated on-shell values obtained from extending the fitted curves to $t = u^2$ plotted as error bars. The curve is the on-shell data. Again one can see the excellent agreement between the B.D. at + bt² and D.P. at + bt² extrapolation results and the on-shell cross section.

One can use the models to predict the off-shell scattering when the on-shell results are known. Figure 10.5a-d show the Dürr Pilkuhn curves (solid lines) with the off-shell data (error bars). The four distributions a-d

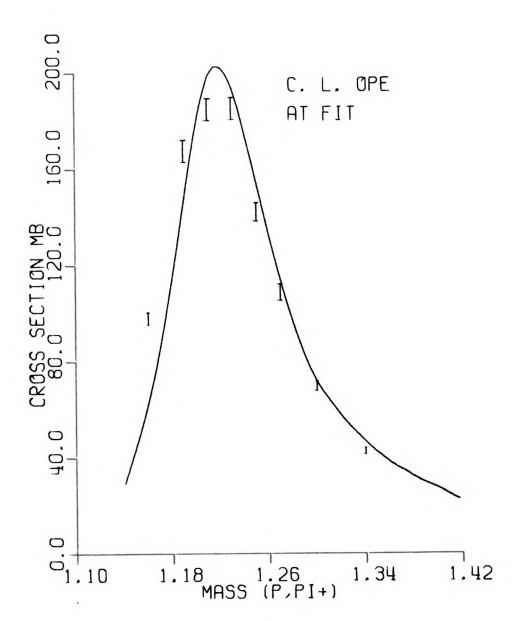
are the mass of the P- π + system, the momentum transfer squared and the Δ ++ decay angles θ_{Jac} and ϕ_{TY} respectively.

The experimental mass and t curves are reproduced fairly well by the off-shell t dependence given by the Dürr-Pilkuhn form factor model. The Dürr Pilkuhn OPE curves shown in Figures 10.5c-d do not follow the data points. Form factor models which modify the individual helicity amplitudes and density matrix elements can also be used to predict the decay angular distributions. 44-46 The absorbtion model, 47 for example, gives predictions which are in good agreement with experiment. 46

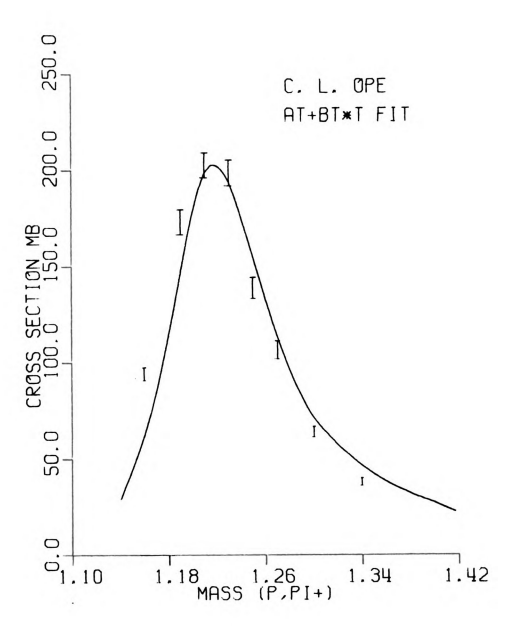
The three polynomial extrapolations terms used above all require explicitely that the "to" curve is zero at t=0. Several schemes have been proposed to account for the possible deviation of the O.P.E. differential cross section from 0 at t=0. It has been proposed that conspiracy could occur between the pion Regge pole and an opposite parity pole. The idea is that in reactions between particles with spins, kinematic constraints require certain helicity amplitudes to vanish at t=0. For a single Regge pole in that t channel, these constraints force some amplitudes to vanish when they are factorized. Conspiracy is when a set of Regge poles conspire to satisfy the constraints collectively instead of each being zero. Conspiracy can give effects similar to damping corrections in absorption models.

- Figure 10.4. a-b. Chew Low extrapolated on-shell mass cross section and on-shell data.
 - c-d. Dürr Pilkuhn extrapolated and on-shell mass data.
 - e-f. Benecke Dürr extrapolated and onshell mass data.

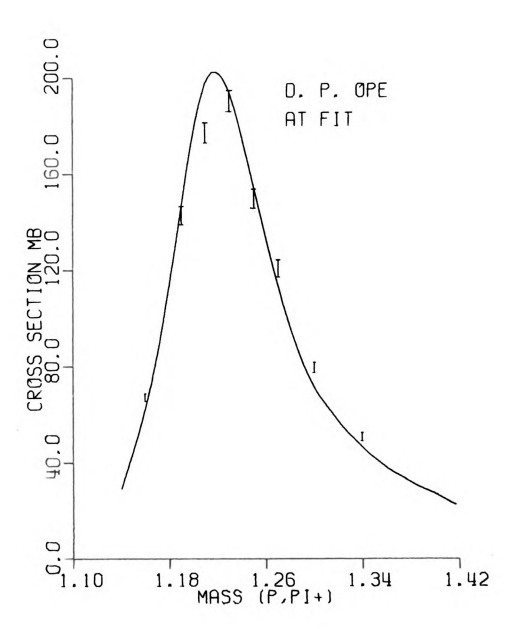
(a)



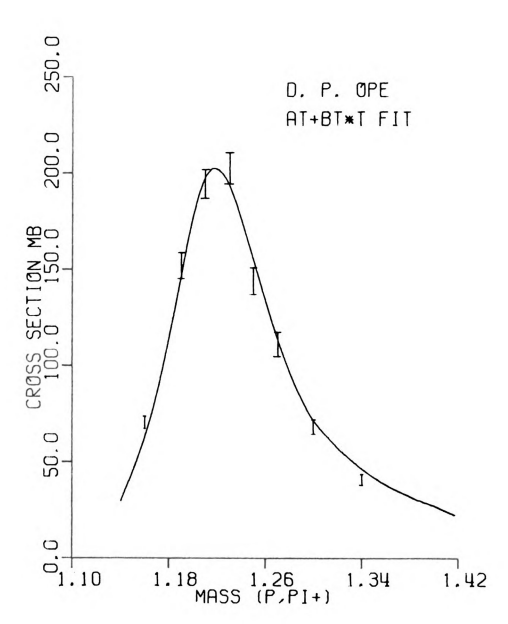
(b)



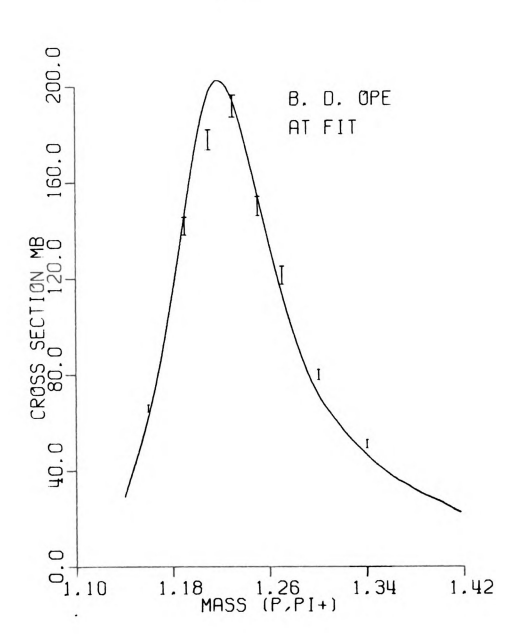
(c)



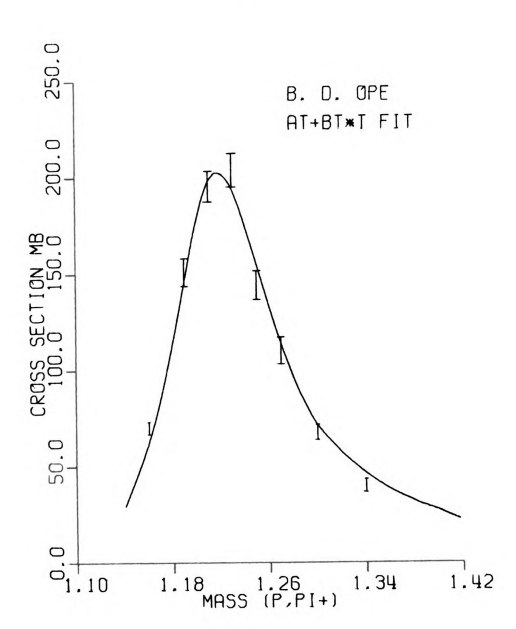
(d)

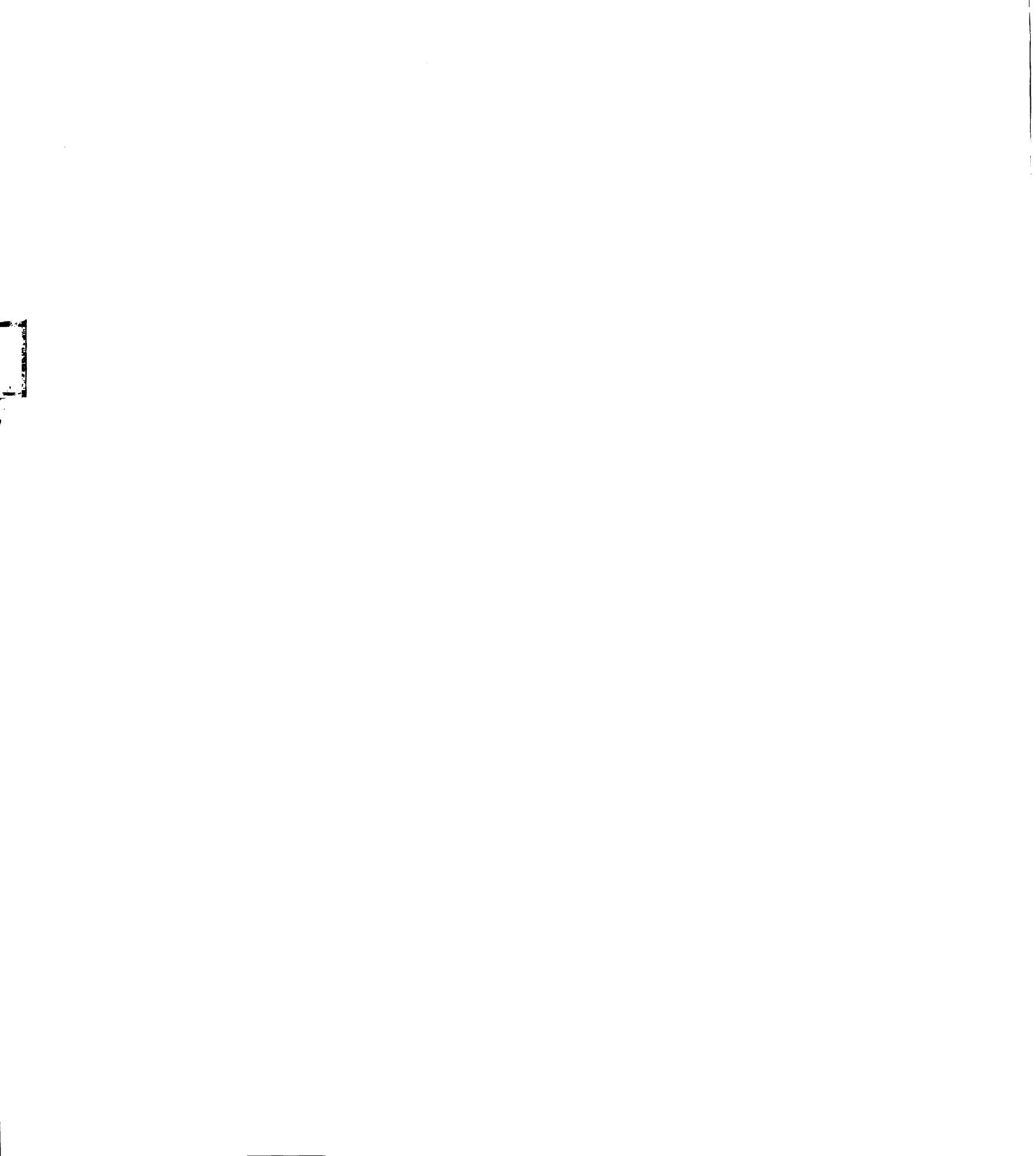


(e)

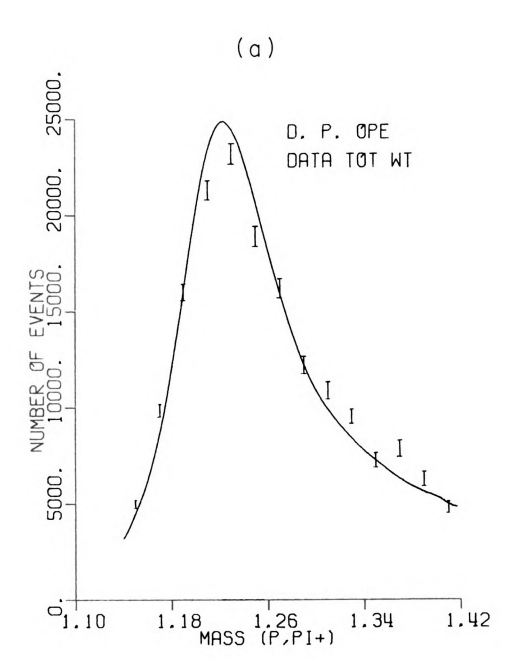


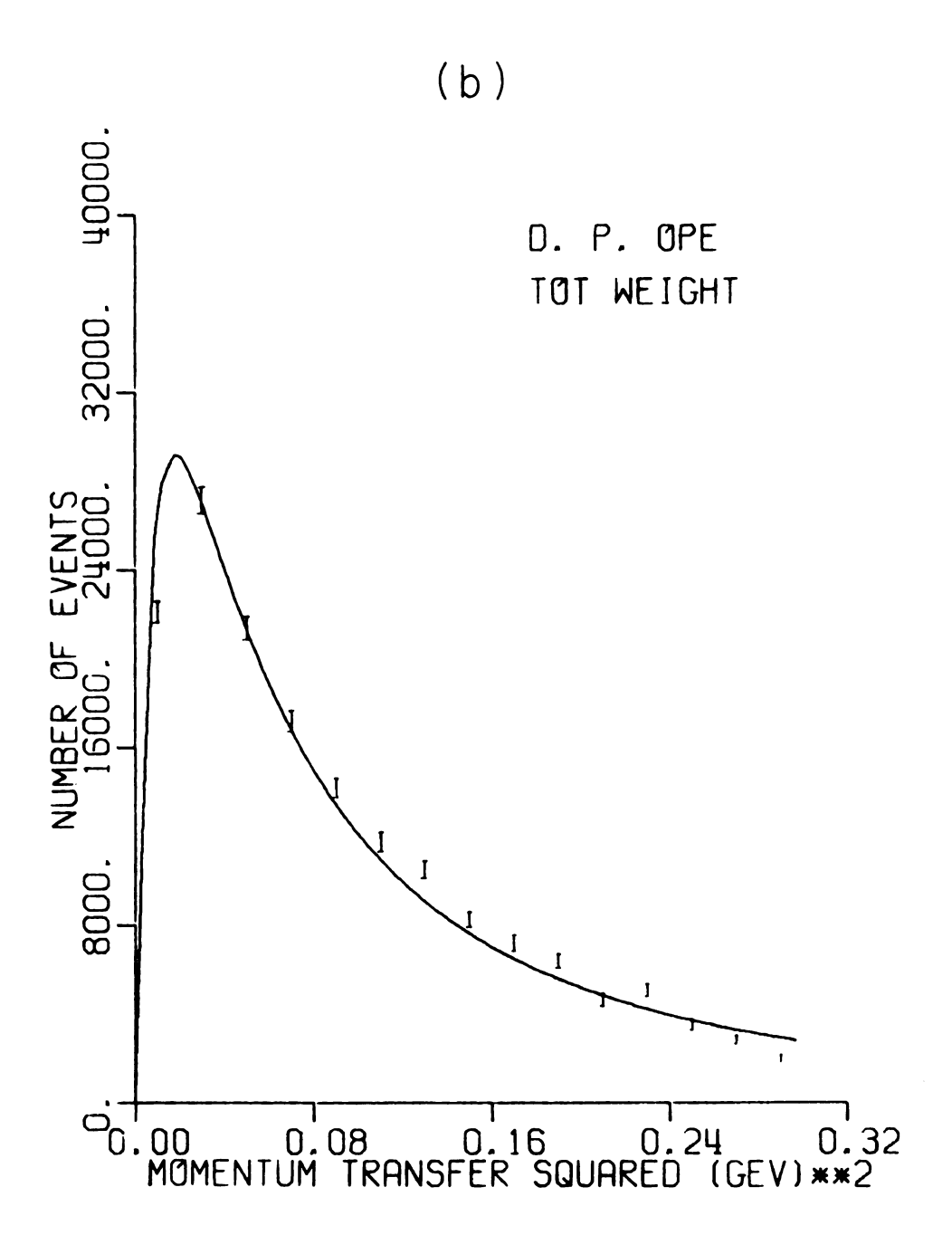
(f)

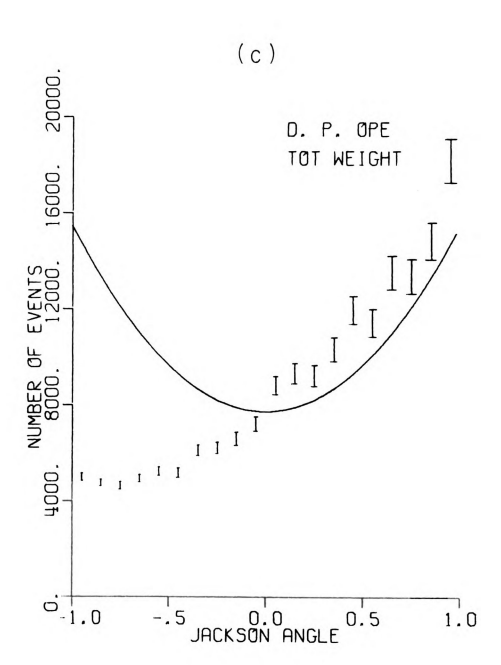


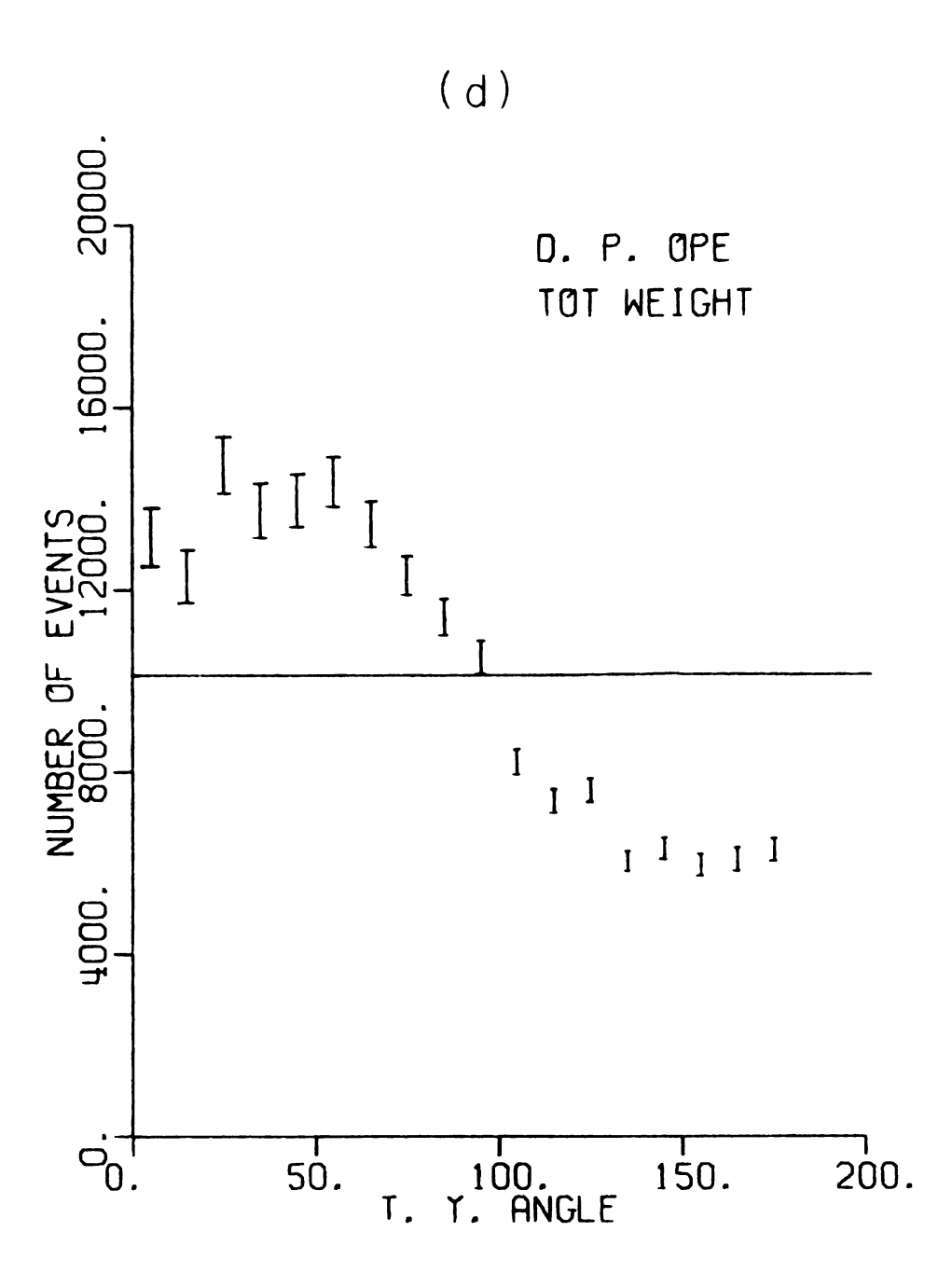


- Figure 10.5. a. do/dM experiment and Dürr Pilkuhn prediction.
 - b. do/dt experiment and Dürr Pilkuhn prediction.
 - c. $d\sigma/d\cos\theta_{\mbox{\scriptsize Jac}}$ experiment and Dürr Pilkuhn prediction.
 - d. $d^{\sigma}/d\varphi_{TY}$ experiment and Dürr Pilkuhn prediction.









It is found useful to eliminate the t in the numerator which arises naturally in the limit $t + \mu^2$ in the Double-Regge-Pole model (D.R.P.). The diagram is shown in Figure 10.6. One can define $S = (P_1 + P_2)^2$ and

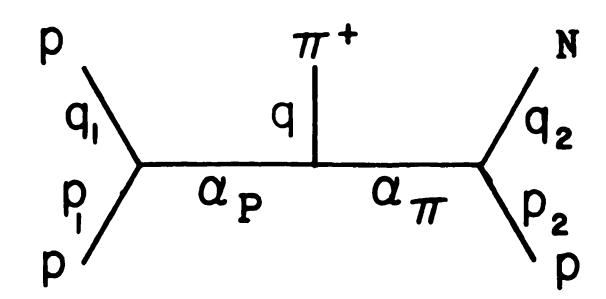


Figure 10.6. Double-Regge-Pole Model.

S p π + = $(q_1 + q_1)^2$. The application of the D.R.P. model assumes an explicate 3 body final state so quasi-two-body states should be removed. It is necessary to have $\sqrt{\text{Sp}\pi}$ + = $M(P\pi+)^2 \cdot 2.0$ GeV. One obtains good results by allowing $t \rightarrow \mu^2 \cdot 49$ Even if one extends the analysis to low $M(P\pi+)$, 22 one can still get reasonable fits using appropriate modifications of the t factor from O.P.E. Reggeized pion exchange give good results to decay curves for the P- π + when the t factor is modified as described above. 44

The modifications necessary to have do/dt not pass through 0 at t = 0 arise naturally from an absorption model. 45, 46 A general absorption model has been worked out. 47 This model considers several spin states and applies absorbtive corrections on the angular momentum decomposition of the individual Born term helicity amplitudes in the standard S-channel helicity frame.

The absorption can be represented for the helicity flip term as

$$\frac{-t}{t-M_{\pi}^{2}} \xrightarrow{\text{absorbtion}} \frac{-M_{\pi}^{2}}{t-M_{\pi}^{2}} A(s,t) + B(s,t)$$

and the non-flip term is

$$\frac{(-t)^{\frac{1}{2}\ln l}}{t-M_{\pi}^{2}} \xrightarrow{absorbtion} \frac{(-t)^{\frac{1}{2}\ln l}}{t-M_{\pi}^{2}} ((s,t) \text{ where}$$

n is the net helicity flip. This model provides a good approximation to the decay distribution of the $\Delta + + in$ PP+N $\Delta + + \cdot \cdot ^{46}$ A simpler absorption model has been used to extrapolate in t and obtain the on-shell $\pi - \pi$ density matrix elements. 8, 50 The absorption corrections can be used to account for the descrepancy between the data and O.P.E. model curves.

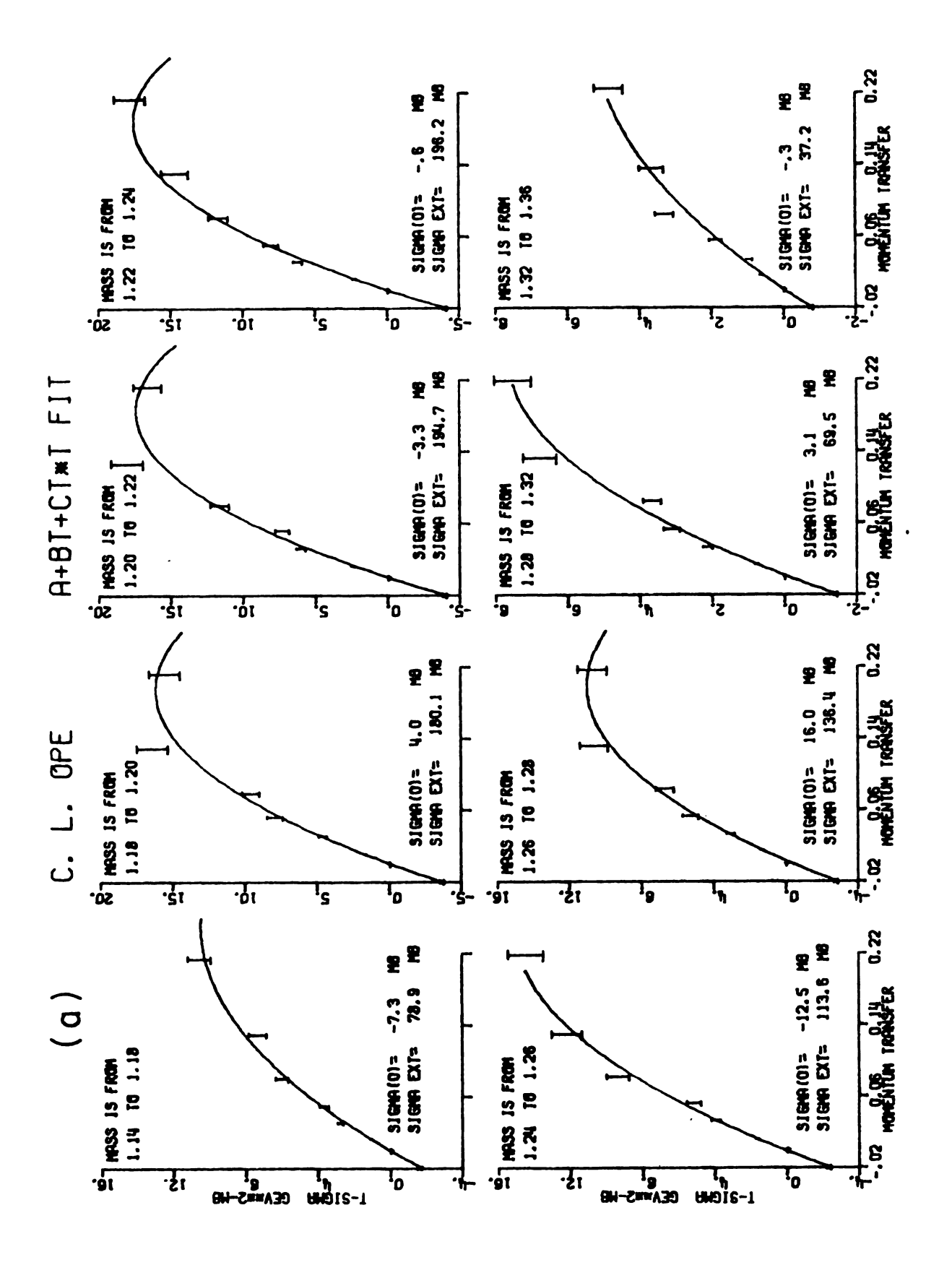
As mentioned above, many models can account for $d\sigma/dt \neq 0$ at t=0. The absorption model predictions agree fairly well with experiments at lower energies. Figure 10.7a-c shows the extrapolation curves for "to" for the Chew Low, Dürr Pilkuhn, and Benecke Dürr models with a fit parameterization of the a + bt + ct² type.

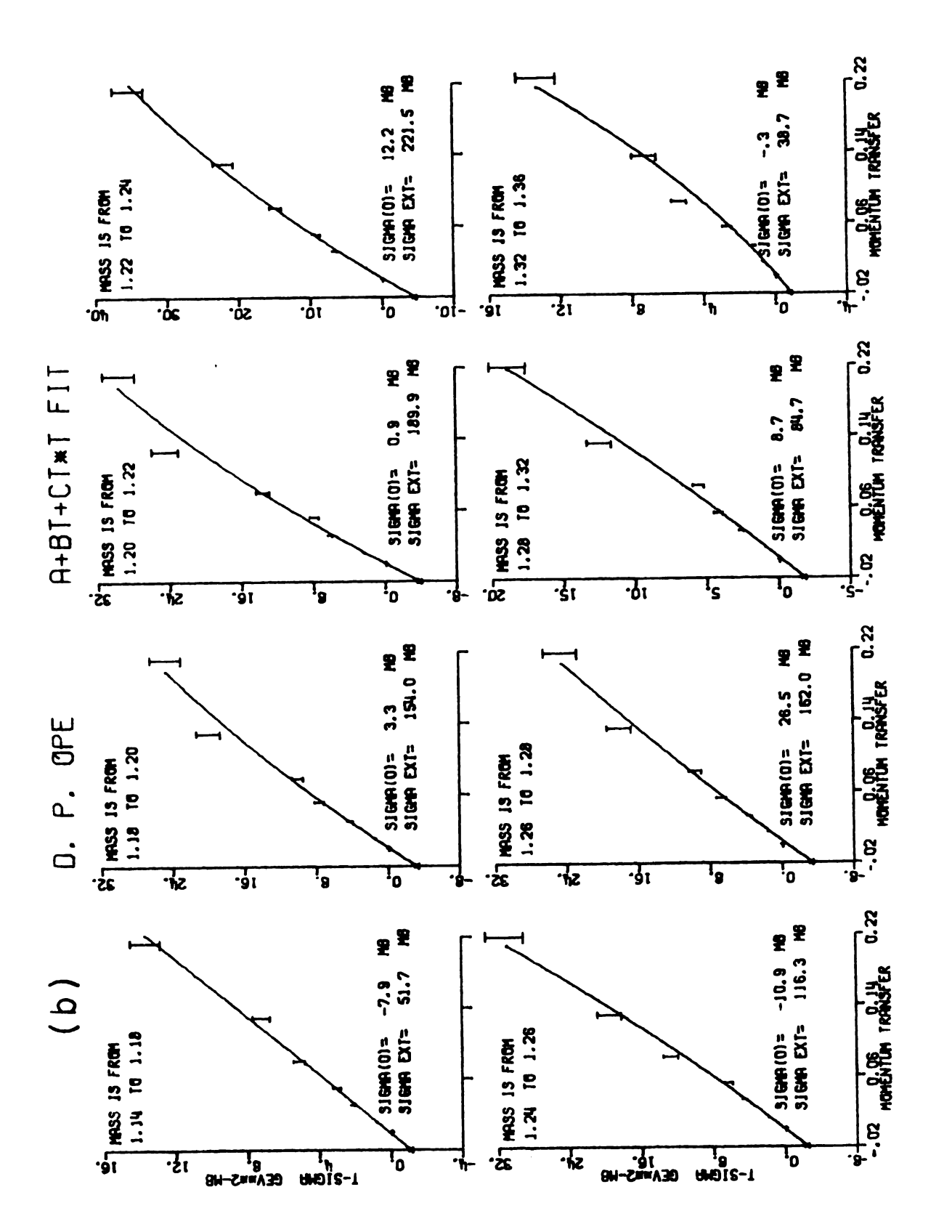
The + sign in the lower left hand corner indicates the position of the origin $(t,"t\sigma") = (0,0)$. The results of these fits are summarized in Table 10.2 along with results from a linear fit. It is clear that the linear fits not constrained to pass through the origin do not reproduce the on-shell values with a good χ^2 . Also the

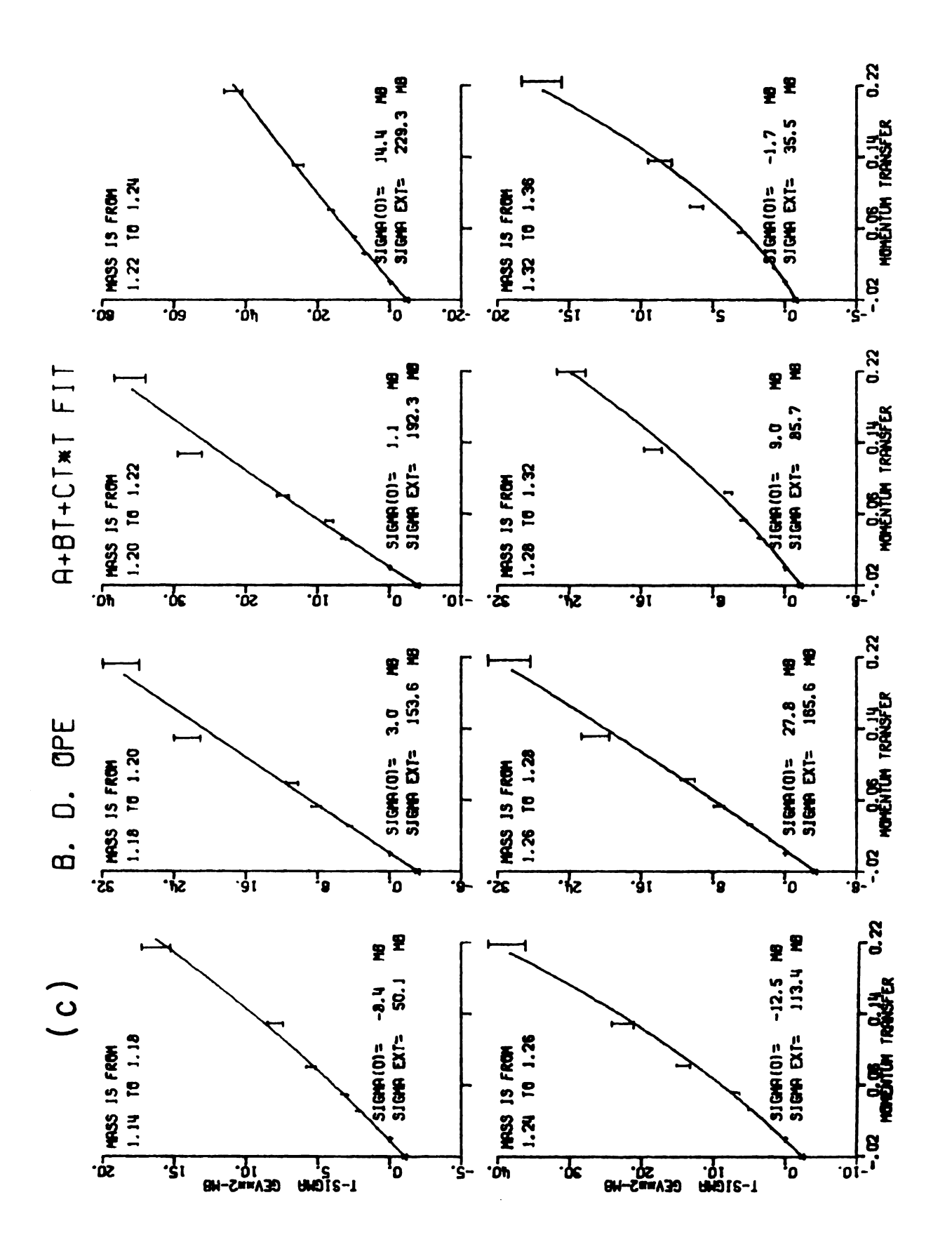
C.L. model with a + bt + ct² extrapolation polynomials. ٠ ت Figure 10.7.

D.P. model with a + bt + ct² extrapolation polynomials. ф.

B.D. model with a + bt + ct^2 extrapolation polynomials. ς.







scale factors are not in good agreement with 1, with the exception of the Durr Pilkuhn model. The Chew-Low model requires the data to be scaled up by a factor of 4.

Table 10.2.--Chi-Square and Multiplier for A + BT and $A + BT + CT^2$ Fits.

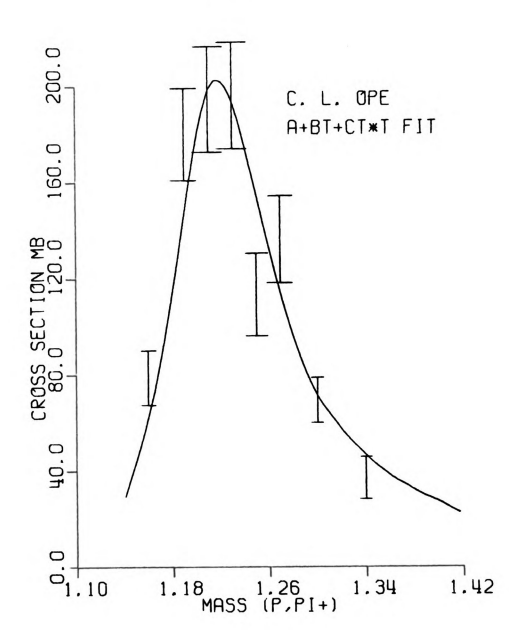
Fit Type	1	2	3	4	5	6	7	8	Fac	χ²
DP - A + BT	5.	11.	21.	9.	9.	5.	14.	23.	.96	57.
BD - A + BT	7.	8.	16.	5.	14.	5.	19.	31.	1.18	67.
CL - A + BT	30.	64.	88.	74.	33.	42.	41.	25.	.26	20.
DP - A + BT + CT ²	5.	8.	15.	4.	7.	4.	13.	17.	1.034	10.5
BD - A + BT + CT ²	5.	8.	16.	4.	7.	4.	13.	16.	1.03	10.8
CL - A + BT + CT ²	5.	7.	12.	7.	6.	3.	14.	15.	1.005	13.6

In all three models if one allows the parabolic fit for the extrapolation, a good χ^2 is achieved and the scale factors are consistant with one within the limits of the cross section error.

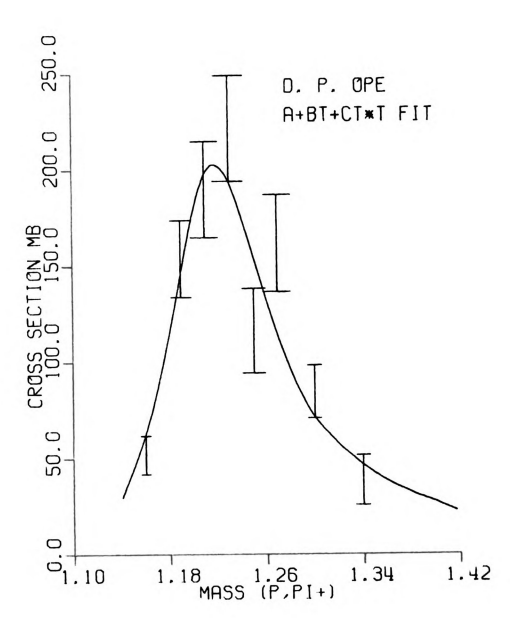
Figure 10.8a-c shows the extrapolated on-shell cross sections as error bars using quadratic extrapolation curves not constrained to pass through the origin. The error bars are larger than those shown in Figure 10.4 because both ends of the extrapolation curve are free to move. The smaller errors in Figure 10.4 are obtained because the fit curve was constrained to pivot around the

- Figure 10.8. a. C.L. extrapolated cross section at $t = M\pi^2$ and on-shell curve for $a + bt + ct^2$ extrapolation curve.
 - b. D.P. extrapolated cross section using same criteria as above.
 - c. B.D. extrapolated cross section using same criteria as above.

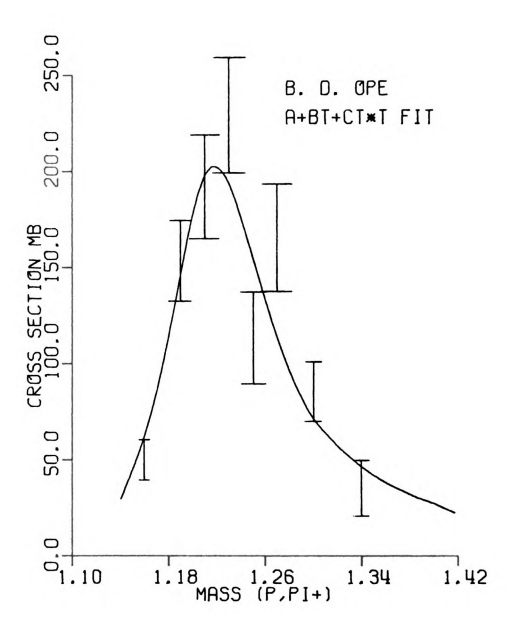








(c)

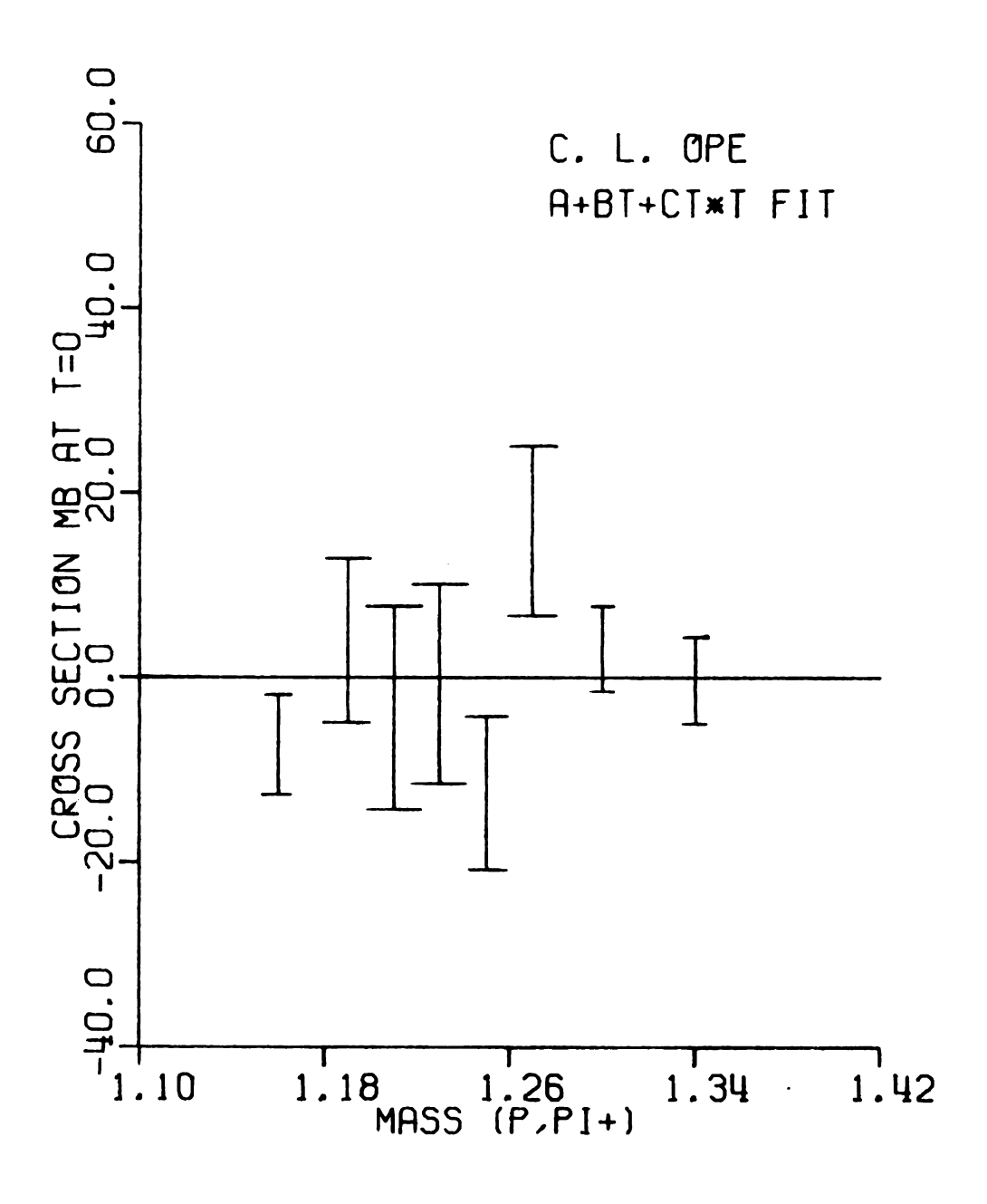


origin. The freedom of the extrapolated value was severaly restricted because the origin is close to the pion mass squared. The solid curve is the experimental on-shell cross section. Figure 10.9a-c is the extrapolation cross sections evaluated at t = 0 for the three models. The O.P.E. with form factors would predict zero because the spin amplitude must go to zero in the forward direction. The quadratic fit extrapolated to t = 0 gives a cross section that is free from increasing or decreasing trends and is in general consistant with zero. However, even the absorption model predicts this cross section to differ only slightly from zero at these energies. 51

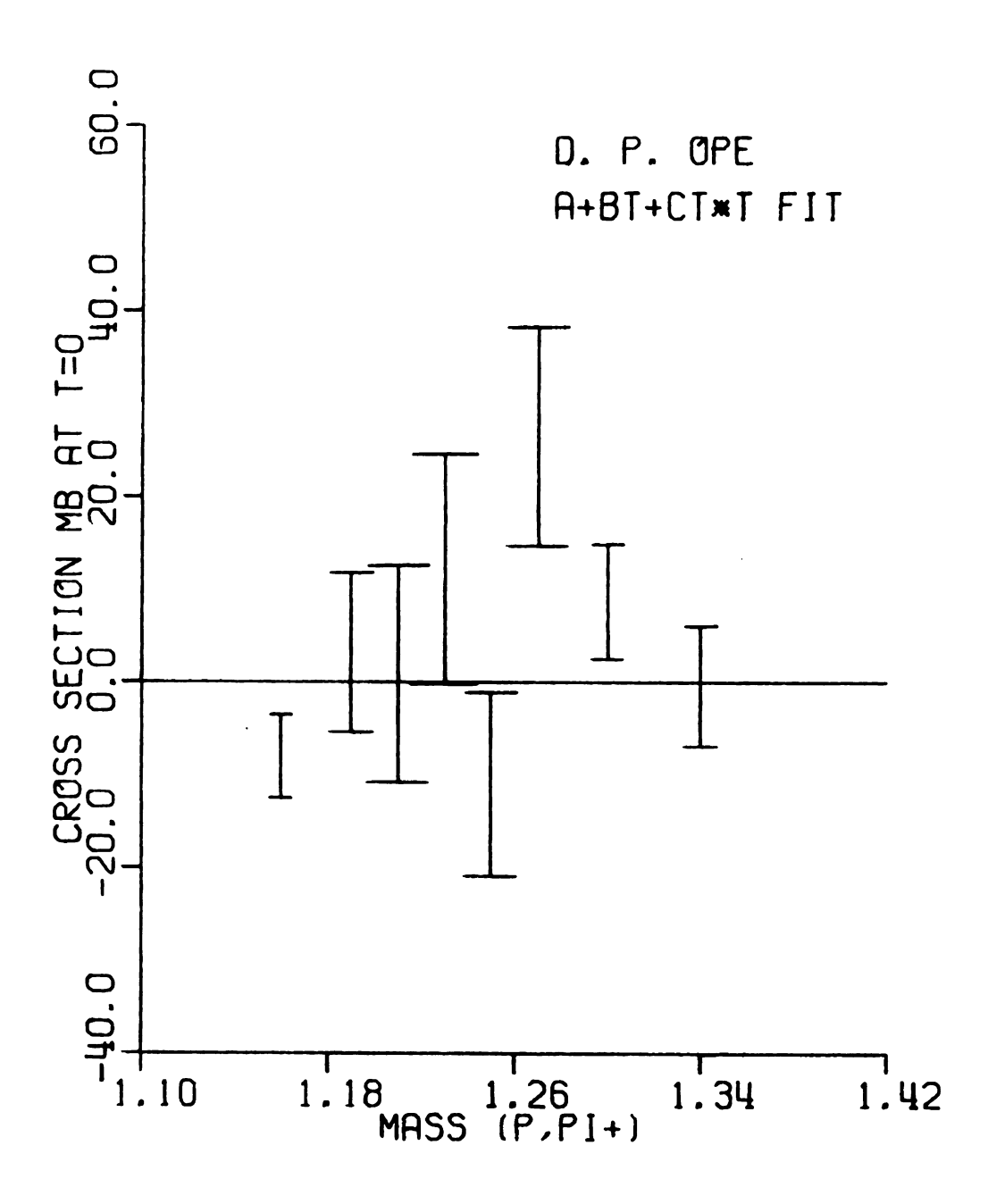
- Figure 10.9. a. C.L. extrapolated cross section at t=0 for a + bt + ct² extrapolation curve.

 The straight line at $\sigma(t=0)=0$ is the unmodified O.P.E. prediction.
 - b. D.P. extrapolated cross section at t = 0 using same criteria as above.
 - c. B.D. extrapolated cross section at t = 0
 using same criteria as above.

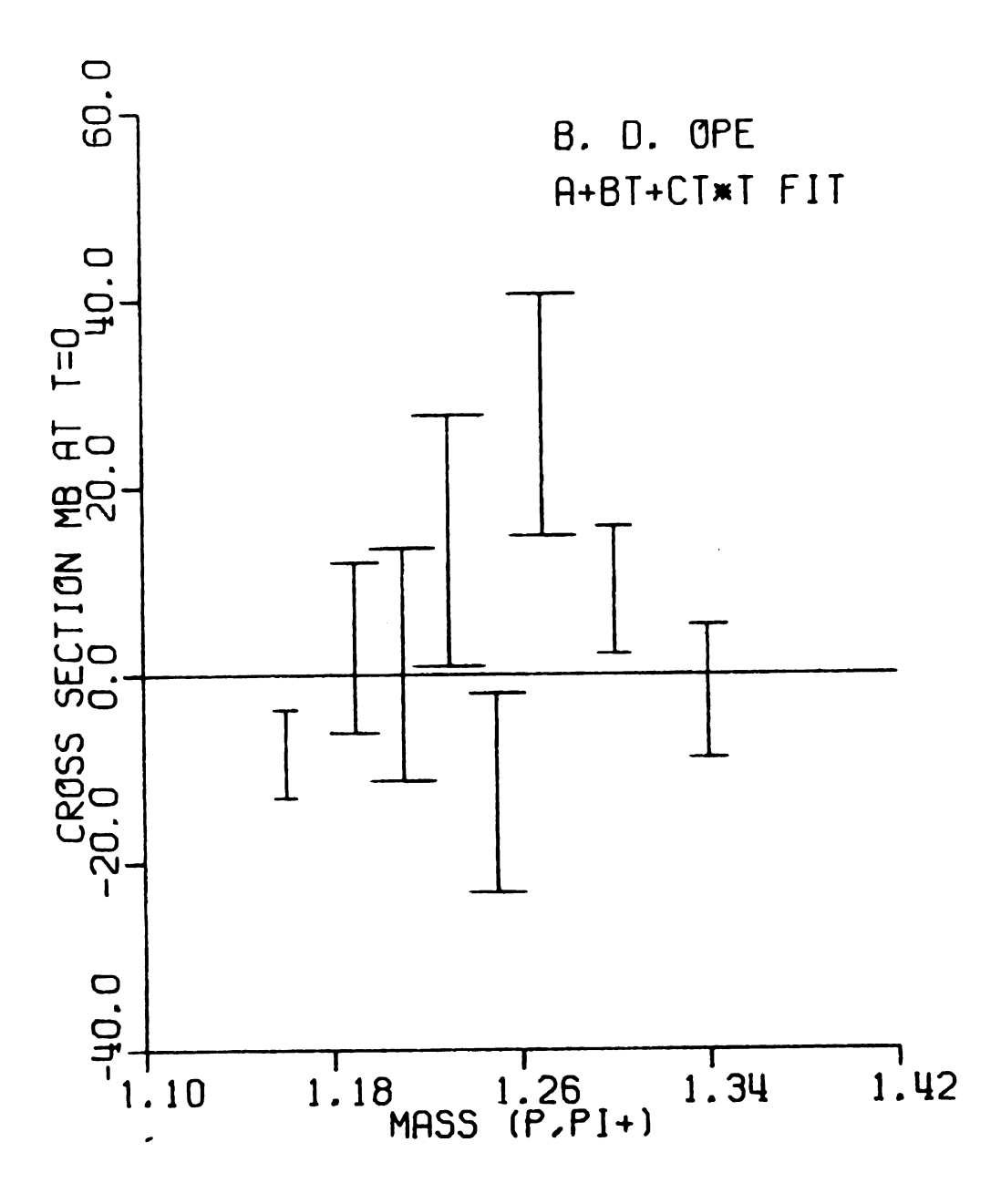
(a)



(b)



(c)



CHAPTER XI

SUMMARY AND CONCLUSIONS

This thesis reports on the analysis of one pion production reactions resulting from proton-proton scattering at 6.0 Gev/c. The final data sample includes 40,000 events with the PN π + final state and 10,000 events with the PP π ° final state. The PN π + sample includes 14,000 events having the Δ ++ $_{1236}$ (3,3) resonance-neutron final state. This resonance is defined by restricting 1.14<M $_{P\pi}$ +<1.42 Gev and simultaneously demanding that the target proton-neutron momentum transfer be less than 0.3 Gev 2 .

The PN π + sample has a neutron width of 186 MeV and the PP π ° has a pion width of 165 MeV. The mass resolution for the P π + is 5 MeV in the peak and the momentum transfer per cent resolution is 2%, except at small t. The cross section for PP+PN π + at 6 GeV/c is estimated to be σ (PN π +) = 7.58±0.7 mb.

The 14,000 Δ ++ events were corrected for their limited acceptance in the spectrometer. A Monte Carlo program was written to correct for hardware-induced

scattering and various hardware efficiency losses. The $\Delta++$ sample has a corrected F.W.H.M. of 126 \pm 4 Mev. The cross section for PP+ $\Delta++$ N is obtained using a Breit-Wigner fit to the mass distribution and gives $\sigma(PP+\Delta++N) = 2.702 \pm 0.15$ mb.

The one pion exchange model was used to interpret the final data with the $\Delta ++$ neutron final state. The exchange diagram for this process is shown in Figure 11.1.

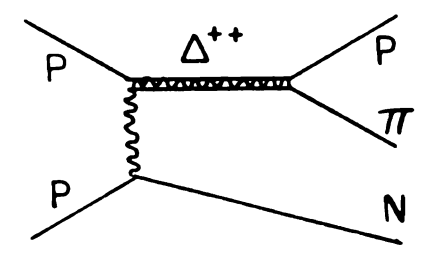


Figure 11.1. One pion exchange diagram for PP+ Δ ++N.

The upper vertex in the figure was interpreted in this experiment as π -P elastic scattering, where initially the pion is off its mass shell, or virtual, and is a real pion after the resonance decays. A pole extrapolation was carried out for different mass bins using the scattering data. The quantity $t\sigma_{\text{on-shell}}(M)$ was calculated using off-shell negative t value bins of the data, and the data points thus obtained were fit and extrapolated as a function of t to the positive unphysical t region. The extrapolated value at the pion mass squared was compared to the known on-shell cross sections. 7

At a fixed mass, the actual scattering data are complicated as a function of t. The extrapolation of t to

positive values can be done reliable only if the data are normalized using the expected pole cross section and off-shell corrections. The pole term contains vertex factors from the upper and lower vertex in Figure 11.1 and a contribution from the pion propagator. The off-shell corrections are due to spin effects of the $\Delta++(3,3)$ resonance formation and dynamical form factors which result from the finite spacial extension of the particles involved in this process.

Three models are compared in this thesis. Chew-Low (C.L.) model is an unmodified one pion exchange model without form factors. The Dürr-Pilkuhn (D.P.) model 12 and the Benecke-Dürr (B.D.) model 13 introduce dynamical form factors which consider the nucleon and $\Delta++$ as having a finite extension in space. The form factors damp out high t or low partial waves in the cross section. The difficiences of each model can be readily seen from the linear bt fits to the calculted "to" values presented in Chapter X. If the theory had the correct off-shell t dependence, the "to" points calculated using the off-shell data normalized by the theoretically calculated values should be a straight line with the slope parameter $b = \sigma_{ON}(M)$. The Chew-Low "to" points are seen to be fit poorly by a linear curve. As is well known, the calculated cross section is too high at higher t values. The Dürr-Pilkuhn and Benecke-Dürr normalized points are nearly linear, but some deviation from linearity is evident at high t. The linear plots indicate that the calculated cross section is under damped at high t below the mass peak and over damped at high t above the mass peak.

The pole extrapolation values of the on-shell cross section as a function of mass is presented for linear, quadratic and cubic curves fit to the normalized off-shell data points. The non-linear fits are used to obtain good fits throughout the t range and are used because none of the three models assumed here fit the data exactly, as was shown above. The quadratic curve fits to data normalized by the Dürr-Pilkuhn or Benecke-Dürr model have been extrapolated to the pion pole and the cross section results are in good agreement with the experimental on-shell values. No normalization factors are necessary to obtain this good agreement.

The one pion exchange model demands that the cross section as a function of t pass through 0 at t=0. This is because the pseudo-scalar pion exchange vertex contribution from the lower vertex in Figure 11.1 is non-zero only for the spin flip amplitude. This spin flip amplitude goes to 0 at t=0. Regge pole models with conspiracy 48 or absorption models 45 do not require the cross section to be zero at t=0.

The scattering data has been extrapolated to t=0 in this analysis. Again, the normalization factors are

calculated using the Chew-Low, Dürr-Pilkuhn, and Benecke-Dürr models. The data normalized by the Dürr-Pilkuhn and Benecke-Dürr model calculations give good fits using quadratic curves of the A + Bt + Ct 2 form. The extrapolated cross sections at t = 0 are consistant with zero. At this energy and with the statistics of this experiment, one cannot differentiate between the absorption model and the form factor models predictions at t = 0. 51

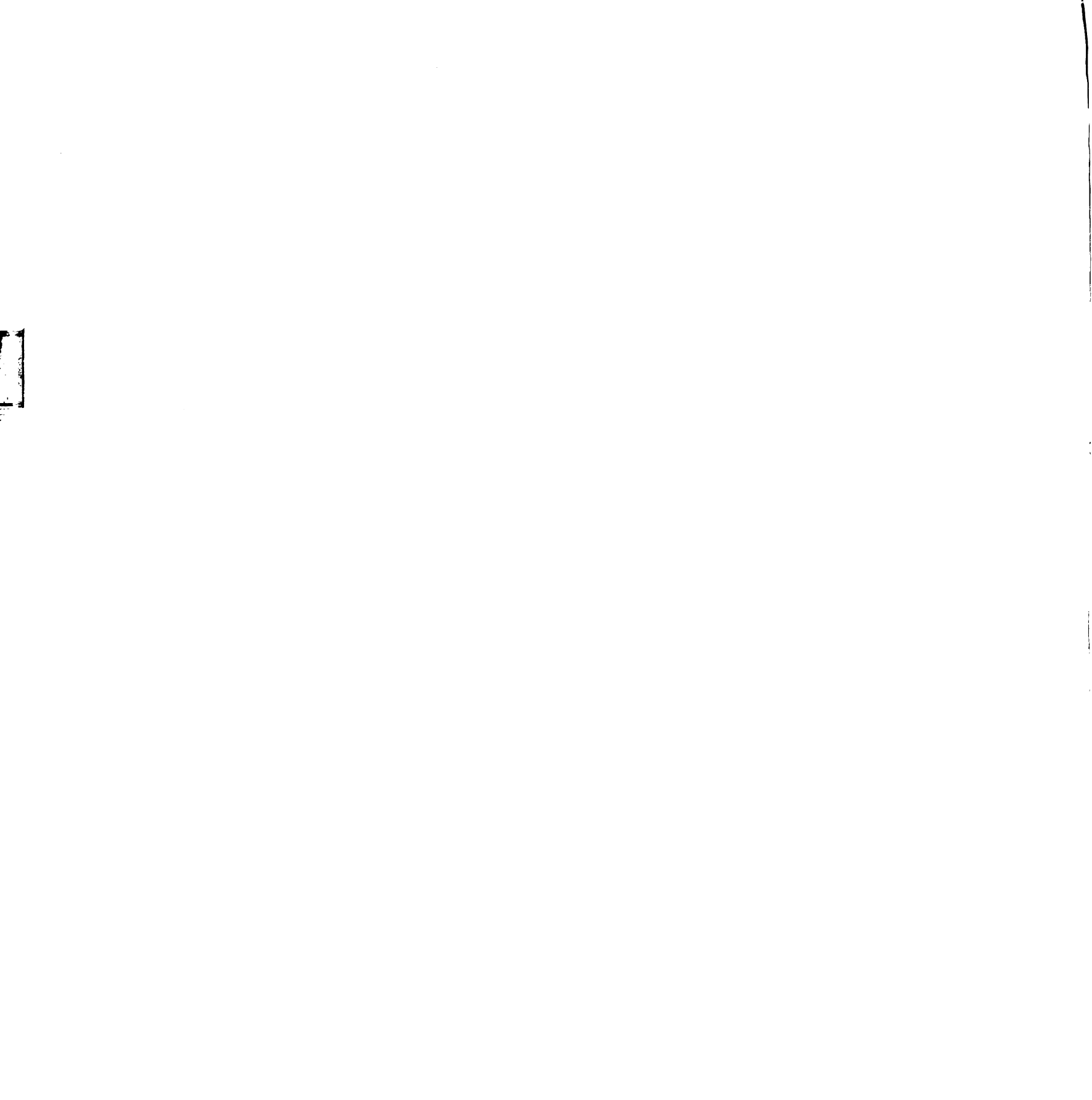
REFERENCES

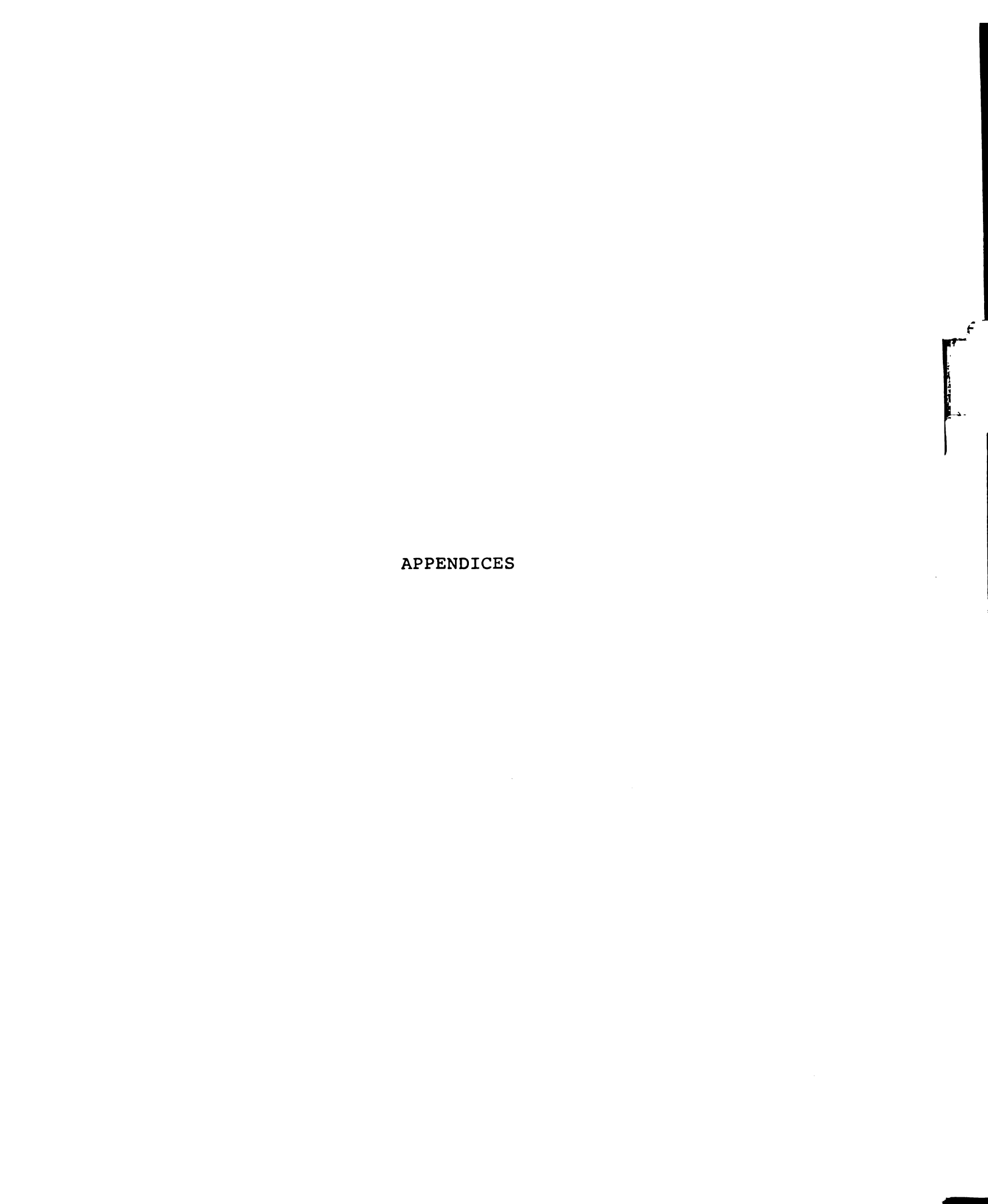
REFERENCES

- 1. G. F. Chew and F. E. Low, Phys. Rev. 113, 1640 (1959).
- 2. W. S. C. Williams, An Introduction to Elementary Particles, Academic Press, 1971.
- 3. Günter Wolf, Phys. Rev. 182, 1538 (1969).
- 4. Z. Ming Ma et al., Phys. Rev. Lett. 23, 342 (1970).
- 5. Particle Data Group, NN and ND Interactions, Lawrence Radiation Laboratory, 1970.
- 6. E. Flaminio, et al., Compilation of Cross Sections IV π + Induced Reactions. CERN (1970).
- 7. A. A. Carter, et al., Nucl. Phys. 26B, 445 (1971).
- 8. P. K. Williams, Phys. Rev. Dl, 1312 (1970).
- 9. J. P. Prukop, Low Energy $\pi\pi$ Phase Shifts from the Reaction π -P+ π - π +N at 5 Gev/c, University of Notre Dame (thesis), 1973.
- 10. References given in 6 include differential cross sections.
- 11. J. D. Jackson and H. Pilkuhn, Nuovo Cimento. 33, 906 (1964).
- 12. H. P. Dürr and H. Pilkuhn, Nuovo Cimento. 40A, 899 (1965).
- 13. J. Benecke and H. P. Dürr, Nuovo Cimento. <u>56A</u>, 269 (1968).
- 14. Crunch is a filter program written by J. Prukop, University of Notre Dame (thesis).

- 15. D. E. Fries, Circe--A general multi-prong fitting computer program for spacial coordinates in a non-uniform magnetic field. S.L.A.C. -99, UC-34, 1967.
- 16. D. E. C. Fries, Nuclear Inst. & Methods. 44, 317 (1966).
- 17. R. J. Sprafka, Michigan State University, did most of the work necessary to specialize the software of this experiment.
- 18. I. Dorado and R. Leedy, S.L.A.C. 72, UC 34 (1967).
- 19. H. A. Bethe, Phys. Rev. 89, 1256 (1953).
- 20. E. Segre, Exper. Nucl. Phys., Wiley, V1, 287 (1953).
- 21. L. Marten, Methods of Exper. Phys., Academic Press, 73 (1961).
- 22. E. Colton, et al., Phys. Rev. 7, 3267 (1973).
- 23. L. Leśniak and H. Wolek, Nucl. Phys. 125A, 665 (1969).
- 24. H. Palovsky, et al., Phys. Rev. Lett. 118, 1200 (1967).
- 25. W. Preston, et al., Phys. Rev. <u>118</u>, 579 (1960).
- 26. C. Wilkin, Nucl. & Par. Phys., W. A. Benjamin. 439 (1968).
- 27. J. W. Cronin, et al., Phys. Rev. 107, 1121 (1957).
- 28. V. S. Barashoakov, et al., Fort. der Phys. <u>17</u>, 683 (1969).
- 29. S. M. Eliseev, ACTA Phys. Pol. Bl, 83 (1970).
- 30. John C. Caris, et al., Phys. Rev. 126, 295 (1962).
- 31. G. Bellettini, et al., Nucl. Phys. 79, 609 (1966).
- 32. This program was written by Dr. D. L. Parker. Michigan State University.
- 33. L. Landau, Jour. of Phys. 8, 201 (1944).
- 34. B. Rossi, High Energy Particles, Prentice-Hall, Inc. (1952).

- 35. Y. K. Akimov, Scintillation Counters in High Energy Physics, Academic Press (1965).
- 36. Z. Ming Ma and E. Colton, Phys. Rev. Lett. <u>26</u>, 333 (1971).
- 37. R. J. Eden, High Energy Collisions of Elementary
 Particles. Cambridge Press. Chapter 3 (1967).
- 38. Jon Pumplin, private communication, Michigan State University.
- 39. J. D. Jackson, Nuovo Cimento. 34, 1644 (1964).
- 40. M. Jacob and G. Chew, Strong Interaction Physics. Chapter 1. W. A. Benjamin Inc. (1964).
- 41. E. Colton, Thesis, Pion Production in Proton-Proton
 Interactions at 6.6 Gev/c. Appendix A, University of California (1968).
- 42. J. Blatt and V. Weisskopf. Theoretical Nuclear Physics. Wiley, 358 (1952).
- 43. George Bohannon, private communication. Michigan State University.
- 44. P. Kobe, et al., Nucl. Phys. <u>52B</u>, 109 (1973).
- 45. G. L. Kane, Phys. Rev. Lett. 25, 1519 (1970).
- 46. V. Blobel, et al., Nucl. Phys. B. To be published.
- 47. F. Wagner, Nucl. Phys. <u>58B</u>, 494 (1973).
- 48. R. J. N. Phillips, Nucl. Phys. 2B, 394 (1967).
- 49. E. L. Berger, Phys. Rev. Lett. 21, 701 (1968).
- 50. P. K. Williams, AIP Conference. Proceedings on Experimental Meson Spectroscopy (1972).
- 51. S. Hagopian, et al., Phys. Rev. <u>D7</u>, 1271 (1973).
- 52. B. Y. Oh, Michigan State University, wrote the notes from which this fitting technique was adapted.





APPENDIX A

EVENT PROCESSING FAILURES

APPENDIX A

EVENT PROCESSING FAILURES

Table A.1 lists the cause and percentage of Crunch failure events.

Table A.1.--Crunch Losses.

Failure Code	Reason for Failure	Percent of Input Ev.			
1	Less than 2 Y tracks downstream	26%			
3	Less than 2 Z tracks downstream	7.5%			
8	<pre>Vertex too far from target; <2 useful</pre>	6.2%			
10	No potential U-V or Y-Z pair after magnet	6.2%			
15	No Y-Z or U-V pairs after 1 track removed	3.6%			
30	Event has same Y or Z view in chamber 7 and 8	27%			
		Total = 76.5%			

The other 6.5% of losses are distributed among the other failures codes, but can be related to the inability of Crunch to find two good tracks. In order for a beam track to fake a good event, it only needs to throw a second particle into the DE/DX, which can occur in a variety of ways, and then also hit two hodoscopes. Occurrences such as "hodoscope splash" or slow electrons after the magnet can cause two hodoscopes to trigger. A study of Crunch loss indicates they are mostly just beam tracks.

The Circe failures are given in Table A.2.

As one can see 90% of the Circe failures have one or two negative tracks. There are many reactions with high cross sections at this energy which would cause these triggers. Table A.3 lists three such reactions.⁵

Teuta failures are multi-pion events and have a low confidence level when forced to fit one of the single pion reactions. Table A.4 summarizes these failures. A study revealed low momentum distributions for tracks 1 and 2 which would be consistant with the phase space production predicted for the multi-pion events as suggested in Table A.5.

Two cuts must be imposed on events which pass Teuta to further limit contamination. First the pass 2 runs which had hardware problems must be eliminated. Also a target cut must be applied to the entire sample. The target cut is taken to be the limits of the physical target plus the half-width of the fitted errors in x and R =

Table A.2.--Circe Failures.

Failure Code	Reason for Failure	Pass 1	Pass 2 Cut
0	× ² increases or needs >8 iterations	5011	58
8	Both tracks negative	3874	27
10	One track positive, other negative	60326	1070
91	>15" from target	1903	18
92	Momentum track 2< 50 Mev	42	0
93	Condition 91 + 92	6	0
94	Momentum track 3<50 Mev	243	6
95	Condition 94 + 91	24	1
96	Condition 94 + 92	3	0
97	Condition 91 + 92 + 94	6	0
99	Varied beam momentum	191	0
Total		71629	1180

Table A.3.--Reactions Leading to 90% of Circe Failures.

Reaction	Cross Section mb		
PP→PPπ+π-	3.3		
$PP \rightarrow PN\pi + \pi + \pi -$	3.1		
$PP \rightarrow PP\pi + \pi - \pi^{\circ}$	2.4		

Table A.4.--Teuta Events Confidence Level <.03.

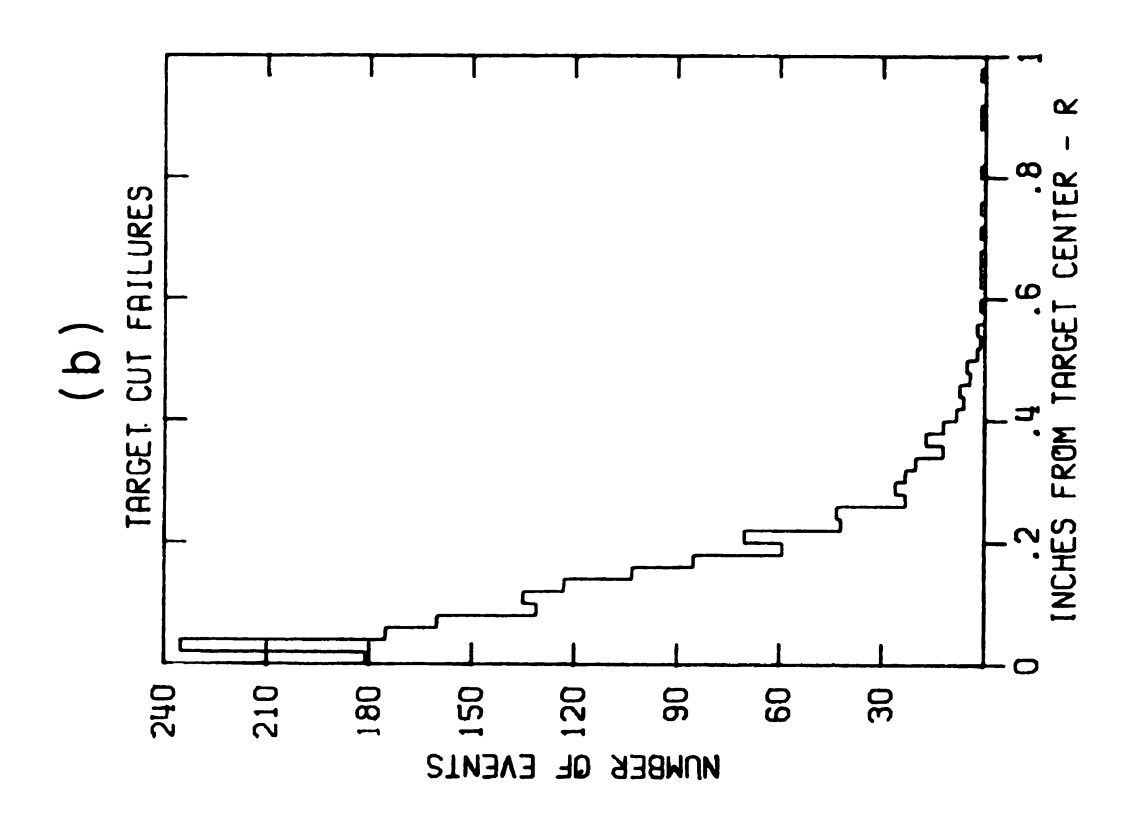
	Positive Field		Negat	ive Field		Total	
	<10 ⁻⁵	10 ⁻⁵ <c<.03< th=""><th><10⁻⁵</th><th>10⁻⁵<c<.03< th=""><th><10⁻⁵</th><th>10⁻⁵<c<.03< th=""><th><.03</th></c<.03<></th></c<.03<></th></c<.03<>	<10 ⁻⁵	10 ⁻⁵ <c<.03< th=""><th><10⁻⁵</th><th>10⁻⁵<c<.03< th=""><th><.03</th></c<.03<></th></c<.03<>	<10 ⁻⁵	10 ⁻⁵ <c<.03< th=""><th><.03</th></c<.03<>	<.03
Pass 1	33703	7411	53465	11242	87168	18653	105821
Pass 2	1606	396	666	197	2272	598	2865

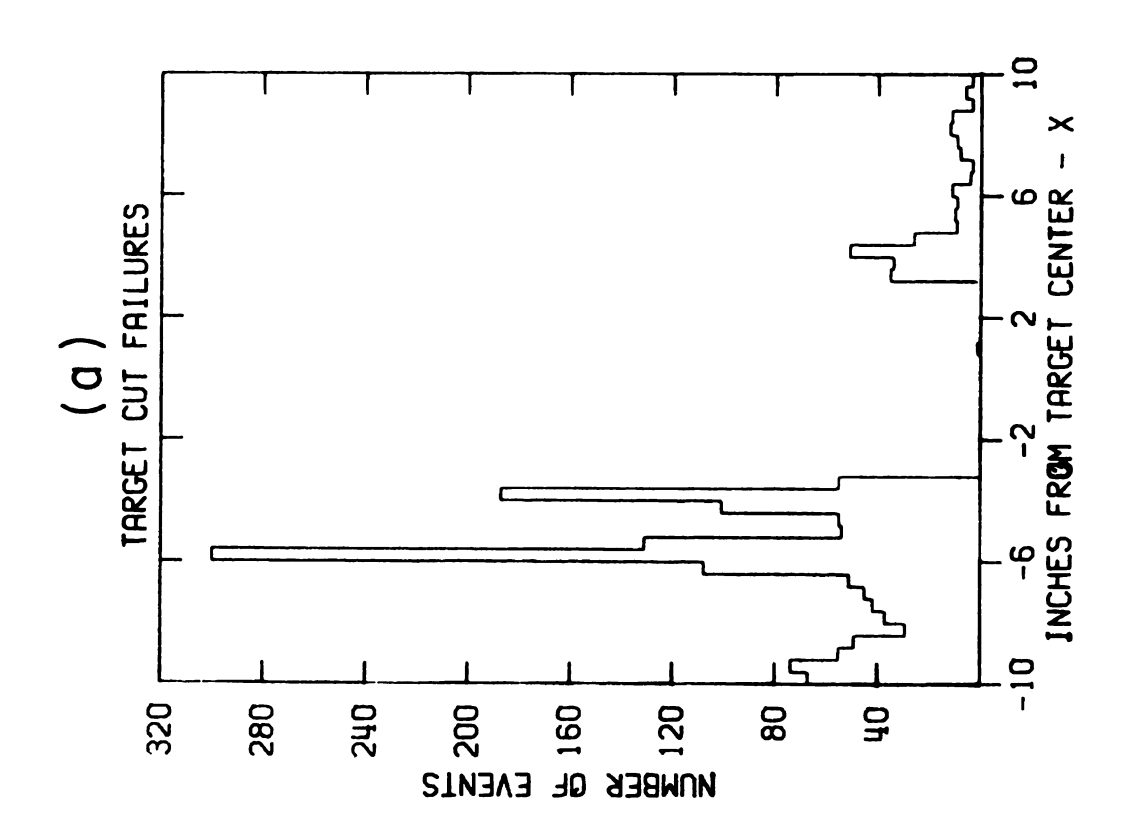
Table A.5.--Teuta Failure Event Types.

Reaction	Cross Section mb
PP→PNπ+π°	~4 mb
$PP\rightarrow NN\pi+\pi+$	~ .5 mb
PP→PPπ°π°	~1 mb
PP→PNπ+π°π°	~2 mb

 $\sqrt{Y^2 + Z^2}$. Figures A.la-b show the event lost to the target cut for x and R respectively. Notice the loss is almost entirely from the x location of the vertex.

Vertex distributions for events lost in the target cut plotted along the beam direction \mathbf{x} , where $\mathbf{x}=0$ is the target center, and \mathbf{R} . Figure A.la-b.





APPENDIX B

BEAM MOMENTUM FITTING PROGRAM

APPENDIX B

BEAM MOMENTUM FITTING PROGRAM⁵²

A typical view from above the experimental apparatus is shown in Figure B.la where the x represents measured spark positions and the line signifies an orbited track.

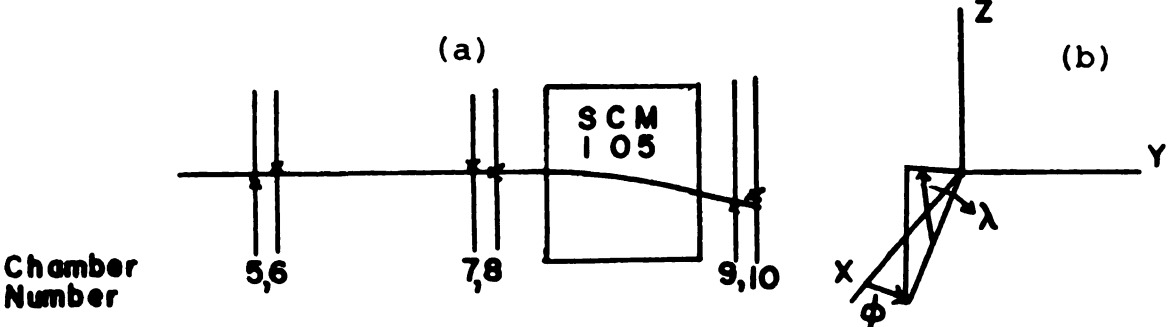


Figure B.1. Experimental apparatus after target (a) and coordinate system (b).

The track has three parameters, the curvature K $\equiv \frac{1}{P}$, λ and ϕ , shown in Figure B.lb. Denoting the deviations of the measured and orbited track by di, the fit procedure is to minimize $\chi^2 = \sum_{di}^2$ by varying the three tracks parameters K, λ and ϕ , denoted collectively as β . One gets

$$di = A_{i}^{(o)} + \sum \nabla \beta^{\lambda} \left(\frac{9\beta^{\lambda}}{9qi} \right)_{(o)}^{(o)}$$
 (B-1)

 $\left(\frac{\partial di}{\partial \beta_{\lambda}}\right)$ (0) will be denoted by Di_{λ}. The superscript (0) refers to the quantity evaluated using the intitial estimate for the three parameters $K^{(0)}$, $\lambda^{(0)}$, $\phi^{(0)} \equiv \beta_{\lambda}^{(0)}$ and $\Delta\beta_{\lambda} =$ β_{λ} - $\beta_{\lambda}^{\ (0)}$ is to be solved for as the correction term that will minimize χ^2 . One can expand χ^2 above using the Einstein summation notation.

Now set

$$\frac{\partial \beta^{A}}{\partial x_{5}} = 0 = 3 DiA Q_{A}^{A} + 3 DiA DiA QA$$
 (B-3)

Denote

$$y_{x} = 2D_{iy}d\hat{y}$$
 (B-4)

and

$$y_{\gamma} = 2D_{i\gamma}d_{\gamma}^{\circ}$$
 (B-4)
 $G_{\gamma\lambda} = 2D_{i\gamma}D_{i\lambda} \Delta \beta_{\lambda}$ (B-5)

We find

$$\nabla \dot{\beta}^{\lambda} = -\sum_{i}^{\lambda} G_{-i}^{\lambda \lambda} \dot{\lambda}^{\lambda} \qquad (B-e)$$

One recalls for this 3 x 3 case

$$\lambda = \begin{bmatrix} \sum_{i} q'_{i,0} \left(\frac{9qi}{9qi} \right)_{i,0} \\ \sum_{i} q'_{i,0} \left(\frac{9qi}{9qi} \right)_{i,0} \end{bmatrix}$$

$$\lambda = \begin{bmatrix} \sum_{i} q'_{i,0} \left(\frac{9qi}{9qi} \right)_{i,0} \\ \sum_{i} q'_{i,0} \left(\frac{9qi}{9qi} \right)_{i,0} \end{bmatrix}$$
(B-2)

The sum is over all chamber y and z spark position. Also one gets

$$G = \begin{bmatrix} \frac{3}{9} \frac{K}{4} \\ \frac{3}{9} \frac{K}{4} \end{bmatrix}_{(0)} \begin{pmatrix} \frac{3}{9} \frac{K}{4} \\ \frac{3}{9} \frac{K}{4} \end{pmatrix}_{(0)} \begin{pmatrix} \frac{3}{9} \frac{K}{4$$

APPENDIX C

TRANSFORMATION FROM M, t, $\theta_{\mathtt{Jac'}}$ $\phi_{\mathtt{TY}}$ TO $\overrightarrow{\mathtt{P}}$ AND $\overrightarrow{\pi}$

APPENDIX C

TRANSFORMATION FROM M, t, θ_{Jac} , ϕ_{TY} TO \overrightarrow{P} AND $\overrightarrow{\pi}$

One must work in the over-all center of mass in order to relate the neutron and outgoing $\Delta++$ to the initial beam and target protons. The scattering kinematics are outlined in Figure C.1.

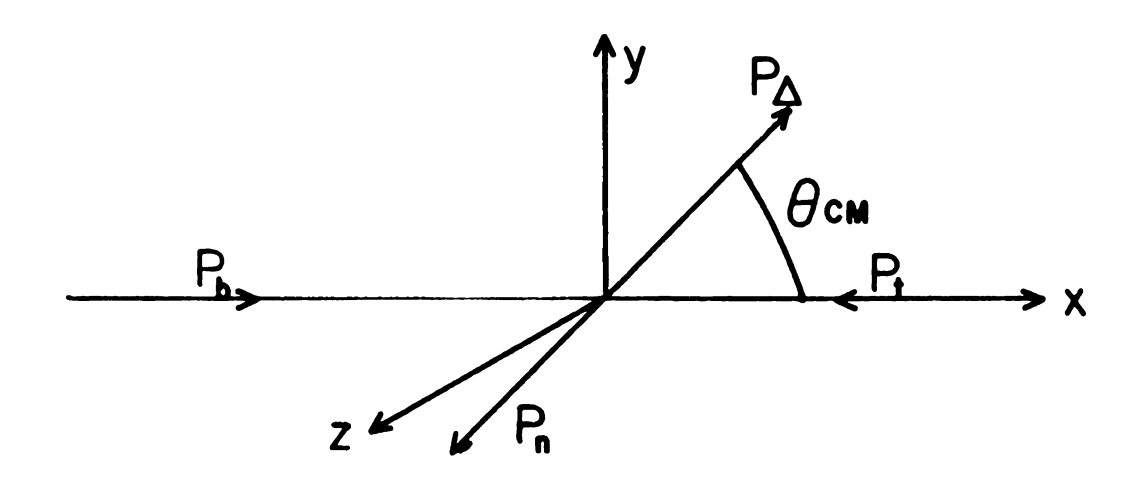


Figure C.1. The reaction PP+ Δ ++N in over-all center of mass.

The particle labels used above denote the 3-momentum of the particle. Two assumptions must be made in going from the four-variables M, t, $\theta_{\mbox{\scriptsize Jac}}$ and $\phi_{\mbox{\scriptsize TY}}$ to the six

variables \vec{P} and $\vec{\pi}$. These are a result of the symmetry of the problem and can be added without loss of generality. The first one is that the reaction has axial symmetry about the beam axis and so all scatterings can be assumed in the X-Y plane leaving $P_N^{\ Z} = P_\Delta^{\ Z} = 0$. This means in the lab one has $\vec{P}^Z = -\vec{\pi}^Z$. Also one can assume the beam is along the x axis.

One can write $\mathbf{M}_{p\pi^+}$ and t in terms of the variables defined in Figure C.1 as

$$M_{P\pi^+} = \sqrt{(P^{\mu} + \pi^{\mu})^2} \qquad (C-1)$$

and

$$t = (P_{h}^{M} - P_{h}^{M})^{2} = (P_{T}^{M} - P_{h}^{M})^{2} \qquad (c-2)$$

 P^{u} and π^{u} above are defined as $P^{u} = (E_{p}, i\vec{P})$ and $\pi^{u} = (E_{\pi}, i\vec{\pi})$. Also one has $P_{\Delta}^{u} = (E_{\Delta}, i\vec{P}_{\Delta})$ and $P_{b}^{u} = (E_{b}, i\vec{P}_{b})$ and similar definitions for P_{T}^{u} and P_{N}^{u} . One can expand t defined above to give

This expression can be solved to give the center of mass scattering angle in terms of \mathbf{M}_{Δ} and t

One can define

$$R(m_1, m_2, m) = \sqrt{[(m-m_1)^2 - m_2^2][(m+m_1)^2 - m_2^2]/2m} (c-5)$$

which can be used to get the beam momentum $|P_b|$ and the $\Delta++$ momentum $|P_\Delta|$ in the center of mass. If the total energy in the center of mass is \sqrt{s} , then

and

So far, the mass of the $\Delta++$ and the momentum transfer have served to determine the direction the resonance will travel away from the origin in the over-all center of mass. Now it is necessary to transform all center of mass vectors into the $\Delta++$ center of mass and make use of the decay angle information.

In the $\Delta + +$ center of mass, Figure C.2 shows the relevent decay quantities.

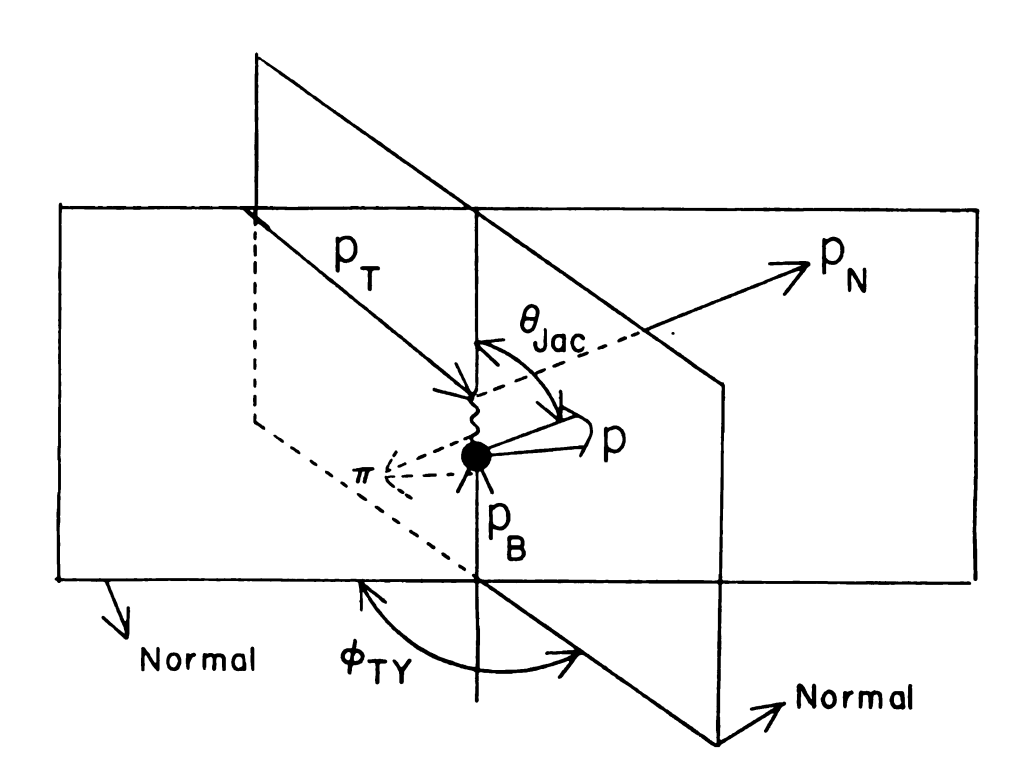


Figure C.2. $\theta_{\mbox{Jac}}$ and $\phi_{\mbox{TY}}$ defined in $\Delta +\!\!\!\!+$ center of mass.

One defines

$$\cos \phi_{Jac} = \frac{\vec{P}_B \cdot \vec{P}}{|\vec{P}_A||\vec{P}|} \qquad (C-8)$$

$$\cos \phi_{TY} = \frac{(\vec{P}_{x} \cdot \vec{P}_{N}) \cdot (\vec{P}_{R} \times \vec{P})}{|\vec{P}_{L} \times \vec{P}_{N}| |\vec{P}_{R} \times \vec{P}|} \qquad (c-9)$$

$$sin \phi_{TY} = \frac{\vec{P}_B \times (\vec{P}_T \times \vec{P}_N) \cdot (\vec{P}_B \times \vec{P})}{|\vec{P}_B \times (\vec{P}_T \times \vec{P}_N)||\vec{P}_B \times \vec{P}|} \quad (C-10)$$

First one can make use of the Jackson angle. One can find the component of the decay proton parallel to the beam as shown in Figure C.3, given by

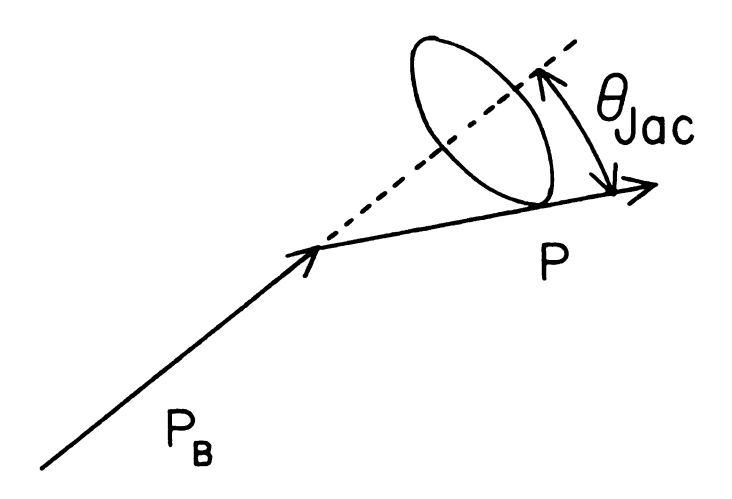


Figure C.3. Beam and decay proton in $\Delta++$ center of mass.

R is the momentum of the proton and pion in $\Delta ++$ decay center of mass given by

$$R = R (M_{P}, M_{\pi}, M_{P_{\pi}^{+}})$$
 (c-12)

and \bar{N}_B is the unit vector given by $\bar{N}_B = \bar{P}_B/|\bar{P}_B|$ evaluated in the $\Delta++$ center of mass.

The components of proton momentum perpendicular to the beam involves the Treiman-Yang angle.

Figure C.4 shows Figure C.2 from above and illustrates the angle between the planes.

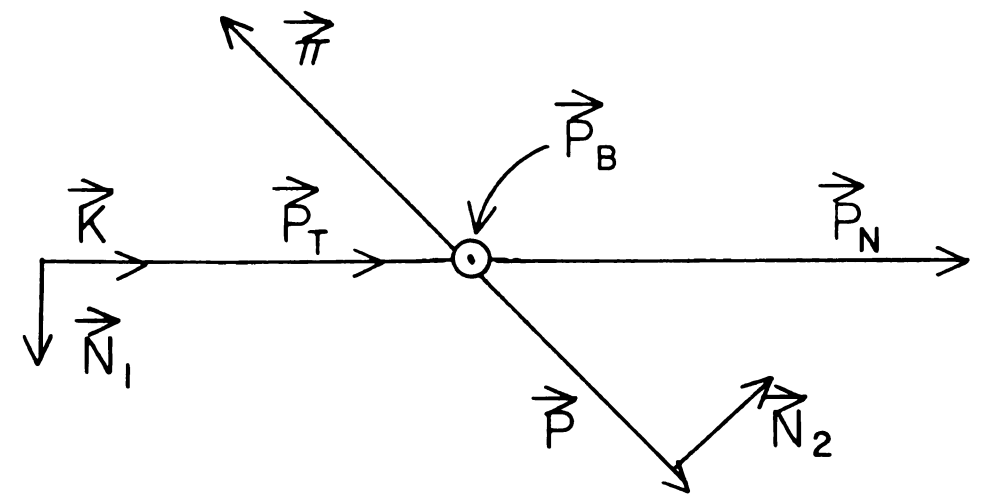


Figure C.4. Projected view of planes described in Figure C.2.

The vectors shown above are defined in terms of known vectors as below:

$$\vec{N} = \frac{\vec{P}_T \times \vec{P}_N}{|\vec{P}_T \times \vec{P}_N|}$$
 (c-13)

$$\overrightarrow{K} = \overrightarrow{N}_B \times \overrightarrow{N}_i \qquad (c-14)$$

$$\vec{N}_B = \frac{\vec{P}_B}{|\vec{P}_B|} \qquad (c-15)$$

$$\vec{N}_2 = \frac{\vec{P}_B \times \vec{P}}{|\vec{P}_B \times \vec{P}|}$$
 (c-16)

By definition, the Treiman-Yang angle is the angle between the two planes and is given in terms of the newly defined vectors as

$$\cos\phi_{TY} = \vec{N}_1 \cdot \vec{N}_2 \qquad (c-17)$$

$$Sin \phi_{TY} = \vec{K} \cdot \vec{N}_2 \qquad (c-18)$$

The vectors \vec{K} and \vec{N}_1 form a perpendicular system and one can find the perpendicular component of the decay proton from Figure C.5,

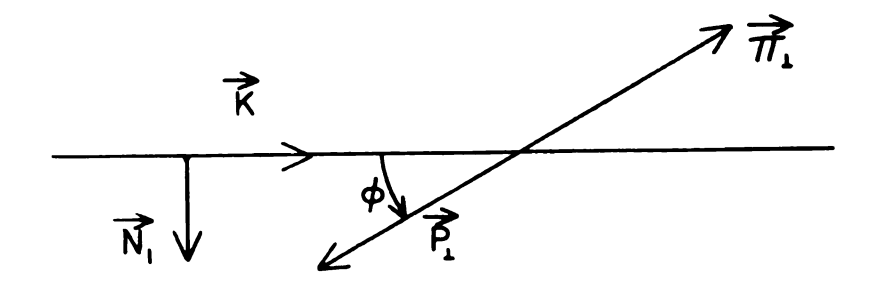


Figure C.5. Momentum of $\Delta++$ decay products perpendicular to beam proton in $\Delta++$ center of mass.

where

$$\vec{P}_{\perp} = R(\vec{N}_{1}, \sin \phi_{TY} - \vec{K}\cos \phi_{TY}) \qquad (C-19)$$

$$\vec{P} = \vec{P}_{1} + \vec{P}_{11} =$$

and so $P = P_1 + P_2$

.

$$\overrightarrow{\pi} = -\overrightarrow{P} \qquad (c-21)$$

Both the π^μ and P^μ four vectors can be transformed into the lab to give the desired decay vectors.

APPENDIX D

 $\boldsymbol{\theta}_{\texttt{Jac}}$ AND $\boldsymbol{\varphi}_{\texttt{TY}}$ BIASES

APPENDIX D

$\theta_{\mbox{\scriptsize Jac}} \ \mbox{\scriptsize AND} \ \ \phi_{\mbox{\scriptsize TY}} \ \mbox{\scriptsize BIASES}$

A typical event, as viewed in the $\Delta + +$ center of mass, is shown below. The beam is along the x axis in the lab.

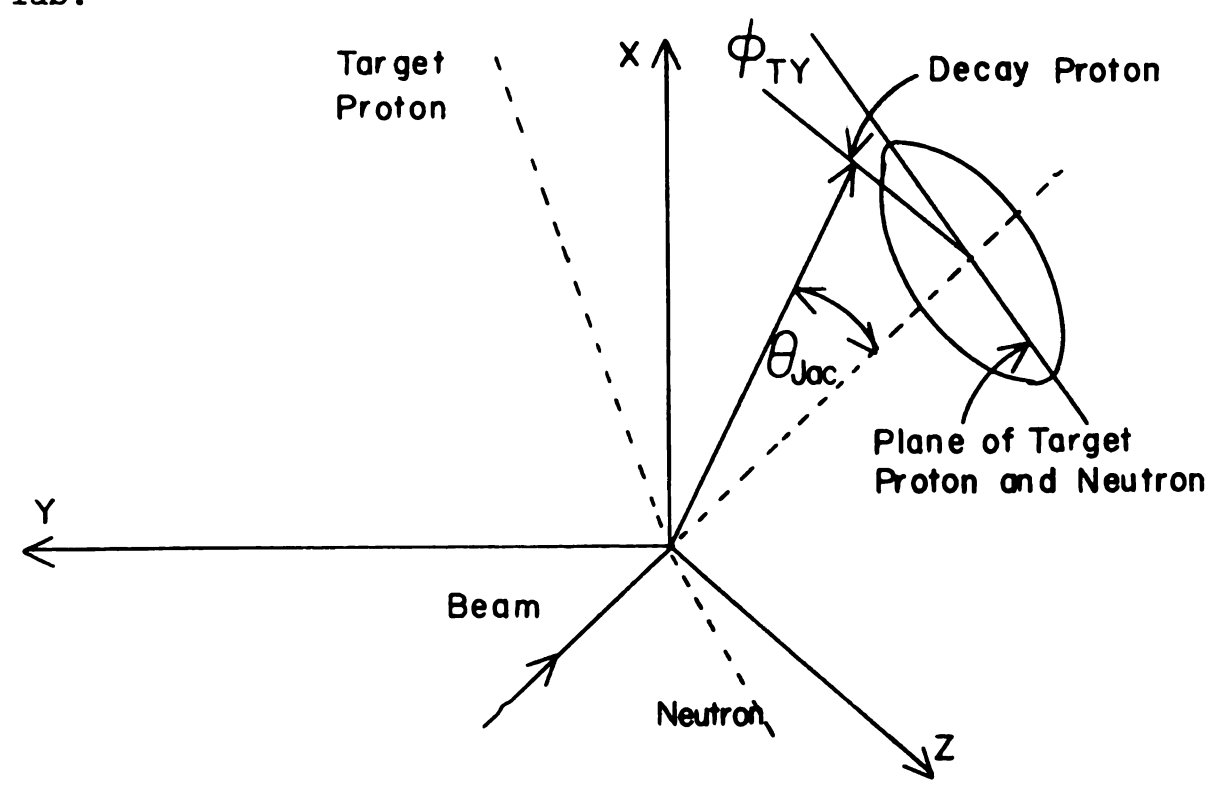


Figure D.1. PP+PN π + event in P- π + center of mass.

For simplification, one can consider the beam direction as forward in the spectrometer, and the neutron to be at a large angle or backwards in the lab. is the track which is most sensitive to acceptance and has in most cases the widest angle and is the slowest. acceptance will be high if the pion is forward and fast, and low if the pion is wide angled or slow. The forward speed of the pion is smallest if the decay proton is in line with the target proton. In order to get the decay proton to the lab, one just does a Lorentz boost in the direction opposite the target proton. By lining the decay proton up in the $\Delta++$ cm, one gets a fast proton in the lab. This gives a slow wide angle pion. From this one can see that if there are certain decay angles which have zero acceptance, this effect will be larger for a high mass $\Delta ++$ than one of low mass. Typically in the $\Delta++$ center of mass, the proton and pion come off back to back with a momentum of 200 Mev/c. At higher momentum, a backwards pion in the Δ ++ cm would correspond to a slower or wider angle pion in the lab.

In the $\Delta++$ center of mass, the beam proton, which defines the zero for $\theta_{\rm Jac}$, and the target proton, which defines the way back to the lab, are in general not in opposite directions. As momentum transfer increases, so does this off-set angle. If the Jackson angle happens to equal this off-set angle, the target and decay protons can still be anti-parallel and a minimum acceptance will occur.

This line-up will be precise only if the Treiman-Yang angle is zero, as will be discussed later. For t close to zero, where this beam proton and target proton are almost opposite in the $\Delta++$ cm, then $\theta_{\rm Jac}$ equal zero is the situation which makes the pion slowest. Also, for $\theta_{\rm Jac}$ close to zero, a 360° rotation for $\phi_{\rm TY}$ does little to disrupt the alignment because it is just making a tight small circle about the target proton. Monte Carlo studies show there is a zero acceptance at $\theta_{\rm Jac}=0$ for all $\phi_{\rm TY}$.

As t increases, and the angle between the target proton and the beam proton becomes less anti-parallel, it becomes necessary for the Jackson angle to become larger in order that the pion comes off directly backwards in the laboratory. This backwards pion condition requires a coincidence between the planes of the target proton and the neutron. This is the place where $\phi_{TY} = 0$. Monte Carlo studies reveal that as one goes to high momentum transfer, the Jackson angle where the acceptance is zero increases slowly, and the zero acceptance occurs only if $\phi_{TY} = 0$.

APPENDIX E

MONTE CARLO EVENT GENERATION

APPENDIX E

MONTE CARLO EVENT GENERATION

An event of the type PP+P π +N can be completely specified by four quantities. The most useful for this study are the mass of P π +, momentum transfer squared from the target proton to the neutron, and the outgoing scatter angles of decay for the P or π + in the P π + center of mass, $\theta_{\rm Jackson}$ and $\phi_{\rm Treiman-Yang}$. The bubble chamber data was used to generate these distributions because it is thought to have no strong biases. In fact, the bubble chamber data agrees within statistics with the present experimental data once a Δ ++ cut is made.

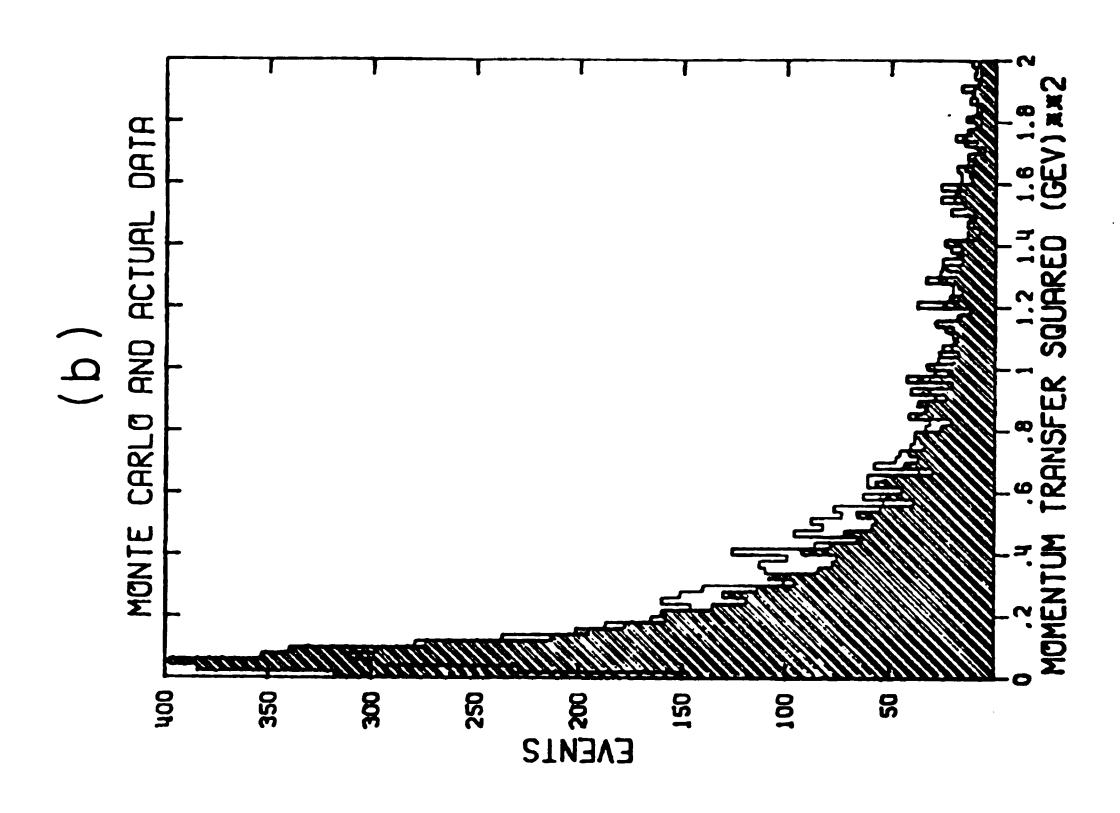
The bubble chamber mass distribution is scaled down from the 6.6 Gev/c beam momentum kinematic boundary to the 6.0 Gev/c boundary. The bubble chamber mass, t, $\theta_{\rm Jac}$ and $\phi_{\rm TY}$ distributions are converted into event generation probabilities by an integral transform.

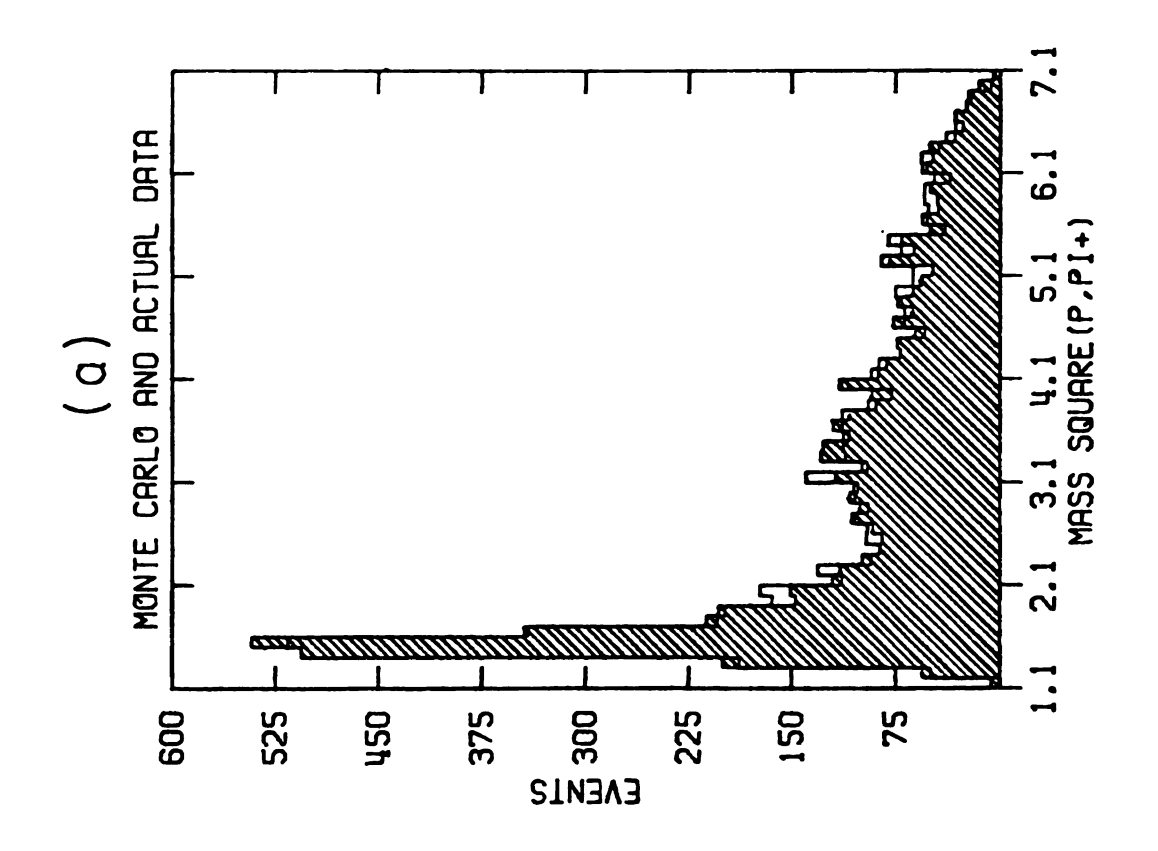
If F(x) is any of the above distributions defined between X_L and X_U , events can be generated in accordance with this distribution by first generating a number W such

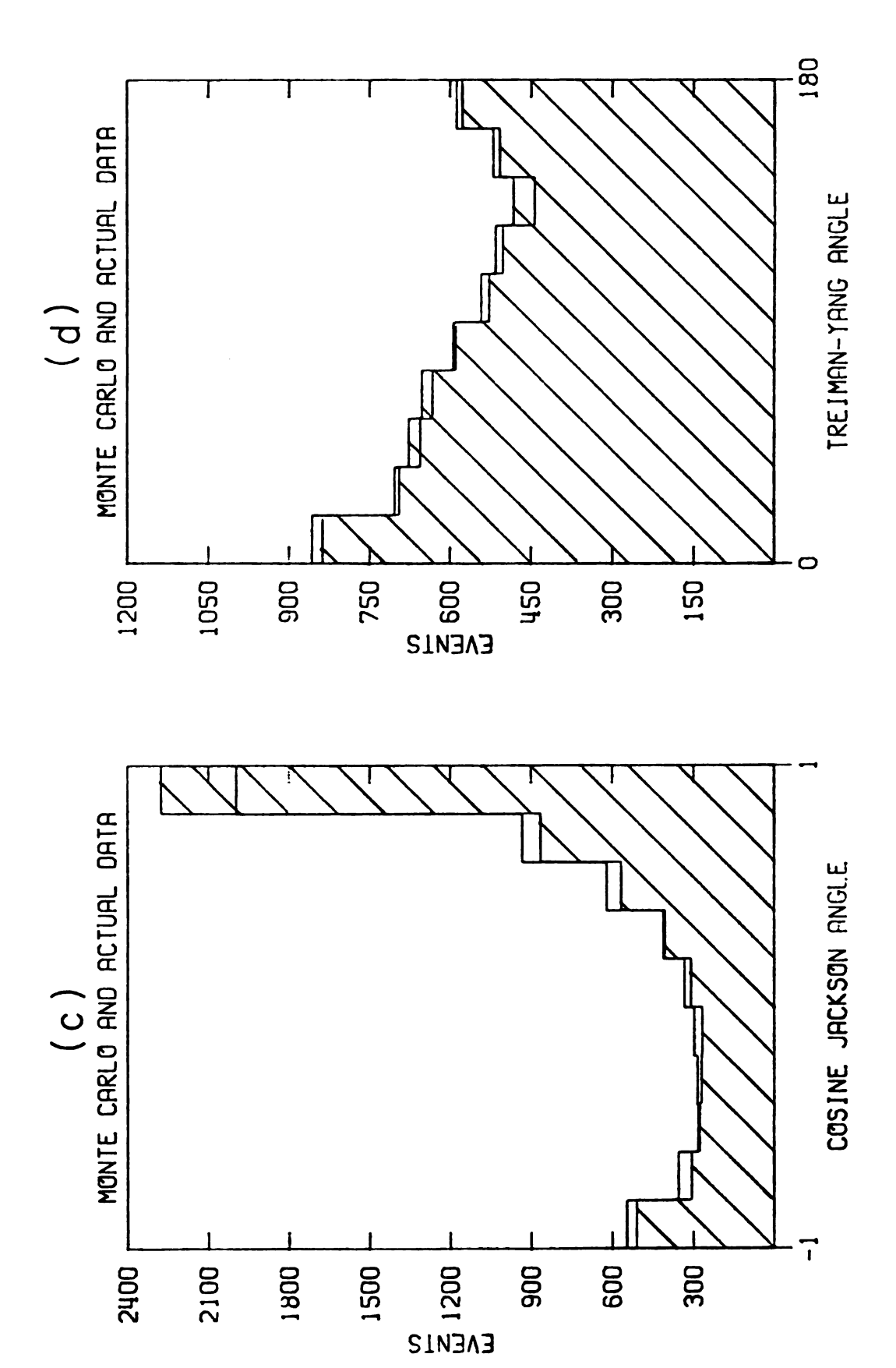
that W is a random number between 0 and $\int_{0}^{x} F(x) dx$. Then one must generate an event of value x where x is the solution to $W(X) = \int_{0}^{x} F(x) dx$.

These events can be transformed first to the overall center of mass where the neutron and $(P-\pi+)$ vectors are found using $M(P\pi+)$ and t, then in the $(P-\pi+)$ center of mass where the pion and the proton vectors are found from M(P π +), $\theta_{\rm Jac}$ and $\phi_{\rm TY}$. It is known that only (P- π +) combinations associated with the beam projectile will trigger the apparatus so only beam vertex $P=\pi+$ events are produced. Appendix C gives the details of the above transformation. Once the four vectors for the event are back in the laboratory, the two outgoing tracks are rotated randomly about the beam axis in order to resupply the event with a symmetric degree of freedom not obtainable from the basic four variables which describe the event. Figure E.la-d shows the initial bubble chamber distribution shaded, and final distributions derived from the Monte Carlo event generation described above unshaded.

Original bubble chamber events (shaded) and Monte Carlo distributions which are the result of generation program (unshaded). Figure E.l.a-d.







APPENDIX F

RESONANCE MASS AND WIDTH CORRECTIONS DUE

TO EXPERIMENTAL ERRORS

APPENDIX F

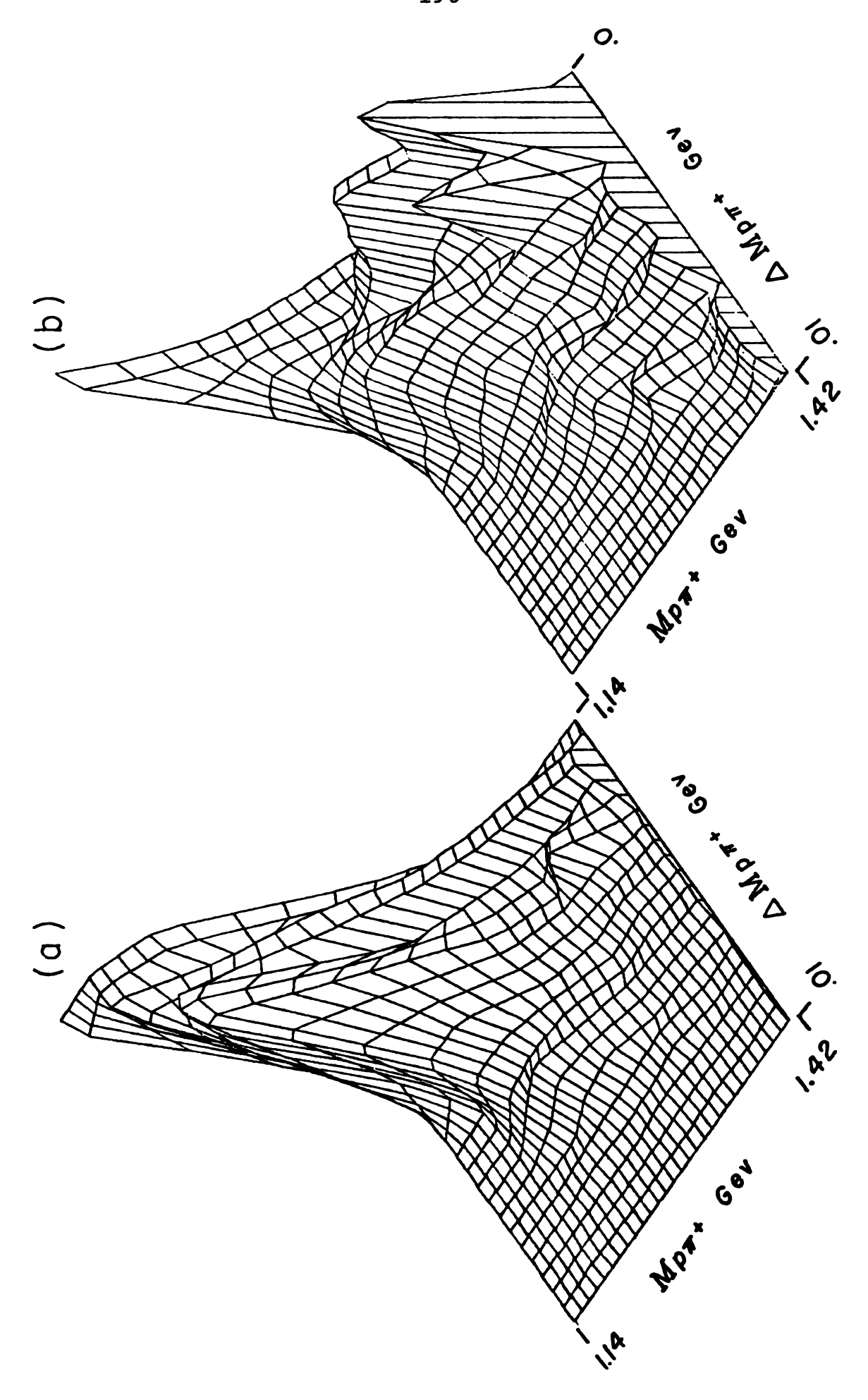
RESONANCE MASS AND WIDTH CORRECTIONS DUE TO EXPERIMENTAL ERRORS

Figure F.la-b shows the invariant mass and the calculated error in this quantity. Figure F.l-b has the probability of finding the error E at mass M normalized so that the area under the probability surface at fixed M is constant.

In order to see the effects of the error on a given mass distribution, one must first select the mass, then look up the probability for a given error P(E,M) from the mass-error distribution. One gets the new mass distribution by a Gaussian smear of width E at the fixed M of probability P(E,M). This can be expressed as

$$\sigma(M') = \sum_{E} P(E, M) \exp \left[-\left(\frac{M'-M}{E}\right)^{2}\right] \quad (F-1)$$

subject to the restriction that $\int dM'\sigma(M') = 1$. The actual error at the resonance peak of 1.230 GeV is 5 MeV. The error at the half maximum points are 3 MeV at M = 1.176 GeV



and 6 Mev at M = 1.298 Gev resulting in a width error of 8 Mev. This is summarized in Table F.1. The column marked data gets its peak and width directly from the data, and not from the Breit-Wigner fit to the data. The fit does not have precisely the right shape.

Table F.1. Peak and Width of $M(P,\pi+)$ With Resolution Errors.

	Data	Breit Wigner Fit
Peak (Mev)	1226. <u>+</u> 5.	1226. <u>+</u> 5.
Width (Mev)	122. <u>+</u> 8.	133. <u>+</u> 8.

The average error increases from 1 to 6 Mev between the masses of 1.14 to 1.26 Gev. Above 1.26 Gev the error is approximately constant at 6 Mev.

In order to study the effect of the experimental errors on the mass distribution, the events are smeared and fit by a Breit-Wigner curve. The Breit-Wigner form used is given by

$$\sigma(M) = \frac{\Gamma}{(M^2 - M_0^2)^2 + \Gamma/4} \text{ where } \Gamma = \frac{M_0 V (QR)^3}{[1 + (QR)^2]}. \quad (F-2)$$

M is the mass of the P- π + system and Q is the proton momentum in the P- π + center of mass. R is the Δ ++ radius and M and γ are varied in the fit. The fit parameters are summarized in Table F.2.

Table F.2.--Breit-Wigner Fits to Unsmeared and Smeared Data.

Fit Type M		24	Γ _(M₀)		Peak(Gev) Exp Fit		(Gev)	x ² /Point
Fit Type	(Gev) (Gev	(Gev)	(Gev ²)	Ехр	Fit	Exp	Fit	
Unsmeared	1.246	.753	.179	1.226	1.226	.122	.133	2.
Smeared	1.247	.766	.182	1.227	1.226	.130	.135	1.5

As expected the peak is insensitive to the error but the width is directly related to the errors. Table F.3 gives the corrected mass parameters after the effects of experimental error have been removed. The row marked fitted used smeared and unsmeared fitted parameters to predict the correct mass parameters, while the row marked experimental uses parameters obtained from the actual mass distributions.

Table F.3.--Parameter for Predicted Fitted and Experimental Mass and Distribution.

	M _O (Gev)	γ (Gev)	FWHM (Gev)	Peak (Gev)
Fitted	1.245	.740	.131	1.225
Experimental	1.224	.700	.126	1.226

APPENDIX G

SPARK CHAMBER EFFICIENCY

APPENDIX G

SPARK CHAMBER EFFICIENCY

The spark chamber efficiency calculation will be given in detail only for the magnet section chambers. The rest are calculated similarly. Denote by α_N where N is 5-8 the probability that chamber N misses 1 track and B the probability of missing both tracks. Let $E_N = \alpha_N + B_N$ be the probability that chamber N does not see either track. The probability that the Nth chamber sees both tracks is $1-E_N$ and the probability for a perfect event in the magnet section, abbreviated by P_{4-4} , is then

$$P_{4-4} = \frac{8}{11}(1-E_i)$$
 (G-1)

and is symbolized by . The probability of firing 4 chambers on one side and 3 on the other is symbolized by

and is denoted by P_{3-4} and is given by

$$P_{3-4} = \sum_{i=5}^{8} \alpha_i \prod_{j=5}^{8} (1-E_j).$$
 (G-2)

The probability P_{33} for both tracks to misfire in one chamber is

$$P_{3-3}$$
 (same chamber) = $\sum_{i=5}^{8} B_i \prod_{j=5}^{8} (1-E_i) (G-3)$

and the combined probability for $P_{4-3}^{+P}_{3-3}$ where the P_{3-3} case has one chamber miss for both tracks is

$$P_{y-3} + P_{3-3}$$
 (same chamber) = $\sum_{i=5}^{8} E_i \pi_{i+i}$ (G-4)

since $E_i = \alpha_i + B_i$. Another type of 3-3 event can occur when different chambers miss a track as shown below.

The entire term can be expressed as

$$P_{3-3}(\text{different chambers}) = \sqrt{2} \sum_{i=5}^{7} \alpha_i \sum_{j=i+1}^{8} \alpha_j \prod_{\substack{k=5\\k\neq i\\k\neq j}}^{8} (1-\epsilon_k) (6-5)$$

The factor of 1/2 is necessary because the expression above includes events where one track fires 4 chambers and the other fires only 2 chambers, symbolized by

These types of events will not pass the filter program. The total probability of getting an event is $P_{4-4} + P_{4-3} + P_{3-3}$ (same chamber) + P_{3-3} (different chambers) =

$$\begin{array}{lll}
8 \\
\pi (1-E_i) + \sum_{i=5}^{8} E_i \pi (1-E_j) + \frac{7}{2} \sum_{i=5}^{8} \alpha_i \sum_{j=i+1}^{8} \alpha_j \pi (1-E_k) \\
i=5 & i=5 & i=5 & i=5 \\
i=6 & i=5 & i=6
\end{array}$$

As one can see from the magnet chamber event probability calculation, care must be taken to be sure certain event classes are not counted twice. With this observation made and the notation established, the results for the other sections will be summarized in Tables G.1 and G.2.

Table G.1.--Beam Chambers.

Condition	Abbreviation	Symbol	Probability
All 4 hit	P 4	++++	サ
l miss	P ₃		Σ E; π(1-Ej) 1 = 1 + 1

Table G.2. -- Hodoscope Chambers.

Condition	Abbreviation	Symbol Probability
All fire	P ₂₂	TT (1-E;)
One miss One side	P ₂₁	$\frac{1}{1+1+\cdots} + \cdots = \sum_{i=0}^{10} \alpha_i \prod_{j=0}^{10} (1-\epsilon_j)$
Two miss Same chamber	P ₁₁	

Iteration

If one knew α_i and B_i for the chambers, one could put them into the formulas above and get an efficiency. The individual chamber efficiencies are coupled to the over all efficiency and the solutions must be obtained simultaneously.

In the magnet section, the first approximation to α_i and B_i is just $N_i(1)/N$ and $N_i(2)/N$ respectively, where N_i is the total number of firings for the chambers and $N_i(1)$ and $N_i(2)$ are the single and double misfires respectively in chamber i. However, B_i estimated this way would be too low because of the constraint that at least three firings must occur per track in the magnet chamber region. In reality, B_i estimated as above is the probability that one chamber does not fire and all three others do fire. An exact expression for B_i is the sum of the probability that

chamber i miss two tracks and is seen plus the probability that chamber i miss two tracks and is not seen. Similar statements can be said for α_i and E_i to give

$$E_i = N_i^{(0)}/N_T + P_i^{(0)} N.s.$$
 (G-7)

$$\alpha_i = N_i^{(1)}/N_T + P_{i N.s.}^1$$
 (G-8)

$$B_i = N_i^{(2)}/N_T + P_{i \text{ N.s.}}^2$$
 (G-9)

where P_i^N N.S. is the probability for N sparks in chamber i to be missing and the event not to be seen. Table G.3 will summarize the probability of the ith magnet chamber missing two track and the event not be seen. The notation $\sum_{i=j}^{4} (1-E_k)$ will be used to mean $\sum_{k=1}^{4} (1-E_k)$. k=1 $k\neq i$ $k\neq j$

Table G.3.--Probability for ith Magnet Chamber to Miss Two Tracks of a Missing Event.

$ \begin{array}{cccccccccccccccccccccccccccccccccccc$	Symbol	Term
	# + · · + # + · · · + # + · · · + # # + · · · + # # # + · · · + # # # #	Bi Fijan (I-E) Bi Fijan (I-E)

The sum of the above terms is P_i^2 N.S. which can be written as $B_iF(\alpha_j,B_j)$ $j\neq i$. Similarly one could write out terms for P_i^1 and P_i^0 N.S. and obtain the efficiency by solving the four simultaneous equations below.

In practice it is possible to iterate the equations which rapidly converge to give an efficiency. Similar equations can be written down for the beam and hodoscope chambers and the final apparatus efficiency is taken as the product

 $E_{App} = E_{B}E_{Mag} E_{Hod}$

The data N_0 , $N_i^{(0)}$, $N_i^{(1)}$ and $N_i^{(2)}$ are obtained for the most of the input data which makes Teuta fit confidence levels greater than .03 and is present in the final summary tape. The results of the counting of total firings, one firing and no firings are listed for 42427 Teuta fit events in Table G.4a-c respectively.

Table G.4a.--Beam Chambers.

Chambers	Sparks	Misses	α
1	41273	1154	.027
2	40787	1640	.039
3	42016	411	.0096
4	40859	1568	.037

Table G.4b.--Magnet Chambers.

Chamber	2 Sparks	l Spark	No Spark	α	В
5	32531	9322	574	.219	.014
6	36620	5682	125	.136	.0030
7	34027	8284	116	.195	.0027
8	40912	1504	11	.035	.00025

Table G.4c.--Hodoscope Chambers.

Chamber	2 Sparks	l Spark	No Spark	α	В
9 10	37271 37021	5060 5388	96 18	.119	.002

The total efficiency is then the product of the three subefficiencies. APPENDIX H

ERROR CALCULATION

APPENDIX H

ERROR CALCULATION

Missing mass

We can calculate the error in the missing mass for the reaction PP+P π +N or PP π ° as below. A diagram and a coordinate system for the reaction is given in Figure H.l.

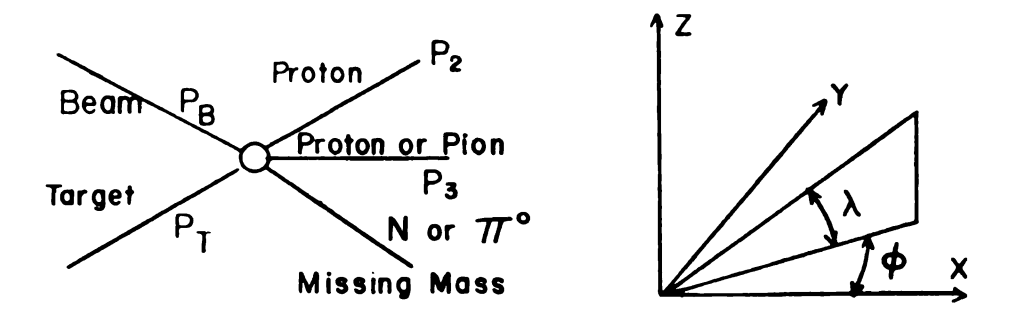


Figure H.1.--Notation and coordinate system used in this appendix.

We can write

$$(M M)^{2} = (P_{8} + P_{7} - P_{2} - P_{3})^{2} = (E_{8} + E_{7} - E_{2} - E_{3})^{2} - \sum_{i=1}^{3} (P_{8}^{i} + P_{7}^{i} - P_{2}^{i} - P_{3}^{i})^{2} (H-I)$$

Substitute

$$P^{x} = P \cos \lambda \cos \phi$$

$$P^{y} = P \cos \lambda \sin \phi \qquad (H-2)$$

$$P^{z} = P \sin \lambda$$

gives

$$(MM)^{2} = 3M_{2}^{2} + M_{3}^{2} + 2E_{B}E_{4} - 2E_{B}E_{2} - 2E_{B}E_{3} - 2E_{4}E_{2} - E_{4}E_{3} + E_{2}E_{5}$$

$$+ 2P_{B}P_{2} \left[\cos \lambda_{B} \cos \lambda_{2} \cos (\varphi_{B} - \varphi_{2}) + \sin \lambda_{B} \sin \lambda_{2} \right]$$

$$- 2P_{2}P_{3} \left[\cos \lambda_{2} \cos \lambda_{3} \cos (\varphi_{2} - \varphi_{3}) + \sin \lambda_{2} \sin \lambda_{3} \right]$$

$$+ 2P_{3}P_{B} \left[\cos \lambda_{3} \cos \lambda_{B} \cos (\varphi_{3} - \varphi_{B}) + \sin \lambda_{3} \sin \lambda_{B} \right] (H-3)$$

If one defines Z(i) = (-1,1,1) and considers the beam as track 1, one can write

$$\Theta_{i,j} = \cos \lambda_i \cos \lambda_j \cos (\phi_i - \phi_j) + \sin \lambda_i \sin \lambda_j$$
 (H-6)

where i, j and k are defined cyclicly as 1, 2, 3; 2, 3, 1; or 3, 1 and 2. Using equation H-6 one can write

$$\frac{\partial P_{1}}{\partial P_{1}} = \frac{2P_{1}}{E_{b}} (E_{T} - E_{2} - E_{3}) + 2P_{2}\Theta_{12} + 2P_{3}\Theta_{13} (H - 7)$$

$$\frac{\partial MM^{2}}{\partial P_{2}} = \frac{2P_{2}}{E_{2}} \left(-E_{1} - M_{p} + E_{3}\right) + 2P_{1} \oplus_{12} - 2P_{3} \oplus_{23} \quad (H-8)$$

$$\frac{\partial MM^2}{\partial P_3} = \frac{2P_3}{E_3} \left(-E_1 - M_p + E_2\right) - 2P_2\Theta_{23} + 2P_1\Theta_{13} \quad (H-9)$$

The error in missing mass squared can be written as

$$(E_{rror})^2 = \sum_{i,j} \mathcal{E}_{i,j} \vee_i \vee_j \qquad (H-10)$$

where ϵ_{ij} is the symmetrized error matrix of Circe and

$$\Lambda = \left[\frac{9b'}{9Mu_s}, \frac{9y'}{9Mu_s}, \frac{9\phi'}{9Mu_s}, \frac{9b^2}{9Mu_s}, \frac{9y'}{9Mu_s}, \frac{9\phi'}{9Mu_s}, \frac{9\phi'}{9Mu_s}, \frac{9\phi'}{9Mu_s}, \frac{9\phi'}{9Mu_s} \right] (H-II)$$

Invariant Mass

This error involves just two tracks. The notation is shown in Figure H.2.

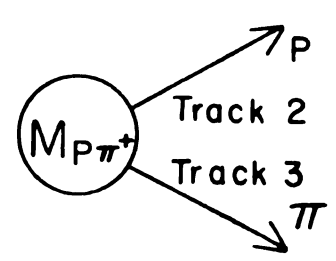


Figure H.2. Notation used in calculating invariant mass error.

Using the decay and coordinate system as shown above we get

$$M_{P\pi}^{2} + = (E_{2} + E_{3})^{2} - (P_{2}^{x} + P_{3}^{x})^{2} - (P_{2}^{y} + P_{3}^{y})^{2} - (P_{2}^{z} + P_{3}^{z})^{2} - (P_{2}^{z} + P_{3}^{z})^{2} + (P_{2}^{z} + P_{3}^{z})^{2}$$

gives

$$M_{P\pi}^{2} + M_{P}^{2} + M_{\pi}^{2} + 2E_{2}E_{3} - 2P_{2}P_{3}\left[\cos{\lambda_{2}}\cos{\lambda_{3}}\cos(\phi_{2} - \phi_{3}) + \sin{\lambda_{2}}\right]$$
(H-14)

One can calculate the vector

$$V = \left[\frac{9 \, h^2}{9 \, h^2}, \frac{9 \, y^2}{9 \, h^3}, \frac{9 \, h^2}{9 \, h^3}, \frac{9 \, h^3}{9 \, h^3}, \frac{9 \, h^3}{9 \, h^3}, \frac{9 \, h^3}{9 \, h^3}\right] (H-I2)$$

and get

$$(Error)^2 = \sum_{i,j} \xi_{i,j} \forall_i \forall_j$$
 (H-16)

where ϵ_{ij} is the 6 x 6 error matrix for the 6 quantities involved.

Momentum Transfer Squared

The errors in this are calculated similar to the missing mass errors. The notation is defined in Figure H.3.

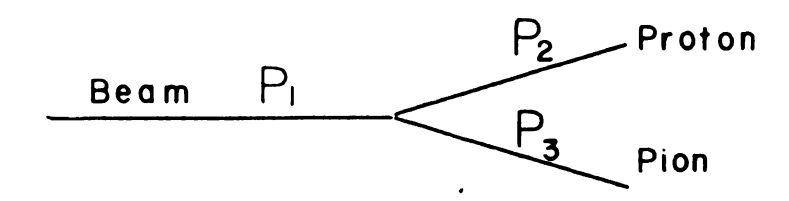


Figure H.3. Notation used in calculating momentum transfer squared error.

All the results from the missing mass calculations apply except for the following:

$$t = (MM)^2 - M_P^2 - 2M_P(E_1 - E_2 - E_3)$$
 (H-17)

$$\frac{96}{97} = \frac{96}{900} - Mb_{\frac{1}{3}}$$
 (H-18)

$$\frac{\partial t}{\partial P_2} = \frac{\partial MM^2}{\partial P_2} + M_P \frac{ZP_2}{ZP_2}$$
 (H-19)

$$\frac{\partial t}{\partial P_2} = \frac{\partial MM^2}{\partial P_3} + \frac{MP}{E_2} = \frac{2P_2}{E_3} + \frac{E_2}{E_3} \qquad (H-19)$$

